FACULDADE DE ENGENHARIA DA UNIVERSIDADE DO PORTO

Machinability studies of additively manufactured 18Ni300 maraging steel

Marcelo Rodrigo Magalhães Ramalho Mendes Lainho

Master's dissertation in Mechanical Engineering

Supervisor: Prof. Dr. Abílio Manuel Pinho de Jesus

Co-supervisor: Eng. Tiago Emanuel Fraga da Silva

February 17th, 2020

Machinability studies of additively manufactured 18Ni300 maraging steel

Marcelo Rodrigo Magalhães Ramalho Mendes Lainho

Master's dissertation in Mechanical Engineering

February 17th, 2020

Resumo

Apesar do aumento significativo, na indústria das tecnologias de Fabrico Aditivo (FA) devido à melhoria das propriedades mecânicas e integridade estrutural dos componentes produzidos, operações de pós-processamento através de processos subtrativos ainda são correntemente utilizadas de modo a alcançar as tolerâncias geométricas e acabamentos superficiais requeridos. O âmbito desta dissertação é a avaliação da maquinabilidade do aço maraging 18Ni300 produzido por fabrico aditivo e estabelecer uma comparação com o material convencional.

Amostras produzidas por um processo de *Laser Powder Bed Fusion* (LPBF) foram sujeitas a uma caraterização de material, onde características como a composição química, a microestrutura, dureza, rugosidades e defeitos de produção foram analisados. O comportamento mecânico do material foi também avaliado e comparado com o material convencional, através de ensaios de compressão.

Testes de corte experimentais (ensaios de torneamento e fresagem) para ambas as amostras (FA e convencional) foram executados e a influência dos diferentes parâmetros de corte foi avaliada através de análise das forças de corte, potência consumida, pressão específica de corte, qualidade superficial e morfologia das aparas. A influência da geometria das ferramentas de corte foi também avaliada para uma vasta variedade de parâmetros.

O estudo mostrou que apesar de algumas diferenças entre o material de FA e convencional em termos de resistência à compressão, em termos de maquinabilidade os materiais apresentaram comportamentos muito semelhantes. De um modo geral foram produzidas aparas largas nas operações de torneamento, mesmo com recurso a ferramentas com quebra-aparas. Aparas serrilhadas são características de ligas com elevado teor de Ni. O uso de ferramentas com quebra-aparas apesar de não existirem diferenças no tipo de aparas produzidas, levam a uma redução acentuada em termos de forças de corte, melhorando as operações de corte.

Os resultados dos ensaios de fresagem foram tratados com um modelo analítico de corte que permitiu gerar pressões específicas de corte consistentes com os valores obtidos em torneamento.

Abstract

Despite the significant industrial increase of Additive Manufacturing (AM) technologies, due to recent improvement in mechanical properties and structural integrity of the produced components, post-processing operations based on subtractive processes are still often employed in order to achieve the required geometrical tolerances and surface quality. The scope of this dissertation is the machinability evaluation of the 18Ni300 maraging steel produced by AM as well as its comparison with the conventionally fabricated steel.

Laser Powder Bed Fusion (LPBF) specimens were submitted to a material characterization stage, where aspects such as chemical composition, microstructure, hardness measurements, surface roughness and production defects were analyzed. The mechanical behaviour of the material was also assessed and compared to the conventional steel through quasi-static compression tests.

Experimental cutting test (turning and milling operations) for both AM and conventionally manufactured samples were carried out and the influence of the different cutting parameters was evaluated by analyzing cutting forces, power consumption, specific cutting pressure, surface quality and chip morphology. Cutting tool geometry influence was also conducted for a wide range of cutting parameters.

The experimental study showed that in spite of the differences between AM and conventional material regarding compression resistance, in terms of machinability, both materials presented very similar behaviour. For most tests, long continuous chips were obtained in the turning operations, even with the use of a chip-breaker tool. Serrated chips were also obtained, and are a typical characteristic of the Ni-based alloys. The use of a chip-breaker tool, did not prove to be influential regarding chip geometry. However, this type of tool, when compared to a flat rake face insert improve the cutting loads during the turning operations.

The results from the milling tests were analysed using an analytical cutting model that allowed to generate specific cutting pressures comparable with the ones obtained in the turning operations.

Acknowledgements

First of all I would like to thank my Supervisor, Professor Abílio de Jesus for the opportunity to be a part of this project and for allowing me to improve my knowledge in the different subjects addressed in this dissertation, for all his knowledgeable inputs and help with my struggles, and comprehensibility he had for letting me dedicate some time to the last course unit allowing me to finish my master's degree.

A special thanks to Eng. Tiago Silva for all the help provided along these last few months, his constant willingness to aid me in my hardships and his permanent availability and patience throughout the semester helping me to achieve the desired goals. This thesis wouldn't be possible without his advice and guidance.

I also express my gratitude to INEGI for the opportunity to be a part of an important innovation project and for the technical support provided, expressing my deepest gratitude to Armanda Marques, responsible for the metallurgical laboratory for her availability, positive attitude and encouragement even when my motivation wasn't the best.

I would also like to acknowledge Domingos Carvalho for his assistance and availability for the several DEMEC workshop activities that were carried out.

In addition, I would like to thank the CETRIB laboratory, in particular Professor Carlos Fernandes for his availability in performing the surface quality measurements of the samples.

Also, I express my gratitute do the LET facilities of the department of mechanical engineering of FEUP for the quasi-static compression tests performed there.

Furthermore, I also express my gratefulness to Palbit S.A. for the technical support and the availability to help throughout this project and also for providing their facilities for the experimental tests campaign to be carried out.

Special thanks to EROFIO for providing the AM samples used in this investigation work.

Additionally, I express my deepest thankfulness for all the friends and colleagues I've made throughout my academical path, particularly to the friends who, throughout this semester were also doing their dissertation and provided me with the company, friendship and most of all the motivation in the hardest moments, thank you all.

Last but not least, I would like to express my gratitude to my family, my father and mother, Serafim and Rosita and my older brother, Renato for all the opportunities provided throughout my academical path, for all the support and appreciation for my efforts in these last few years, I wouldn't have made it this far if it wasn't for you.

Marcelo Rodrigo Magalhães Ramalho Mendes Lainho

Porto, February 2020

The project “MAMTool - Machinability of Additive Manufactured Parts for Tooling Industry” funded by the Programa Operacional Competitividade e Internacionalização, and Programa Operacional Regional de Lisboa funded by FEDER and National Funds (FCT) (Reference PTDC/EME-EME/31895/2017) are also acknowledged.

The project Add.Strength entitled "Enhanced Mechanical Properties in Additive Manufactured Components" funded by the Programa Operacional Competitividade e Internacionalização, and Programa Operacional Regional de Lisboa funded by FEDER and National Funds (FCT) is acknowledged (Reference PTDC/EME-EME/31307/2017). The BIC scholarship funded by the Add.Strength project is also acknowledged.

"Go as far as you can see; when you get there, you'll be able to see further"

Thomas Carlyle

Contents

1 Introduction **1**
- 1.1 Project's Framework and Motivation . . . 1
- 1.2 Objectives . . . 2
- 1.3 Structure . . . 2

2 Additive Manufacturing **5**
- 2.1 Introduction . . . 5
- 2.2 Metal Additive Manufacturing . . . 7
  - 2.2.1 Powder Bed Fusion . . . 8
  - 2.2.2 Process Parameters . . . 8
  - 2.2.3 Main Defects in LPBF . . . 10
  - 2.2.4 Materials . . . 12
- 2.3 Maraging Steel . . . 13
  - 2.3.1 Maraging Steel in Additive Manufacturing . . . 14
  - 2.3.2 Maraging Steel Applications . . . 16
- 2.4 Hybrid Manufacturing . . . 17

3 Metal Cutting **19**
- 3.1 Introduction . . . 19
- 3.2 Orthogonal Cutting . . . 19
  - 3.2.1 Mechanics of Orthogonal Cutting . . . 21
  - 3.2.2 Forces in Orthogonal Cutting . . . 22
- 3.3 Chip Formation in Metal Cutting . . . 25
  - 3.3.1 Chip Morphology . . . 27
- 3.4 Machinability . . . 27
- 3.5 Cutting Tools . . . 28
  - 3.5.1 Tool Materials . . . 28
  - 3.5.2 Tool Geometry . . . 30
- 3.6 Turning . . . 33
- 3.7 Milling . . . 35
- 3.8 Machinability of AM Materials . . . 40

4 Material Characterization and Experimental Procedure **43**
- 4.1 Introduction . . . 43
- 4.2 Chemical Composition . . . 43
- 4.3 Microstructure and Defects . . . 44
  - 4.3.1 Porosity . . . 44
  - 4.3.2 Microstructure . . . 47

4.4 Surface Roughness . . . 49
4.5 Compression Tests . . . 49
4.6 Hardness Measurements . . . 52
4.7 Turning Tests . . . 53
4.7.1 Turning Tests Setup . . . 53
4.7.2 Turning Parameters . . . 58
4.7.3 Surface quality . . . 58
4.8 Milling Tests . . . 59
4.8.1 Milling Tests Setup . . . 59
4.8.2 Milling Parameters . . . 62

5 Machining Tests Results and Discussion 65
5.1 Turning Tests . . . 65
5.1.1 Cutting Forces . . . 65
5.1.2 Cutting Power . . . 72
5.1.3 Specific Cutting Pressure . . . 73
5.1.4 Chip Morphology . . . 76
5.1.5 Tool Wear . . . 82
5.1.6 Surface Quality . . . 84
5.2 Milling Tests . . . 87
5.2.1 Cutting Forces . . . 87
5.2.2 Cutting Power . . . 96
5.2.3 Specific Cutting Pressure . . . 97
5.2.4 Chip Morphology . . . 99
5.2.5 Tool Wear . . . 102
5.2.6 Surface Quality . . . 105

6 Conclusions and Future Work 109
6.1 Conclusions . . . 109
6.2 Future Work . . . 110

References 113

A Codes and parameters for the turning experiments 117

B Average load values for the turning experiments 121

C Comparison between different turning tests 125

D Codes and parameters for the milling experiments 127

List of Figures

2.1 Schematics of a powder bed system. . . . 8
2.2 Classification of LPBF process parameters. . . . 9
2.3 Multiple types of laser scanning pattern strategies. . . . 9
2.4 Spherical porosities in LPBF material. . . . 10
2.5 LOF defects in LPBF fabricated parts: (a) poor bonding defects; (b) LOF defects with un-melted metal powders. . . . 11
2.6 SEM images of crack morphology and microstructure from the cross section of an LPBF fabricated Ti6Al4V: (a) crack morphology; (b) microstructure on both sides of the crack. . . . 12
2.7 Schematics showing (a–c) the formation process of microstructure in the maraging steel during the selective laser melting process, together with (d) a schematic thermal history of the sample by local laser heating. . . . 15
2.8 Different MAM materials as a function of mechanical properties (hardeness and yield strength). . . . 15
2.9 Part manufactured using an LBPF process made from maraging steel with conformal cooling channels. . . . 17
2.10 Cross-sectional view showing how an overbuilt part is machined using the combination of AM and machining. . . . 18
2.11 Schematic description of an hybrid (LPBF+Precision milling) process. . . . 18

3.1 (a) Typical accuracy and finish and (b) complexity and size achievable by machining, forming and casting. . . . 20
3.2 Classification of material removal processes. . . . 20
3.3 (a) Orthogonal cutting; (b) Oblique cutting. . . . 21
3.4 Orthogonal cutting variables. . . . 21
3.5 Forces acting on the chip in orthogonal cutting. . . . 23
3.6 Forces normalized in the direction that can be measured. . . . 24
3.7 Forces diagram showing geometric relations between N, F, F_s, F_n, F_c and F_t. . . . 25
3.8 Orthogonal cutting scheme showing primary and secondary shear zones. . . . 25
3.9 Chip formation mechanisms: (a) discontinuous, (b) continuous, (c) continuous with BUE, (d) serrated. . . . 26
3.10 Chip form classification according to ISO 3685 standard. . . . 27
3.11 Tool life affected by rake angle and feed rate. . . . 28
3.12 Components of resultant force depending on feed, cutting speed, tool cutting edge angle, and depth of cut (qualitative). . . . 29

3.13 Three ways of holding and presenting the cutting edge for a single-point tool: (a) solid tool, typical of HSS; (b) brazed insert, one way of holding a cemented carbide insert; and (c) mechanically clamped insert, used for cemented carbides, ceramics, and other very hard tool materials. . . . 31
3.14 Typical single-point tool geometry. . . . 32
3.15 (a) Positive (+) and (b) negative (-) rake angles. . . . 32
3.16 Small and large flank angle. . . . 33
3.17 Geometry of the turning process. . . . 34
3.18 Effect of geometric factors in determining the theoretical finish on a work surface for single-point tools: (a) effect of nose radius, (b) effect of feed. . . . 35
3.19 Face milling geometry. . . . 36
3.20 Different lead angle values (90º,75º and 45º) and its effects on the cutting performance. . . . 36
3.21 Cutting forces in milling operation. . . . 36
3.22 Up cut and down cut milling. . . . 37
3.23 Cutter diameter schematic. . . . 38
3.24 Total table feed length schematic. . . . 38
3.25 Components of cutting force in plain face milling. . . . 39
3.26 Tool-workpiece engagement variables in plain face milling. . . . 39

4.1 Optical microscope OLYMPUS PMG3. . . . 45
4.2 Image treatment for porosity analysis in the transverse to build direction: (a) original optical image, (b) binary image for porosity calculation. . . . 45
4.3 Schematics of different building directions (transverse and parallel to building directions). . . . 46
4.4 Schematic of the parallel and transverse to build surfaces analysed by optical microscopy. . . . 46
4.5 Eletrolytic etching equipment (Struers LECTROPOL-5). . . . 47
4.6 Optical images of eletrolitically etched surfaces: (a) and (b) transverse to build direction surfaces; (c) and (d) parallel to build direction surfaces. . . . 48
4.7 Optical image of lack-of-fusion defect with unmelted powder particles. . . . 48
4.8 Compression test machine (MTS 810) and samples setup. . . . 50
4.9 Compression testing samples drawing. . . . 50
4.10 Testing samples before (a) and after (b) the compression tests. . . . 51
4.11 True stress-strain curves for the three test samples (AM) and the conventional material. . . . 51
4.12 Hardness measuring machine (EMCO® Test M4U-075). . . . 52
4.13 Dynamometer and workpart setup in CNC machine. . . . 54
4.14 Technical drawing of tool holder for lathe chisel for axially mounted dynamometer, Type 9129AE25, Kistler®. . . . 54
4.15 Data acquisition setup . . . 55
4.16 Geometrical parameters of the turning inserts. . . . 55
4.17 Turning inserts, Palbit S.A.: (a) DCMW 11T304; (b) DCGT 11T304-FS. . . . 57
4.18 Toolholder geometrical features. . . . 57
4.19 MAS®MCV 1270 3-axis CNC machine. . . . 59
4.20 Milling tests setup. . . . 60
4.21 ADVANTECH portable data acquisition module. . . . 60
4.22 Geometrical parameters of the milling insert. . . . 61
4.23 Milling tool geometry and dimensional parameters. . . . 62

5.1 AM specimen load spectrum resulting from a cutting tool T2 (DCMW tool), v_c= 90 m/min, f= 0.2 mm/rev and a_p= 0.3 mm. 65
5.2 Evaluation of the feed force as a function of the feed rate for: (a) a_p=0.1 mm and v_c=150 m/min; (b) a_p=0.3 mm and v_c=150 m/min. 66
5.3 Evaluation of the penetration force as a function of the feed rate for: (a) f=0.05 mm/rev and v_c=150 m/min; (b) f=0.2 mm/rev and v_c=150 m/min. 67
5.4 Cutting force (F_c) evolution as a function of the turning parameters and the cutting tools for the both specimens (CV and AM). 69
5.5 Resultant force (F_R) evolution as a function of the turning parameters and the cutting tools for the both specimens (CV and AM). 70
5.6 Cutting force comparison between André's results and this thesis' results for an a_p= 0.3 mm and f= 0.2 mm/rev; (a) conventional material; (b) AM material. . . . 71
5.7 Cutting force comparison between André's results and this thesis' results for an a_p= 0. 1mm and f= 0.1 mm/rev; (a) conventional material; (b) AM material. . . . 71
5.8 Cutting power as a function of the feed rate for: (a) a_p=0.1 mm and v_c=150 m/min; (b) a_p=0.3 mm and v_c=150 m/min. 72
5.9 Cutting power as a function of the depth of cut for: (a) f=0.05 mm/rev and v_c=150 m/min; (b) f=0.2 mm/rev and v_c=150 m/min. 72
5.10 Specific cutting pressure, K_c, as a function of the cross-section area of undeformed chip, S, for the conventional and AM material and for the different tools, for a cutting speed, v_c=60 m/min. 73
5.11 Specific cutting pressure, K_c, as a function of the cross-section area of undeformed chip, S, for the conventional and AM material and for the different tools, for a cutting speed, v_c=90 m/min. 74
5.12 Specific cutting pressure, K_c, as a function of the cross-section area of undeformed chip, S, for the conventional and AM material and for the different tools, for a cutting speed, v_c=120 m/min. 74
5.13 Specific cutting pressure, K_c, as a function of the cross-section area of undeformed chip, S, for the conventional and AM material and for the different tools, for a cutting speed, v_c=150 m/min. 75
5.14 Chip morphology of the AM material obtained from the turning tests: (a) T1, v_c=60 m/min; (b) T1, v_c=90 m/min; (c) T2, v_c=60 m/min; (d) T2, v_c=90 m/min. . 77
5.15 Chip morphology of the conventional (CV) material obtained from the turning tests: (a) T1, v_c=60 m/min; (b) T1, v_c=90 m/min; (c) T2, v_c=60 m/min; (d) T2, v_c=90 m/min. 78
5.16 Chip morphology of the AM material obtained from the turning tests: (a) T1, v_c=120 m/min; (b) T1, v_c=150 m/min; (c) T2, v_c=120 m/min; (d) T2, v_c=150 m/min. 79
5.17 Chip morphology of the conventional (CV) material obtained from the turning tests: (a) T1, v_c=120 m/min; (b) T1, v_c=150 m/min; (c) T2, v_c=120 m/min; (d) T2, v_c=150 m/min. 80
5.18 Unused cutting inserts: (a)(b) DCGT tool (T1); (c)(d) DCMW tool (T2). 82
5.19 Tool wear detail of cutting tool DCGT (T1) used in the machining of the conventional material, for the specimen length L1: (a) rake face; (b) clearance face and tool tip edge. 83
5.20 Tool wear detail of cutting tool DCMW (T2) used in the machining of the conventional material, for the specimen length L3: (a) rake face; (b) clearance face and tool tip edge. 83

5.21 Tool wear detail of cutting tool DCMW (T2) used in the machining of the AM material, for the specimen length L4: (a) rake face; (b) clearance face and tool tip edge. . . . 83
5.22 SEM images of the cutting edge: (a) DMCW tool used in the machining of the AM specimen for section L4; (b) DCGT tool used in the machining of the conventional specimen for section L1. . . . 84
5.23 Sample length labelling for surface roughness measurements. . . . 84
5.24 Surface roughness as a function of the feed rate for an a_p = 0.1 mm. . . . 86
5.25 Section L1 detail. . . . 86
5.26 Surface roughness profile obtained with an optical profilometer for the AM sample machined with the parameters a_p=0.1 mm and f= 0.2 mm/rev: (a) 3D profile; (b) Surface roughness colour map; (c) Linear roughness profile. . . . 87
5.27 Load variation for one rotation of the spindle in the AM sample, for the parameters v_c=80 m/min, a_p= 0.2 mm and f_Z = 0.05 mm/tooth. . . . 88
5.28 Dynamometer fixture in the worktable and respective measured forces referential. 88
5.29 Schematic of the movements of the cutting edge on the workpiece for two consecutive turns of the milling tool. . . . 89
5.30 Load fitting comparison with the experimental data presented in Coelho et al. for an engagement angle of 100 %. . . . 91
5.31 Force data adjustment with the numerical model during the engagement for the AM material, v_c = 80 m/min, a_p = 0.6 mm and f_z = 0.2 mm/tooth . . . 92
5.32 Measured load for a cutting speed of 240 m/min in two consecutive tool full rotations, for an a_p= 0.2 mm and f_z=0.1 mm/tooth. . . . 93
5.33 Cutting force (F_c) evolution as a function of the milling parameters for both materials (AM and CV). . . . 94
5.34 Resultant force (F_R) evolution as a function of the milling parameters for both materials (AM and CV). . . . 95
5.35 Cutting power as a function of the feed per tooth for: (a) a_p = 0.2 mm and (b) a_p = 0.6 mm . . . 96
5.36 Cutting power as a function of the depth of cut for: (a) f_z = 0.05 mm/tooth and (b) f_z = 0.2 mm/tooth . . . 96
5.37 Specific cutting pressure calculated through Method 1 (M1). . . . 97
5.38 Specific cutting pressure as a function of the feed rate calculated through both methods, for the conventional material. . . . 98
5.39 Specific cutting pressure as a function of the feed rate calculated through both methods, for the AM material. . . . 98
5.40 Specific cutting pressure comparison between the milling and turning tests. . . . 99
5.41 SEM images obtained from the milling tests of the conventional (CV) material, v_c = 160 m/min, a_p = 0.2 mm, f_z = 0.05 mm/tooth . . . 100
5.42 SEM images obtained from the milling tests of the conventional (CV) material, v_c = 160 m/min, a_p = 0.6 mm, f_z = 0.2 mm/tooth . . . 101
5.43 SEM images obtained from the milling tests of the AM material, v_c = 160 m/min, a_p = 0.2 mm, f_z = 0.05 mm/tooth . . . 101
5.44 SEM images obtained from the milling tests of the AM material, v_c = 160 m/min, a_p = 0.6 mm, f_z = 0.2 mm/tooth . . . 102
5.45 XPET PDER-LP Milling insert: (a) rake face view; (b) clearance face view. . . . 102

5.46 Cutting insert used in the milling tests for machining of the conventional specimen for a cutting speed of v_c = 80 m/min: (a) and (b) optical images of the rake and clearance face, respectively; (c) SEM image of the cutting edge. 103
5.47 Cutting insert used in the milling tests for machining of the AM specimen for a cutting speed of v_c = 80 m/min: (a) and (b) optical images of the rake and clearance face, respectively; (c) and (d) SEM image of the cutting edge. 103
5.48 Cutting insert used in the milling tests for machining of the conventional specimen for a cutting speed of v_c = 160 m/min: (a) and (b) optical images of the rake and clearance face, respectively; (c) SEM image of the cutting edge. 104
5.49 Cutting insert used in the milling tests for machining of the AM specimen for a cutting speed of v_c = 160 m/min: (a) and (b) optical images of the rake and clearance face, respectively; (c) and (d) SEM image of the cutting edge. 104
5.50 Surface roughness comparison between both materials for all the cutting speeds . 106
5.51 Surface roughness profile obtained with an optical profilometer for the conventional sample for distinct cutting speeds (a) and (b) v_c = 80 m/min; (c) and (d) v_c = 160 m/min. 106

List of Tables

2.1 Main alloy/applications in Metal Additive Manufacturing. 13
2.2 Nominal compositions (wt%) and the respective strength of commercial maraging steels (Inco). 13
2.3 Commonly used materials in MAM. 16

3.1 Typical hardness values (at room temperature) and transverse rupture strengths for various tool materials. 30
3.2 Cutting tool materials with their approximate dates of initial use and allowable cutting speeds. 30
3.3 Conversion between orthogonal cutting and turning parameters. 33

4.1 Standard chemical composition of 18Ni300 maraging steel, conventional and AM sample composition. 44
4.2 Porosity results per surface analyzed. 47
4.3 Surface roughness measurements for the transversal and longitudinal surface. . . 49
4.4 Hardness (HV30) measurements for the different surfaces. 52
4.5 Cutting conditions for the experimental turning tests. 53
4.6 Inserts designation and dimensions. 56
4.7 Coating grade and respective description in accordance to Palbit S.A. catalogue. 56
4.8 Toolholder geometrical dimensions in accordance with Palbit S.A. catalogue . . 57
4.9 Different turning parameters and respective code. 58
4.10 Milling insert designation and geometrical dimensions. 61
4.11 Milling tool designation and geometrical dimensions. 61
4.12 Different milling parameters and respective code used. 62

5.1 Chip forms obtained in the turning tests. 76
5.2 Chip classification for each cutting parameter in accordance with the ISO 3685 standard. 81
5.3 Turning parameters for posterior surface roughness measurements and respective cutting speed (labelling used in the turning operations). 85
5.4 Surface roughness measurements for the turning samples. 85
5.5 Chips collection for milling tests overview. 100
5.6 Most abundant chemical components found in each zone. 105
5.7 Surface roughness measurements for the milling samples. 105

A.1 Operation codes adopted for each combination of parameters in the turning tests. 117
A.1 Operation codes adopted for each combination of parameters in the turning tests. 118
A.1 Operation codes adopted for each combination of parameters in the turning tests. 119

B.1 Average load values obtained in the turning experiments. 121
B.1 Average load values obtained in the turning experiments. 122
B.1 Average load values obtained in the turning experiments. 123

C.1 Comparison between André Couto's turning experiment main cutting force (F_c) results and this thesis results for the conventional material. 125
C.2 Comparison between André Couto's turning experiment main cutting force (F_c) results and this thesis results for the AM material. 126

D.1 Operation codes adopted for each combination of parameters in the milling tests. 127
D.1 Operation codes adopted for each combination of parameters in the milling tests. 128

Symbols and Acronyms

2D	Two dimensional
3D	Three dimensional
A	Cross-section area of an undeformed chip
a_e	Cutting width
AISI	American Iron and Steel Institute
ALE	Arbitrary Langragian Eulerian
AM	Additive Manufacturing
a_p	Depth of cut
ASTM	American Society for Testing and Materials
A_s	Shear plane area
BUE	Built-up edge
CAD	Computer-Aided Design
cBN	Cubic Boron Nitride
CNC	Computer Numerical Control
CV	Conventional material
DC	Direct Current
D_c	Cutter diameter
DED	Direct Energy Deposition
DIN	Deutsches Institut für Normung
DMLS	Direct Metal Laser Sintering
D_m	Workpiece diameter
DOD	Drop On Demand
EBM	Electron Beam Melting
EDM	Eletrical Discharge Machining
f	Feed rate
F	Friction force
F_c	Cutting force
FEA	Finite Element Analysis
FEM	Finite Element Method
F_f	Feed force
F_n	Normal force to shear
F_p	Penetration force
F_R	Average resultant force
F_s	Shear force
F_t	Thrust force
f_z	Feed per tooth
HDH	Hybride-Dehydride
HSS	High-speed steels

ISO	International Organization for Standardization
J-C	Johnson-Cook
K_c	Specific cutting pressure
l	Cutting length per minute
L	Total table feed length
LENS	Laser-Engineered Net Shaping
LOF	Lack-of-fusion
MAM	Metal Additive Manufacturing
N	Normal force to friction
n	Rotational spindle speed
PBF	Powder Bed Fusion
P_c	Cutting power
PVD	Physical Vapor Deposition
r	Chip thickness ratio
R	Resultant force
R_a	Surface roughness
r_e	Nose radius
R_{ta}	Theoretical arithmetic average of surface roughness
R_{tmax}	Maximum surface roughness
SEM	Scanning Electron Microscopy
SLM	Selective Laser Melting
SLS	Selective Laser Sintering
T	Temperature
t_0	Uncut chip thickness
t_c	Chip thickness after cut
T_c	Cutting time
T_m	Melting temperature
T_{room}	Room temperature
TT	Totally heat-treated
v_c	Cutting speed
v_f	Table feed per minute
w	Width of cut
Y_s	Yield Strength
z	Number of inserts

Greek letters

α	Rake angle
$\bar{\varepsilon}$	Equivalent plastic strain
β	Friction angle
$\dot{\bar{\varepsilon}}$	Equivalent plastic strain rate
$\dot{\bar{\varepsilon}}_0$	Reference equivalent plastic strain rate
ε	Strain
η	Machine coefficient of efficiency
μ	Friction coefficient
ϕ	Shear angle
σ	Flow stress
τ	Shear stress

Chapter 1

Introduction

1.1 Project's Framework and Motivation

Additive manufacturing technologies have a lot of advantages such as: the direct production from a CAD model, meaning that no tools and moulds are required (no switch over costs), designs in the form of digital files can be easily shared facilitating the customisation of components and products, complex structures otherwise unachievable through conventional manufacturing processes are possible [1]. Because of the inherent advantages of the AM processes, some of the more conventional manufacturing technologies are being replaced, for example in industries that have small production runs or where the geometrical complexity of parts is a requirement [2]. More specifically, the injection moulding industry currently benefits from AM by printing conformal channels that enable a more efficient cooling [3]. The need for high quality surface roughness as well as geometrical and dimensional tight tolerances bring to focus the need for post-processing of additively manufactured pats, in order to be successfully integrated in functional assemblies. Metal cutting is often employed as a post-processing stage which brings to focus the main goal of this dissertation, which consists of the machinability assessment of additively manufactured maraging steel as well as its comparison with the conventionally fabricated.

Most of the additivelly manufactured metallic components are subjected to post-processing processes, mainly composed of metal cutting operations. Regarding this fact, the machinability assessment and evaluation of the AM parts need to be evaluated, since important aspects such as microstructure, anisotropic structure and residual stresses are distinct from the conventionally produced components which, may in turn lead to a different behaviour when subjected to metal cutting operations. Also, the importance of choosing the proper cutting conditions needs to be evaluated in order to obtain the desired geometrical tolerances and surface quality these components usually have tight requirements for.

Cutting forces measurement has allowed the identification of the cutting power as well as the specific cutting pressure, which constitute important measures regarding load estimation according to distinct cutting parameters. Their monitoring helps to understand the stability of the cutting

process allowing for the identification of the proper cutting conditions and, for example, the occurrence of tool wear. Also, in order to understand the machinability properties of the AM material, due to the inherent microstructural differences between the additivelly manufactured and conventionally manufactured materials, several machinability aspects will be evaluated and compared with the conventional material.

Machinability studies of AM materials are an important research subject in the field of hybrid manufacturing technologies, since these technologies integrate both manufacturing processes into a single machine.

The present work integrates the MAMtool research project of INEGI - Institute of Science and Innovation in Mechanical and Industrial Engineering by providing machinability studies of either conventionally and AM produced 18Ni300 maraging steels.

1.2 Objectives

The main purpose of this dissertation is the machinability evaluation of conventionally and additively manufactured 18Ni300 maraging steel. The following tasks are envisaged:

- Literature review on the additive manufacturing technologies, focusing on Powder Bed Fusion (PBF) of maraging steel as well as metal cutting of the steel in question;
- Metalographic characterization of the AM samples through chemical analysis, microstructure evaluation, hardness, porosity measurement and quasi-static compression tests;
- Experimental metal cutting tests (turning and milling) with cutting load measurement analysis for both AM an conventional 18Ni300 maraging steel;
- Chip analysis and tool wear evaluation for different cutting conditions in order to assess the different materials' machinability;
- Surface roughness measurement of milling and turning surfaces and comparison with the conventional steel;
- To assess the materials' machinability through the evaluation of the specific cutting pressure.

1.3 Structure

The structure of this dissertation is divided into several chapters, organized as follows:

- **Introduction**: A summary of the project's framework and motivations and this dissertation's goals;
- **Additive Manufacturing**: Literature review about additive manufacturing, namely the metallic powder based processes, focusing on the LPBF manufacturing process of additively manufactured maraging steels;

- **Metal Cutting**: An introduction to metal machining, mechanics of the process, chip formation, machinability evaluation, cutting tools and hybrid manufacturing processes;
- **Material Characterization and Experimental Procedure**: Metalographic characterization of the AM material, turning and milling tests setups and parameters (testing matrix);
- **Machining Tests Results and Discussion**: Cutting forces analysis, chip geometry evaluation, cutting tools damage, surface quality and specific cutting pressures analysis;
- **Conclusions and Future work**: Main conclusions derived from this investigation and complimentary future works proposal.

Chapter 2

Additive Manufacturing

2.1 Introduction

Additive Manufacturing (AM) is the official terminology (according to ASTM F2792 Standard) used for the technological processes that use a 3D CAD Model to produce objects using a layer by layer methodology, as opposed to more conventional methods such as subtractive or forming technologies (e.g. metal cutting, metal forging). Over the years, with the industry development and the need to build prototypes for numerous applications began the research on AM technologies, originally known as Rapid Prototyping, because the main application was to make inexpensive prototypes during the development stage of a determined product in order to overcome design flaws and overall usability [4]. Nowadays the technology has evolved from simple prototypes to the manufacturing of complex functional parts, with different materials and applications [5].

The primary applications of additive manufacturing are design/modelling, fit and function prototyping and direct part production. When used correctly, AM can save large amounts of time and money by minimizing elapsed time in stages such as design and prototyping. Traditional manufacturing methods usually involve material remotion into the desired part, whereas AM, instead of removing material from a raw shape, starts from scratch adding thousands of small layers of material to achieve the desired volumetric shape [5].

The methodology adopted in AM technologies is common throughout the different processes and consists in modelling the desired part in a CAD software. The next step is to convert the CAD file into a standard format compatible with AM processing, such as `.STL` `.AMF` or `.3MF` [6]. The processing software proceeds to a "slicing" stage which consists in dividing the part into thousands of thin 2D layers. The final stage consists of uploading the processed file onto the machine and the printing will start. After this stage, the parts might undergo post-processing treatments such as, heat-treatment and others, in order to remove the substrate (support parts that don't belong to the part structure) and to achieve the desired shape and surface roughness [5].

Initially, AM technologies were introduced for the development of polymeric materials prototypes, wax based models and paper laminates. Currently, with the development of new types

of AM processing technologies it is possible to make functional components out of metals, polymers, ceramics, and composites [5]. Presently, AM technologies are used for a wide range of applications, such as the production of ready-to-use parts for aircraft/aerospace industry, medical implants, automobile parts and even fashion products [6]. In order to achieve the best results in the different processes of 3D printing, several materials were developed in order to achieve the best printing properties and thus, allowing for better printing accuracy, durability and overall strength.

AM is revolutionizing the way companies design and develop new components. Complex parts are cheaper to produce than a solid cube of the same material because the more complex (or, less solid the object is), the faster and cheaper it can be produced through additive manufacturing. AM technologies allow much more freedom in terms of design adjustments and optimization; these changes can be made by only changing the CAD file and uploading it to the printer, whereas in a die casting, the whole mould had to be re-machined or made from scratch. Another advantage when compared to conventional methods lies in the reduced number of parts that AM technologies allow; as for example the reduction of the required number of fixtures (hinges).

Lead time is also an important aspect in all production processes. In the case of AM technologies, the engineer can start the production of a prototype after finishing the design in a CAD software. As soon as the part is finished and post-processing procedures are completed, testing can begin, instead of waiting weeks or months for a functional prototype to be made using conventional processes. When using a conventional procedure such as injection moulding, the number of design constraints is very high due to the limitations of the process. In AM technologies, this number is much lower, allowing for a wide variety of complex designs that would be very difficult to achieve using conventional methods.

However, as for all production processes, some limitations need to be taken into account when evaluating if AM processes could be the most adequate solution. The build rates are slower when comparing with other technological processes, many printers lay down material at a rate of roughly 0.08 cubic decimeters per hour. High production costs are also one main disadvantage when it comes to AM; sometimes components can be made faster and cheaper using other techniques, so the extra time can lead to higher costs. High-end additive manufacturing machines are also very expensive such as the printing material and general machine maintenance. Additionally, the components require post-processing methods in order to achieve the desired shape and surface finish. One of the major drawbacks of AM technologies is the overall product quality after production. Given the fact that it is a layered construction method, mechanical properties could be anisotropic and a good surface roughness is difficult to obtain [7].

According to the ISO/ASTM 52900 [8] standard AM technologies are divided into seven categories:

- **Material extrusion:** Material is drawn through a nozzle, where it is partially fused and deposited layer by layer. Materials used are mostly thermoplastics;
- **Material jetting:** Material is jetted onto a building platform using a continuous or drop on demand (DOD) approach. This process is similar to a two dimensional ink jet printer;

- **Binder jetting:** process in which a powder based material is joined together by a liquid bonding agent;
- **Sheet lamination:** sheets of material with the desired shape (such as papers layers) are joined together to form a part;
- **VAT Photopolymerization:** process in which a vat of photopolymer resin is selectively cured by light-activated polymerization;
- **Powder bed fusion:** process that using thermal energy, such as a laser or beam, selectively fuses regions of a powder bed;
- **Direct energy deposition:** process in which focused thermal energy is used to fuse materials by melting as they are being deposited.

2.2 Metal Additive Manufacturing

Metal additive manufacturing (MAM) is a rapidly growing category of technologies and, throughout the years, has been replacing other fabrication methods in some industries. Given the ability to produce very complex components with little to no constraints when compared to, for example, an high pressure die casting process, it allows for a major improvement in the customization of the parts.

The main categories of metal additive manufacturing are categorized in terms of the feed stock material, energy source, build volume, etc. MAM systems are divided into four major categories:

- Powder bed fusion (PBF);
- Directed energy deposition (DED);
- Sheet lamination;
- Binder jetting.

Each of these categories have several specific technological processes, according to several aspects such as energy source, type of feedstock and energy deposition method. For example, metallic powder bed fusion (PBF) processes can be subdivided into Direct Metal Laser Sintering (DMLS), Electron Beam Melting (EBM), Selective Laser Melting (SLM), Directed Energy Deposition (DED) can be subdivided into Electron Beam Additive Manufacturing (EBAM) and Laser-Engineered Net Shaping (LENS) [9]. The main focus of this dissertation is the Laser Powder Bed Fusion (LPBF).

2.2.1 Powder Bed Fusion

Powder bed fusion processes allow the fabrication of functional components with high structural density at a relatively low cost when compared to the production of a mould for example, allowing for several materials to be used, including bio-compatible titanium alloys. One of the main drawbacks in this process is the variable surface finish, which can compromise aesthetic and technical function.

In LPBF, parts are fabricated layer by layer using the action of a high-energy laser beam on several regions of the powder bed, in order to fully melt the metal and aggregate the powder particles into the intended design. The process uses either a roller or a blade to spread new layers of powder over previous layers. When the blade sweeps across the powder bed, it often vibrates to ensure a better distribution of powder. A reservoir is stored below or aside the bed to provide a fresh layer of powder [9].

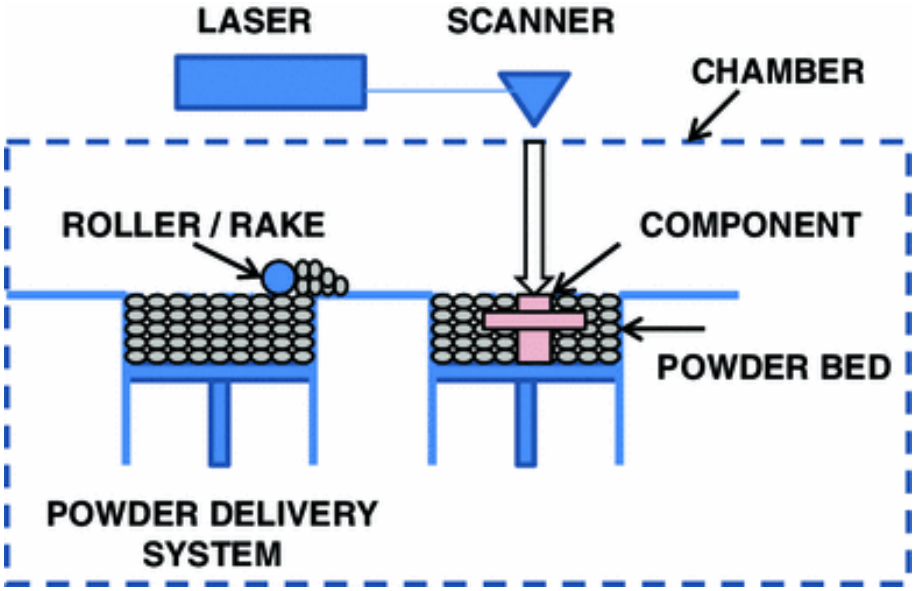

Figure 2.1: Schematics of a powder bed system [10].

The building process starts with the deposition of the first layer of powder (typically 0.1 mm thick [9]), afterwards the laser melts the first layer or first cross section of the model. When the first step is finished, the building platform descends and a new layer of powder is spread out across the previous layer by means of a roller or a rake, and the fusing step begins again. This process is repeated until the entire model is completed. The unmelted powder is removed and the part is ready for post-processing procedures (e.g. removal of support structures).

2.2.2 Process Parameters

Laser Powder Bed Fusion (LPBF) is a technological process in which many building parameters are involved. In order to satisfy the required build quality for each project, these parameters

need to be carefully studied. The main categories of the process parameters can be divided into: laser-related, scan-related, powder-related and temperature-related, as can be seen in figure 2.2. Typical scan pattern strategies are illustrated in Figure 2.3.

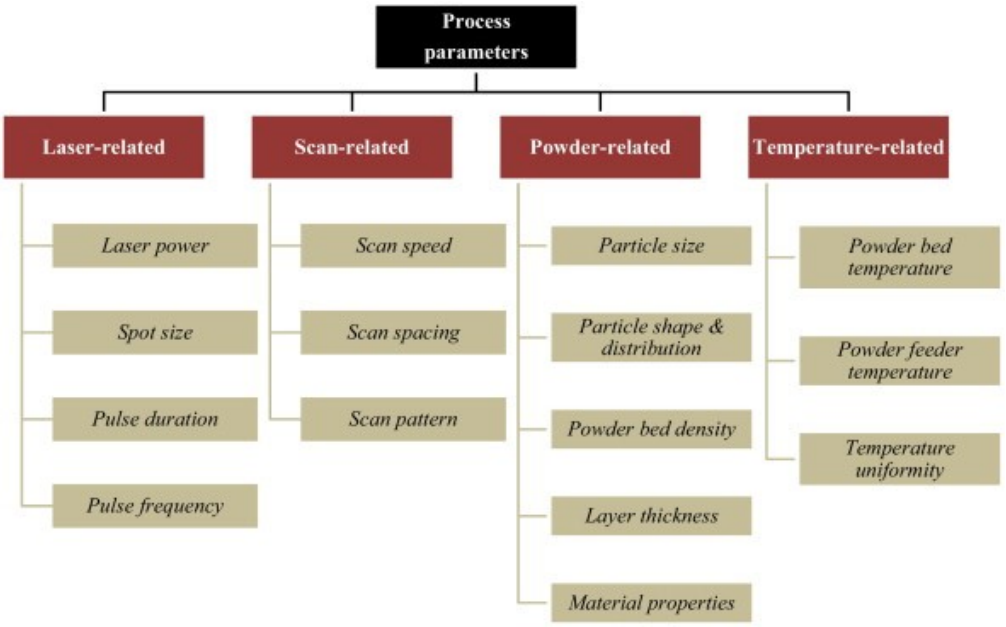

Figure 2.2: Classification of LPBF process parameters [11].

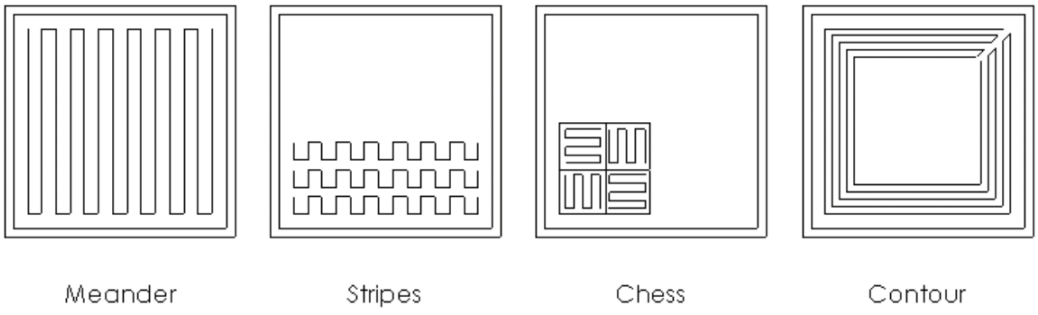

Figure 2.3: Multiple types of laser scanning pattern strategies [12].

2.2.3 Main Defects in LPBF

Although the LPBF process offers a great advantage in manufacturing complex parts at a high material utilization rate, it is affected by many factors such as laser energy input/scanning speed, scan strategy, powder material, powder size and morphology [13]. The LPBF process consists of complex physics, such as absorption and transmission of laser energy, rapid melting and solidification of the material, microstructure evolution, flow in a molten pool and materials evaporation. The process is thus affected by the aforementioned factors to form defects such as porosities, incomplete fusion holes, cracks, impurities, etc [13]. These defects are detrimental to the overall quality of a fabricated part in terms of its mechanical and physical properties, which in turn limits the application of LPBF. Many parameters are involved in an LPBF process, such as laser power, scan speed, hatch spacing, layer thickness, powder materials and chamber environment.

2.2.3.1 Porosity

Pores are a very usual defect in selective laser melted samples and may become a detrimental aspect in their mechanical behaviour [14]. Porosity can occur if the packing density of the powders is low, which in turn can lead to gas presence between the powder particles, not dissolving in the molten pool. The insolubility of gas particles in the molten pool is mainly related to the high cooling rate during the solidification process of the molten material, which causes gas particles to be trapped in the molten pool. Porosities are thus formed and remain in the solidified finished part [13].

Another cause for porosity occurrence is the correlation between gas solubility and the high temperature of liquid metal due to high laser intensity, which can lead to an increase in gas enrichment of the molten pool. Additionally, in the process of powder preparation, gas is inevitably introduced in the powder materials [13].

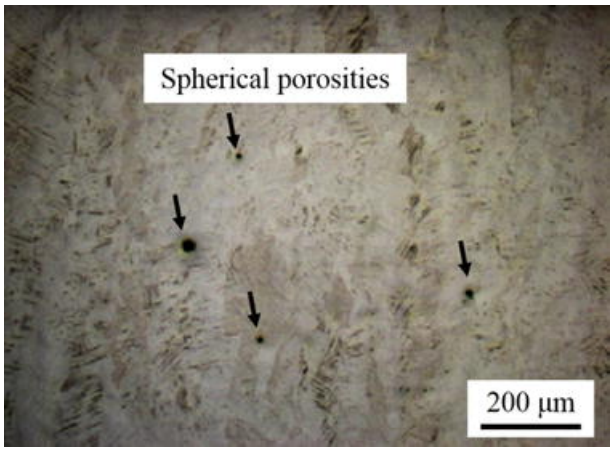

Figure 2.4: Spherical porosities in LPBF material [13].

Spherical porosity is generally caused by entrapped gas bubbles in the molten pool. Gas bubbles are generated when high laser energy is induced in the molten pool, which forms the

regular spherical porosities seen in Figure 2.4.

Another typical occurrence in the LPBF process is called balling phenomenon, which consists of a regrouping of powder particles due to heterogeneous heating, which can be related to a very high scan speed, causing discontinuities in the scan path [15].

2.2.3.2 Incomplete fusion holes

Incomplete fusion holes, commonly known as lack-of-fusion (LOF) defects are related to the lack of energy input in the LPBF process. The formation of these defects is due to the lack of fusion of the metallic powder in order to deposit a new layer on top of the previous layer with a sufficient overlap that allows the bonding of subsequent layers together. Two types of LOF defects can occur: poor bonding defects due to a reduced molten pool during a solidification process 4.7 (a), and defects with unmelted metallic powders 4.7 (b) [13].

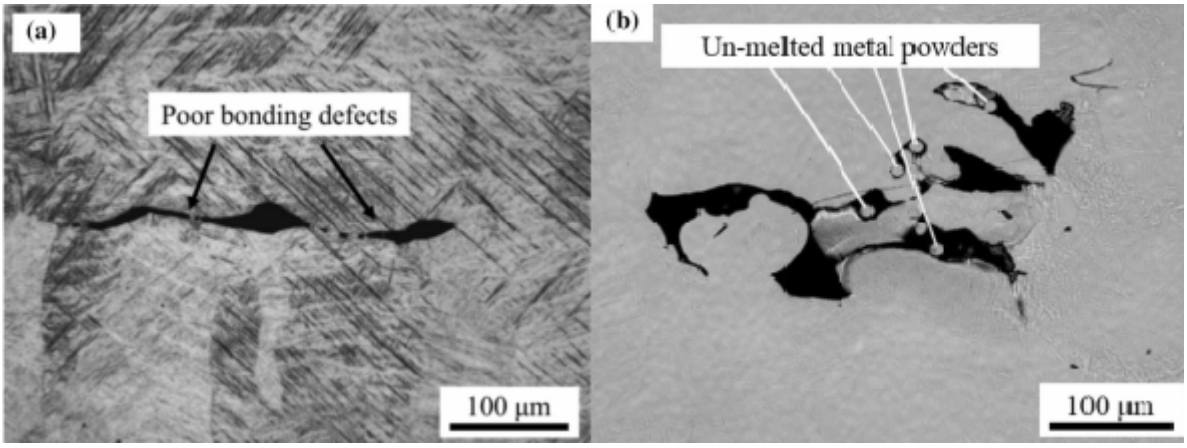

Figure 2.5: LOF defects in LPBF fabricated parts: (a) poor bonding defects; (b) LOF defects with un-melted metal powders [13].

2.2.3.3 Cracks

In an LPBF process the metal powders experience high temperature fluctuation due to the rapid melting and rapid solidification as a result of high local laser energy input. The cooling rate of the molten pool can reach values up to 10^8 K/s [13], which leads to a very high temperature gradient and in turn induces a large amount of residual thermal stresses in the part. Combined, these factors may lead to cracking in a fabricated part.

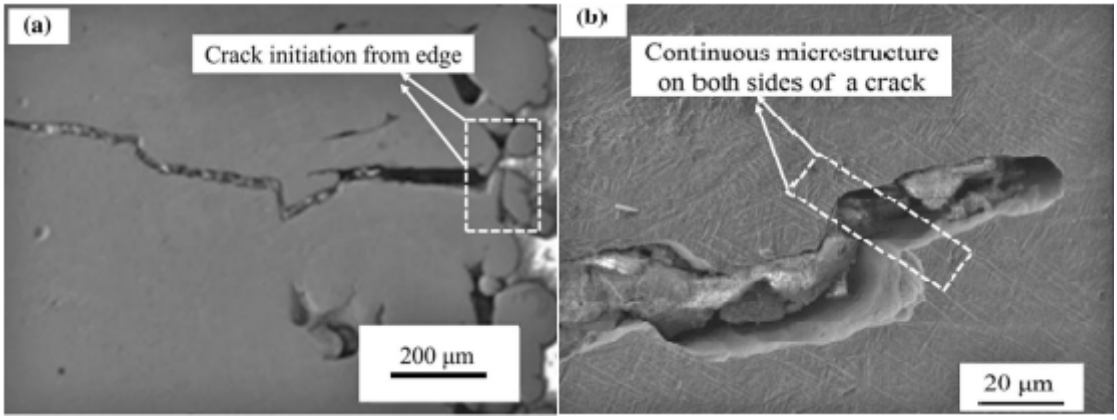

Figure 2.6: SEM images of crack morphology and microstructure from the cross section of an LPBF fabricated Ti6Al4V: (a) crack morphology; (b) microstructure on both sides of the crack [13].

2.2.4 Materials

With the technological development of AM processes a wider range of materials can be used. Increasingly, more interest revolves in high performance metals due to the fact that AM processes offer significantly better options in terms of part complexity and economic advantage. These metals have been studied and implemented in AM processes due to their widespread application and overall material cost [16]. Main metal categories used in LPBF are:

- **Steel and Iron based alloys**: 316L Stainless Steel, AISI Maraging 300 steel, H20 tool steel, 904L Stainless steel, Fe-Ni-Cr, Fe-Al, Fe-Cr-Al, Fe-Ni, Fe-Ni-Cu-P alloys [16];

- **Titanium based alloys** : Commercially pure Titanium (cpTi), Ti-6Al,4V (Ti64), Ti-6Al-7Nb, Ti-24Nb-4Zr-8Sn, Ti-13Zr-Nb, Ti-13Nb-13Zr alloys [16] ;

- **Nickel base alloys**: Inconel (625,718), Chromel, Hastelloy X, Nimonic 263, NiTi alloy [16];

- **Aluminium based alloys**: AlSi12 (DIN 3.3581), AlSi10Mg (DIN 3.2381) [17];

The most common material applications in Metal Additive Manufacturing (MAM) range from aerospace applications to consumer products and biomedical parts. The following table (Table 2.1) relates the main applications with the most common metal alloys used in AM processes.

Table 2.1: Main alloy/applications in Metal Additive Manufacturing. [18]

Alloys ⇨ Applications ⇩	Aluminum	Maraging steel	Stainless steel	Titanium	Cobalt chrome	Nickel super alloys	Precious metals
Aerospace	X		X	X	X	X	
Medical			X	X	X		X
Energy, oil and gas			X				
Automotive	X		X	X			
Marine			X	X		X	
Machinability and weldability	X		X	X		X	
Corrosion resistance			X	X	X	X	
High temperature			X	X		X	
Tools and molds		X	X				
Consumer products	X		X				X

2.3 Maraging Steel

Maraging steel is typically known for having excellent mechanical properties, thus considered an ultra high strength steel, very commonly used in aeronautical/aerospace industry. Due to the fact that they are not hardened by carbon (this alloying element is, in fact, considered an impurity, therefore its presence as an alloying element is kept as low as commercially possible) maraging steel constitutes a class of their own [19]. Mainly, these alloys are composed of Iron (65-75% Fe) and Nickel (17-26% Ni), thus are considered Fe-Ni alloys. The word "maraging" can be decomposed in two parts: "mar" (from the word martensite) and "aging", related to the ageing of martensite (a hard microstructure commonly found in steels) [20]. The only transformation that occurs at ordinary cooling rates is martensite transformation. Typically, hardening and strengthening of these alloys are obtained by ageing heat treatment for several hours at around 480-510ºC [19]. Instead of the typical carbide precipitation, maraging steels are hardened by the precipitation of intermetallic compounds. The absence of carbon as an alloying element grants significantly better hardenability, formability and a combination of strength and toughness [19]. The common composition of commercial grade maraging steels (developed by *Nickel Ltd. (Inco)*) can be found in Table 2.2.

Table 2.2: Nominal compositions (wt%) and the respective strength of commercial maraging steels (Inco). [19]

Alloy designation	Ni	Mo	Co	Ti	Al	Y_S (MPa)
18Ni (200)	18	3.3	8.5	0.2	0.1	1400
18Ni (250)	18	5.0	8.5	0.4	0.1	1700
18Ni (300)	18	5.0	9.0	0.7	0.1	2000
18Ni (350)	18	4.2	12.5	1.6	0.1	2400
18Ni (cast)	17	4.6	10.0	0.3	0.1	1650

Maraging steels have a large number of alloying elements, and have an ultra high yield strength (Y_S in table 2.2) when compared to standard yield strength of structural steel grades (ranging from 275 to 355 MPa) resulting in very high production costs [19]. Over the past fifty years, two major types maraging steels were developed, cobalt-free alloys and 18Ni steels. The latter (18Ni) are in a more advanced stage of development and applications, with maximum strength levels reaching

values up to 2400 MPa, while also having good levels of toughness and ductility. Nonetheless, these steels contain a very expensive alloying element, Cobalt with weight percentages between 8 and 13 %. This is the main reason why these steels have a very expensive production/commercial cost. As a result, cobalt-free maraging steels were developed, in order to provide a more economical alternative while maintaining outstanding levels of strength (2000 MPa). Cobalt-free alloys provide a good alternative to the conventional 18Ni-type maraging steels, allowing for a wider range of applications [19].

2.3.1 Maraging Steel in Additive Manufacturing

Maraging steels are widely used in AM powder bed fusion processes due to their good weldability which is related to the very low presence of interstitial alloying elements [21] and being relatively soft after cooling from austenitizing temperatures [22]. Maraging steels are a suitable material for the Selective Laser Melting process in terms of microstructure development and weldability properties. The extreme local heating by action of a laser-beam produces melt pools, followed by high cooling rates which in turn results in rapid solidification. During the cooling process, the areas irradiated by the laser-beam are rapidly quenched from the austenitic region to reach temperatures lower than the martensite start temperature, which results in formation of martensitic structures that contribute to the strengthening of these materials. The overall strength level of a LPBF maraging steel part is around 1 GPa [23]. After the LPBF process is concluded, parts are submitted to an ageing treatment at relatively high temperatures (≈480ºC) that enhances the precipitation of intermetallic phases in the martensitic structure that, consequently increases strength properties of these steels [23].

Figure 2.7 illustrates the microstructure formation during a LPBF process. The laser irradiated areas heat up and form a melt pool. The primary solid (austenite) is formed in the interface between solid and liquid phases and propagates to the center of the melt pool, which is the point of highest temperature under the laser-beam irradiation in solidification. When the temperature drops to a certain value, below the martensite formation temperature, the solidified austenite grains transform into martensite [23].

Maraging steel 18Ni300, commonly known as "grade 300 maraging steel" (European material number 1.2709), is used almost exclusively in AM processes [21]. The variety of materials used in metal AM processes is continuously expanding, with the development of technologies and further material researches. The most commonly used materials in these processes are shown in Table 2.3. This wide range of materials allows the user to choose the right material according to the specifications of the product [24] . Figure 2.8 compares different materials used in MAM in terms of hardness and yield strength. Note that maraging steel (material 1.2709) is at the top of the graph due to its excellent mechanical properties obtained in AM processes.

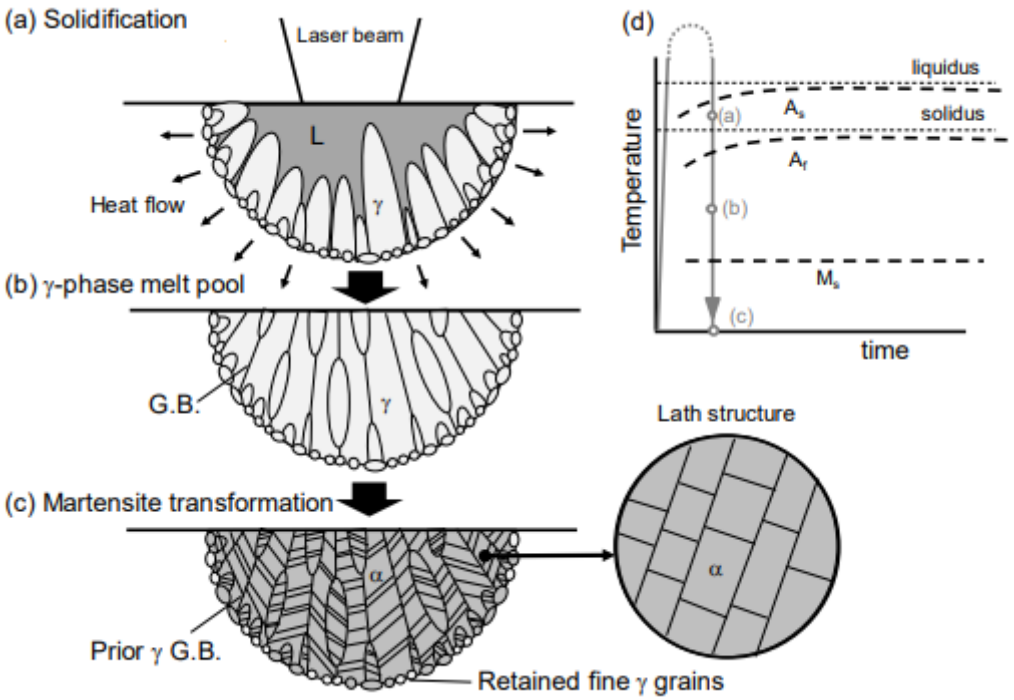

Figure 2.7: Schematics showing (a–c) the formation process of microstructure in the maraging steel during the selective laser melting process, together with (d) a schematic thermal history of the sample by local laser heating [23].

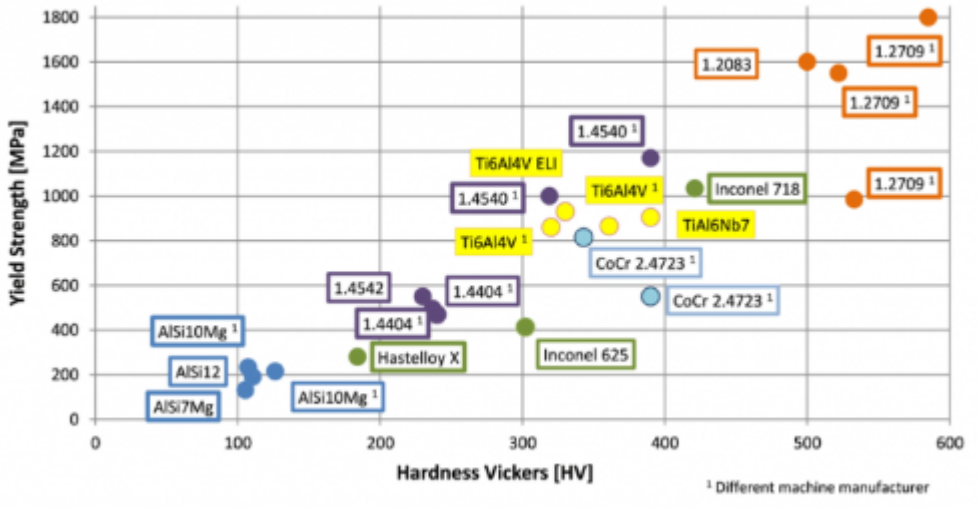

Figure 2.8: Different MAM materials as a function of mechanical properties (hardeness and yield strength) [24].

Table 2.3: Commonly used materials in MAM [24].

	Material	DIN
Aluminium Alloys	AlSi10Mg	3.2381
	AlSi7Mg	3.2371
	AlSi12	3.3581
Cobalt Based Alloys	ASTM F75	2.4723
	CoCrWC	
Tool Steels	AISI 420	1.2083
	Marage 300	1.2709
	H13	1.2344
	AISI D2	1.2379
	AISI A2	1.2363
	AISI S7	1.2357
Nickel Based Alloys	Inconel 718	2.4668
	Inconel 625	2.4856
	Inconel 713	2.4670
	Inconel 738	
	Hastelloy X	2.4665
Stainless Steels	SS 304	1.4301
	SS 316 L	1.4404
	SS 410	1.4006
	SS 440	1.4110
	15-5 PH	1.4540
	17-4 PH	1.4542
Titanium Alloys	Titanium Grade 2	3.7035
	Ti6Al4V	3.7165
	Ti6Al4V ELI	3.7165 ELI
	TiAl6Nb7	
Precious Metal Alloys	Jewellery Gold	18 Carat
	Silver	930 Sterling
Copper Alloys	CC 480 K	2.1050

2.3.2 Maraging Steel Applications

Given the unique properties of maraging steels (high tensile strength and good ductility), these alloys are used in applications with these requirements such as: aerospace engineering, where wing fittings are made from these materials due to its durability; fastening components to hold parts together in a reliable way as well as machinery parts, are some of the common applications of maraging steel. Some applications where demanding power/propulsion ratio is required (due to fuel consumption) also benefit from this material, specially since it is available as metal sheet as stock material [25].

The stable physical properties of maraging steel makes it an excellent choice for machinery components that work in a high temperature gradient in which the thermal stability plays a crucial role in the material choice. Some examples for machinery applications are: engine crankshafts,

weapon firing pins, gearboxes, etc.

One of the main interests of the LPBF process is the ability to produce parts with complex geometries, such as internal cooling channels that can be much more complex than the ones manufactured with conventional methods. Maraging steel is a great choice material-wise for mould applications with conformal cooling channels, given its ability to be thermically stable, corrosion resistant, wear resistant and its good fatigue properties. An example of a part manufactured using maraging steel with internal conformal cooling channels is illustrated in Figure 2.9. The use of this type of steel can improve moulds' life cycle and significantly reduce tool wear, while providing a better solution for conformal cooling if manufactured by an LPBF process.

Figure 2.9: Part manufactured using an AM process made from maraging steel with conformal cooling channels [26].

2.4 Hybrid Manufacturing

Additive manufacturing offers great advantages but one of its major drawbacks is the poor surface finish and geometrical accuracy when compared to conventional manufacturing processes, requiring post-processing operations in order to achieve the desired finish quality. Regarding this requirement, new types of systems have been developed in order to join additive and subtractive manufacturing processes in a single machine. One of the major advantages of these types of machines is the elimination of the "stair" effect present in AM produced parts because of the layer overlap by employing a cutting tool that greatly improves surface quality, an example of this solution is present in Figure 2.10. When using a difficult to machine material, an hybrid manufacturing process can be used in order to reduce tool wear and chip waste because of its ability to produce near-net shapes that require less machining than the conventional processes [27]. A schematic of an hybrid process is illustrated in Figure 2.11.

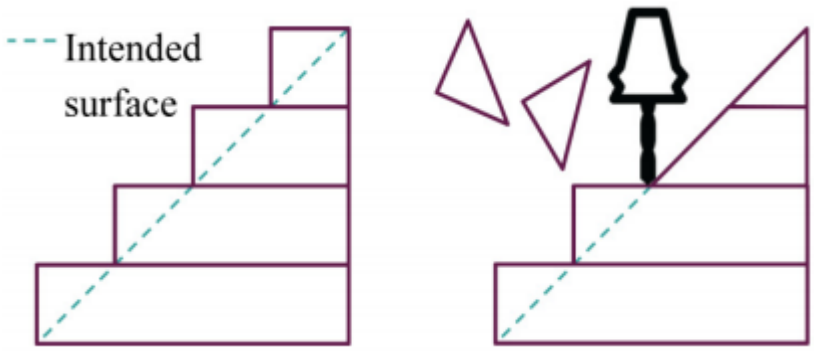

Figure 2.10: Cross-sectional view showing how an overbuilt part is machined using the combination of AM and machining [27].

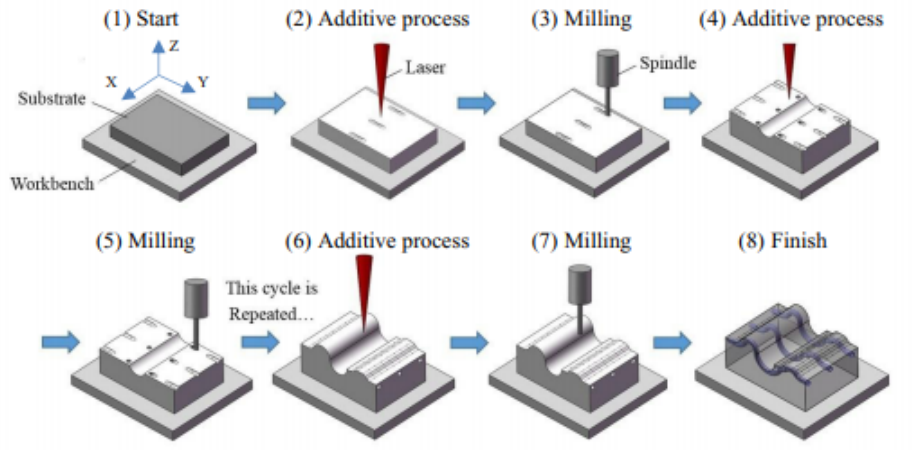

Figure 2.11: Schematic description of an hybrid (LPBF+Precision milling) process [27].

Chapter 3

Metal Cutting

3.1 Introduction

Metal cutting processes consist of shaping operations in which material is removed by cutting away excess material using a cutting tool, in order to achieve the desired geometry. The predominant mechanism involved is shear deformation of the work material to form a chip, and as this chip is removed a new surface is exposed [28]. One of the reasons this technology is so broadly used is the possibility in attaining excellent precision, geometrical and dimensional tolerances as well as surface finish. Another reason these processes are so widely used is the versatility that metal machining has, allowing the manufacturing of complicated free-form shapes (with some restrictions) with many features at a relatively low price, when compared to the investment of time and money in manufacturing a dedicated moulding, die casting or forging tool (besides, machining is needed to make the dies for these processes) [29]. The comparison between machining and other conventional manufacturing processes can be seen in Figure 3.1.

Metal cutting operations can be divided into three major categories: Conventional machining in which a sharp cutting tool is used to mechanically cut the working material to achieve the desired shape, abrasive processes, in which hard, abrasive particles mechanically remove the material and finally, nontraditional processes that use different forms of energy to remove material (e.g. Electrical Discharge Machining (EDM)) [28]. The main focus of this dissertation will be conventional machining processes, which are mainly composed by turning, milling and drilling. A list of the different material removal processes can be seen in Figure 3.2.

3.2 Orthogonal Cutting

The mechanics of most machining operations are very challenging to analyze because of the many different parameters involved, therefore the need to find a simplified machining model that describes correctly the chip formation mechanism, while neglecting many of the geometric complexities is essential. Orthogonal cutting is the most simplified model for mechanical analysis of machining. Most metal cutting operations (e.g. milling, turning) are three dimensional (oblique)

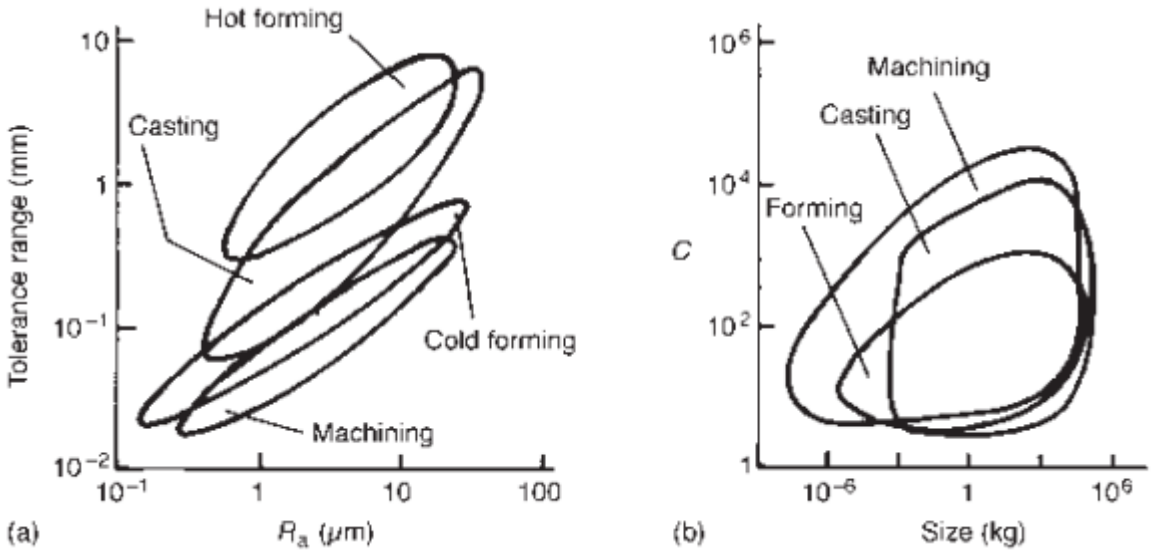

Figure 3.1: (a) Typical accuracy and finish and (b) complexity and size achievable by machining, forming and casting processes [29].

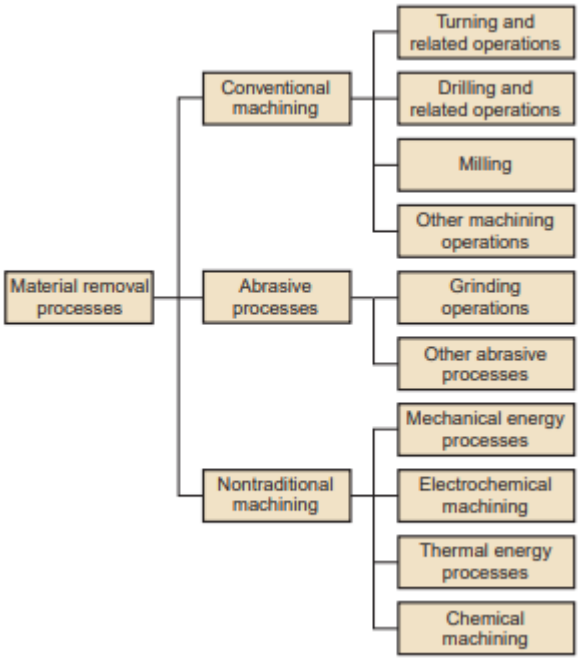

Figure 3.2: Classification of material removal processes [28].

unlike the two-dimensional orthogonal cutting model [28]. Oblique cutting gets the designation due to the angle between the cutting velocity and the cutting tool edge as can be seen in Figure 3.3, introducing a third force component.

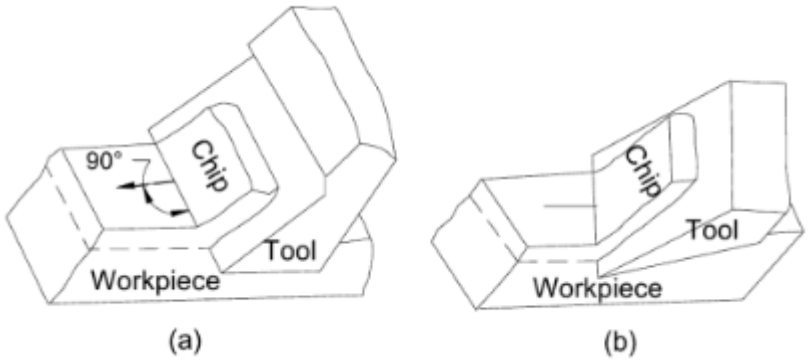

Figure 3.3: (a) Orthogonal cutting; (b) Oblique cutting [30].

3.2.1 Mechanics of Orthogonal Cutting

Orthogonal cutting is used to describe the mechanics of metal cutting in a simplified manner while at the same time representing a reasonable description of the process. By definition, orthogonal cutting uses a wedge-shaped tool in which the cutting edge is orthogonal to the direction of the cutting speed. As the tool advances into the workpiece, a chip is formed by shear deformation in the shear plane (oriented at an angle ϕ), and it is along this plane that most of the energy is consumed due to plastic deformation [28]. The orthogonal cutting tool only has two elements of geometry: rake angle (α) and clearance angle. Rake angle can be positive or negative and determines the chip flow direction; whereas the clearance angles provides a small clearance space between the tool flank and the new workpiece surface, preventing friction between the tool and the newly generated surface, avoiding damaging it [28]. Both angles can be seen in Figure 3.4.

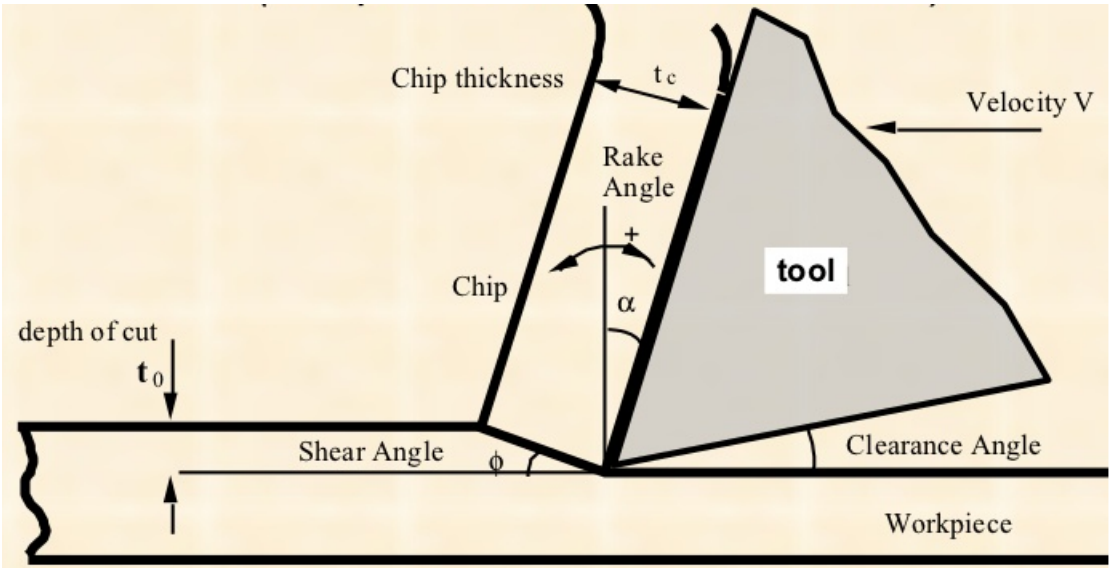

Figure 3.4: Orthogonal cutting variables [31].

Uncut chip thickness (t_0) is defined as the distance at which the edge of the cutting tool is positioned with respect to the original workpiece surface. In orthogonal cutting model, the cutting is assumed to be uniform along the cutting edge (along w direction), therefore it is a two-dimensional plane strain deformation process, unlike oblique cutting [32]. Two cutting forces are developed, one in the direction of the cutting velocity labeled cutting force (F_c) and another on the direction of the uncut chip thickness, denominated thrust force (F_t). The chip thickness increases along the shear plane while its being removed from the material and is defined as t_c and can be related with uncut chip thickness (t_0) by the chip thickness ratio or simply chip ratio, r [28]:

$$r = \frac{t_0}{t_c} \tag{3.1}$$

Since the chip thickness after cutting is always greater than the uncut chip thickness, the chip ratio is always less than 1.0. The geometry of the orthogonal cutting model allows the definition of an important geometrical relationship between the rake angle (α) and the shear plane angle (ϕ) [28]:

$$\tan\phi = \frac{r\cos\alpha}{1 - r\sin\alpha} \tag{3.2}$$

3.2.2 Forces in Orthogonal Cutting

Several forces can be defined using the orthogonal cutting model, which then lead to the establishment of equations that allow the calculation of several parameters such as: shear stress, friction coefficient, and others [28]. The forces analyzed through the orthogonal cutting model are defined based on Merchant's thin shear model, which assumes the following assumptions [30]:

1. The tool is perfectly sharp and has no contact along the clearance face;
2. The surface, where shear occurs is defined by a plane;
3. The cutting edge is a straight line extending perpendicular to the direction of motion, and generates a plane surface as the workpiece moves past it;
4. The chip does not flow to either sides;
5. Uncut chip thickness is constant;
6. Width of the tool is greater than the width of the workpiece;
7. A continuous chip is produced without any Built-up Edge (BUE);
8. Workpiece moves with a uniform velocity;
9. The stresses on the shear plane are uniformly distributed.

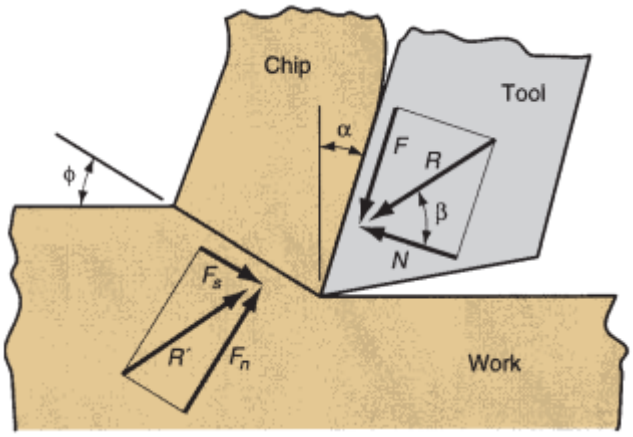

Figure 3.5: Forces acting on the chip in orthogonal cutting [28].

Given the tool-chip interaction (Figure 3.5), two perpendicular force components appear: friction force ($\overrightarrow{F}$) and normal force to friction ($\overrightarrow{N}$), and can be added vectorially to form a resultant force ($\overrightarrow{R}$). These two forces are used to define the coefficient of friction between the tool and the formed chip:

$$\mu = \frac{F}{N} \tag{3.3}$$

The resultant force $\overrightarrow{R}$ is oriented at an angle β, designated friction angle, as can be seen in Figure 3.5, and its relationship with the coefficient of friction is as follows:

$$\mu = \tan\beta \tag{3.4}$$

In addition to the tool forces acting on the chip, two more force components applied by the workpiece on the chip need to be considered and are denominated **shear force** $\overrightarrow{F_s}$, which is the force responsible for the shear deformation on the shear plane and its perpendicular component is defined as **normal force to shear** $\overrightarrow{F_n}$. According to shear force definition, shear stress that acts along the shear plane between the workpiece and the chip:

$$\tau = \frac{F_s}{A_s} \tag{3.5}$$

where A_s is defined as **area of the shear plane** and can be calculated as:

$$A_s = \frac{t_o w}{\sin\phi} \tag{3.6}$$

where t_0 is the uncut chip thickness and w the width of cut. Vectorial summation of the workpiece force components $\overrightarrow{F_s}$ and $\overrightarrow{F_n}$ results in a resultant force $\overrightarrow{R'}$ which, in order to balance the tool forces acting on the chip needs to be equal in magnitude, symmetric (opposite in direction) and collinear with the resultant force $\overrightarrow{R}$.

None of the forces mentioned above ($\overrightarrow{N}$, $\overrightarrow{F}$, $\overrightarrow{F_s}$, $\overrightarrow{F_n}$) can be measured directly during the machining operation because the direction of its applications vary with the cutting parameters and the tool geometry, therefore there's a need to decompose these forces in normalised directions (Figure 3.6) in order to be accurately measured with a dynamometer. These forces, as mentioned before are labelled cutting force $\overrightarrow{F_c}$ and thrust force $\overrightarrow{F_t}$ and form a resultant force labelled $\overrightarrow{R''}$. These force directions are normalized and can be accurately measured with the dynamometer [28].

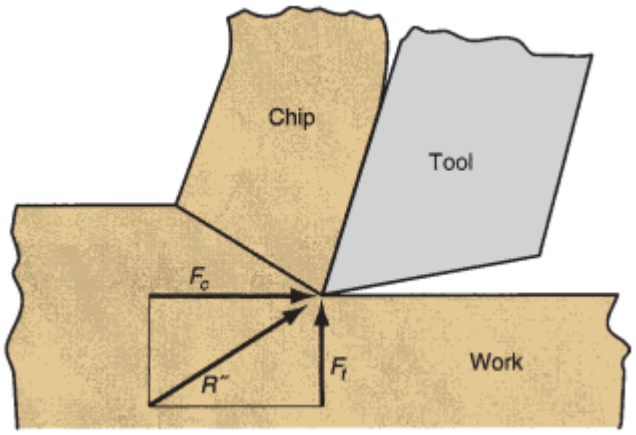

Figure 3.6: Forces normalized in the direction that can be measured [28].

In order to analyze the forces acting on the chip, geometrical relations need to be established to convert the forces measured in the dynamometer into the real forces acting on the chip. Using the geometrical relations shown in Figure 3.7, the following trigonometrical relations can be established:

$$F = F_c \sin\alpha + F_t \cos\alpha \tag{3.7}$$

$$N = F_c \cos\alpha - F_t \sin\alpha \tag{3.8}$$

$$F_s = F_c \cos\phi - F_t \sin\phi \tag{3.9}$$

$$F_n = F_c \sin\phi + F_t \cos\phi \tag{3.10}$$

If cutting and thrust forces are known (experimentally obtained) the four equations can be used to calculate friction force (3.7), normal force to friction (3.8) shear force (3.9) and normal force to friction (3.10). Based on these forces, the coefficient of friction and shear stress can be calculated.

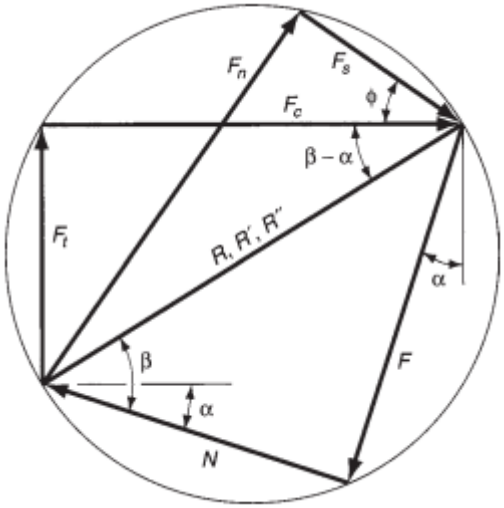

Figure 3.7: Forces diagram showing geometric relations between N, F, F_s, F_n, F_c and F_t [28].

3.3 Chip Formation in Metal Cutting

Merchant's model of orthogonal cutting mechanics has some limitations when applied to a three-dimensional machining process, therefore some key differences need to be considered when analyzing a real machining process. Firstly, shear deformation process does not occur along a plane, but within a thin shear zone called primary shear zone, this represents a more realistic model of what happens during shear formation and is illustrated in Figure 3.8. Secondly, in addition to shear deformation that occurs in the primary shear zone, another shearing action occurs in the chip after being deformed, referred to as secondary shear zone and results from friction between the chip and the tool as the chip slides along the rake face of the tool [28].

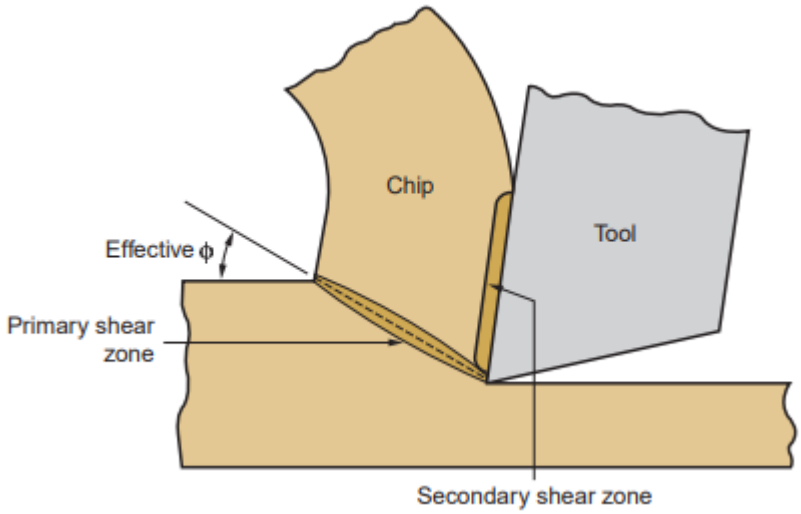

Figure 3.8: Orthogonal cutting scheme showing primary and secondary shear zones [28].

Four main types of chip geometries can occur, see Figure 3.9, regarding different materials and parameters [28]:

- **Discontinuous chip** - When using brittle materials at low cutting speeds, large feeds and depths of cut, or when high tool-chip friction occurs, the chip tends to form into separate segments and can be loosely attached. The main consequence of this chip formation mechanism is the irregular machined surface;

- **Continuous chip** - Occurs when using ductile materials at high cutting speeds, small feeds and depths of cut. Low chip-tool friction and sharp cutting edge tends to promote this chip formation mechanism. A good surface finish is obtained when these type of chips are formed, although, long continuous chips can become an issue in terms of chip disposal and/or tangling on the tool, in order to prevent this, some tools are equipped with chip breakers;

- **Continuous chip with built-up edge (BUE)** - This type of chips form when machining ductile materials at low to medium cutting speeds. Some portions of the work material adhere to the rake face of the tool near the cutting edge and can have detrimental consequences in overall tool life and surface quality of the workpiece;

- **Serrated chips** - Semi-continuous chips that have a saw-tooth like appearance that forms due to a cyclical high shear strain deformation followed by a low shear strain deformation. This type of chip formation is mostly associated with materials that are difficult to machine, for example titanium. However, this type of chip can also be found when machining common alloys (e.g. steels) when high cutting speeds are used.

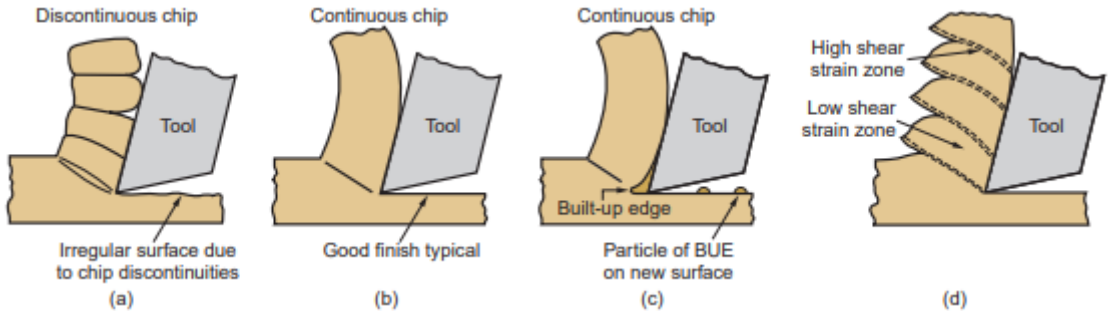

Figure 3.9: Types of chip formation mechanisms: (a) discontinuous, (b) continuous, (c) continuous with BUE, (d) serrated [28].

3.3.1 Chip Morphology

In accordance with the chip formation mechanism, workpiece material and machining parameters, different types of chip geometries can be obtained. These geometries are sub-divided and categorized into eight different groups, according to their shape and size. These categories are defined by the ISO 3685 standard and are illustrated in Figure 3.10. The different chip geometries can be categorized according to its advantages/disadvantages in terms of operator safety, workpiece quality, cutting tool life, the most hazardous types of chips are ribbon chips, snarled chips, flat helical chips and long cylindrical helical chips, which can be very detrimental to the safety of the operator and/or machine.

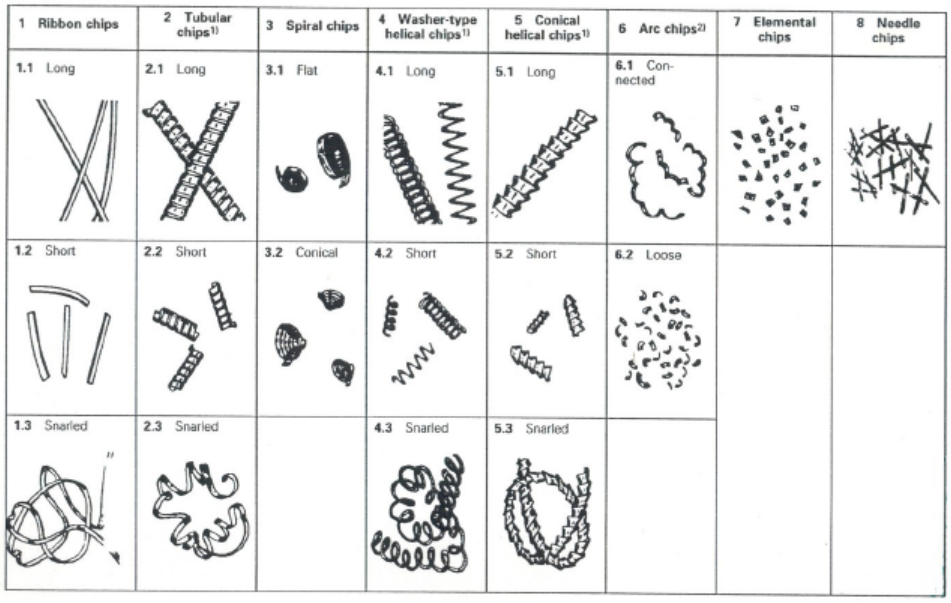

Figure 3.10: Chip form classification according to ISO 3685 standard [33].

3.4 Machinability

Machinability is usually defined as the ease a certain material is machined. Because of the many parameters that determine a successful metal cutting operation, it is a challenging property to evaluate. Some of the most common aspects that strongly influence a material's machinability are [30]:

- Workpiece material properties;
- Cutting forces;
- Tool geometry;
- Tool life;
- Machining parameters;

- Lubrication;
- Chip form.

Overall machinability of a certain type of material can be correlated to the tool life due to the fact that harder to machine materials tend to reduce tool life significantly. Tool life can be an important machinability indicator correlating with the resultant machining forces acting on the tool, which increase the harder it is to machine a certain material.

Process parameters and tool geometry also have a crucial influence in the cutting forces involved which in turn relate to machinability since they can lead to a reduction in tool life if improperly chosen. Figures 3.11 and 3.12 illustrate the influence of different process parameters and tool geometry on the resultant forces involved in the machining process and tool life, respectively.

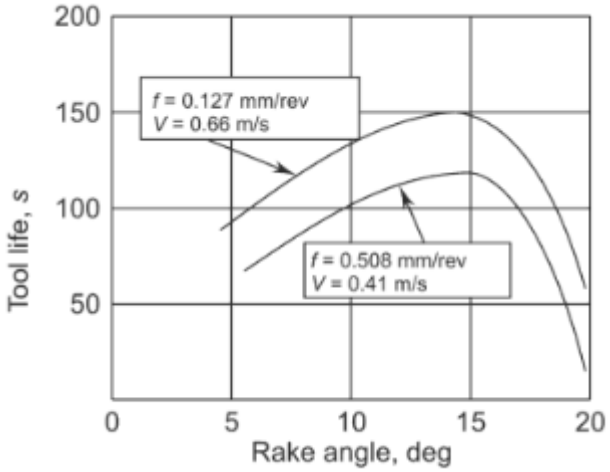

Figure 3.11: Tool life affected by rake angle and feed rate [30].

Hardness properties alone are not enough to quantify properly the machinability of a certain material. Physical microstructure has also a great impact in terms of machinability. For example, steels that contain free ferrite are relatively soft materials and their machining has almost no tool wear, however they are likely to form a chip with built-up edge, resulting in a poor surface finish. Presence of cementite for example, due to its hardness tends to reduce tool life, contrarily to cast irons, containing free graphite which is a softer phase and result in a better tool life and, consequently, in a better machinability [30].

3.5 Cutting Tools

3.5.1 Tool Materials

Tool materials must endure the rough conditions during the metal cutting operations, therefore must comply with certain requisites in order to achieve a good performance during the process.

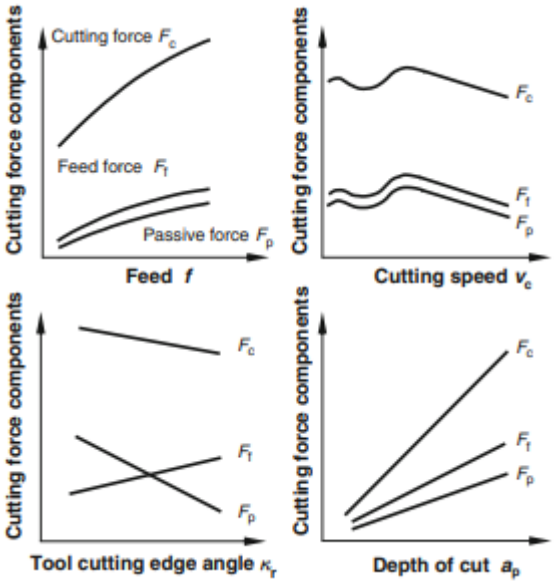

Figure 3.12: Components of resultant force depending on feed, cutting speed, tool cutting edge angle, and depth of cut (qualitative) [34].

A certain tool material must be though to prevent wear and consequent failure. The tool material must be able to maintain its mechanical properties at a high temperature. Because of the extreme conditions the tool is withstanding during a certain operation, it needs to be able to keep its integrity.

Another important property tool materials must have in order to improve its life-cycle is good wear resistance. Wear resistance is related to material hardness which in turn, relates to abrasion resistance. A good surface finish on the tool results in a lower coefficient of friction, reducing tool wear. Also, in order to resist tool wear, the presence of a cutting fluid is important because it can reduce the friction between the tool and the workpiece resulting in a better tool life [29].

Cutting tool materials must have a combination of these properties and the selected material must be chosen accordingly depending on the machining operation, workpiece material and cutting parameters. The main categories of cutting tool materials are [29]:

- High-speed steels (HSS) and its predecessors (plain carbon and low alloy steels);
- Cast cobalt alloys;
- Cemented carbides, cermets, and coated carbides;
- Ceramics;
- Synthetic policristaline (PCD) diamond and cubic boron nitride (cBN);

Commercially, the most used cutting tool materials are high-speed steels, cemented carbides, cermets and coated carbides and account for more than 90% of the cutting tools used in machining

operations [29]. Some mechanical properties and cutting speeds of most commonly used tools are illustrated in Tables 3.1 and 3.2, respectively.

Table 3.1: Typical hardness values (at room temperature) and transverse rupture strengths for various tool materials [29].

		Transverse Rupture Strength	
Material	**Hardness**	**MPa**	**lb/in²**
Plain carbon steel	60 HRC	5200	750,000
High-speed steel	65 HRC	4100	600,000
Cast cobalt alloy	65 HRC	2250	325,000
Cemented carbide (WC)			
Low Co content	93 HRA, 1800 HK	1400	200,000
High Co content	90 HRA, 1700 HK	2400	350,000
Cermet (TiC)	2400 HK	1700	250,000
Alumina (Al_2O_3)	2100 HK	400	60,000
Cubic boron nitride	5000 HK	700	100,000
Polycrystalline diamond	6000 HK	1000	150,000
Natural diamond	8000 HK	1500	215,000

Table 3.2: Cutting tool materials with their approximate dates of initial use and allowable cutting speeds [29].

		Allowable Cutting Speed[a]			
		Nonsteel Cutting		Steel Cutting	
Tool Material	**Year of Initial Use**	**m/min**	**ft/min**	**m/min**	**ft/min**
Plain carbon tool steel	1800s	Below 10	Below 30	Below 5	Below 15
High-speed steel	1900	25–65	75–200	17–33	50–100
Cast cobalt alloys	1915	50–200	150–600	33–100	100–300
Cemented carbides (WC)	1930	330–650	1000–2000	100–300	300–900
Cermets (TiC)	1950s			165–400	500–1200
Ceramics (Al_2O_3)	1955			330–650	1000–2000
Synthetic diamonds	1954, 1973	390–1300	1200–4000		
Cubic boron nitride	1969			500–800	1500–2500
Coated carbides	1970			165–400	500–1200

3.5.2 Tool Geometry

Another important aspect when classifying different cutting tools other than its material, is its geometry. Different types of tool geometries are used depending on the machining process. Cutting tools are divided into two major categories, single-point tools and multiple-cutting-edge tools. Single-point tools are used, for example, in turning operations whereas multiple-cutting-edge tools are used for instance in milling operations.

Typically, when using a single point tool, instead of using a single solid tool, the cutting edge consists of an insert which allows for a more economically viable solution given the fact that is the part of the tool subject to more wear, if an insert is used it is cheaper to replace than the whole tool. Typically, inserts are not usually made with a perfectly sharp cutting edge, given the fact that sharp edges are weaker and more prone to fracture, especially considering the brittle and hard materials inserts are made from (cemented carbides, cermets, ceramics, coated carbides, cBN and PCD). Figure 3.13 shows different types of single-point cutting tools, with and without the use of inserts.

Figure 3.14 shows the different geometrical parameters that exist in a single-point cutting tool.

The rake angle plays an important role in most machining operations, and is directly related to chip disposal, cutting temperature, tool life and cutting resistance, and can be either positive or negative depending on the application. Positive rake angles are mostly used when machining soft materials, materials with good machinability or when the workpiece/machine have poor rigidity, whereas a negative rake angle is used when machining hard workpieces or when increased cutting edge strength is required (e.g. uncut surfaces and/or interrupted cutting) [35]. Positive (+) and negative (-) cutting angles are illustrated in Figure 3.15.

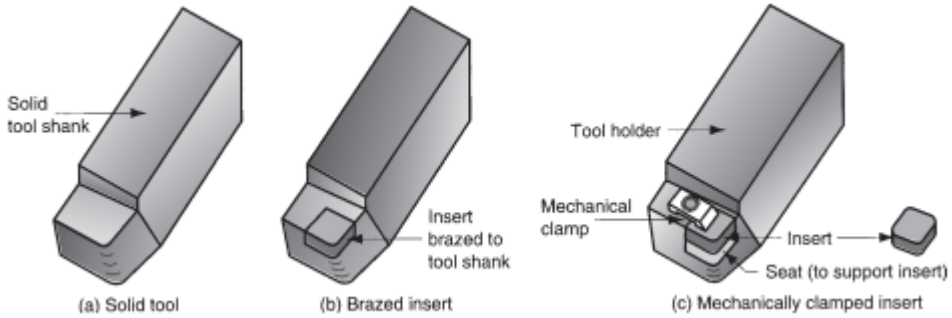

Figure 3.13: Three ways of holding and presenting the cutting edge for a single-point tool: (a) solid tool, typical of HSS; (b) brazed insert, one way of holding a cemented carbide insert; and (c) mechanically clamped insert, used for cemented carbides, ceramics, and other very hard tool materials [29].

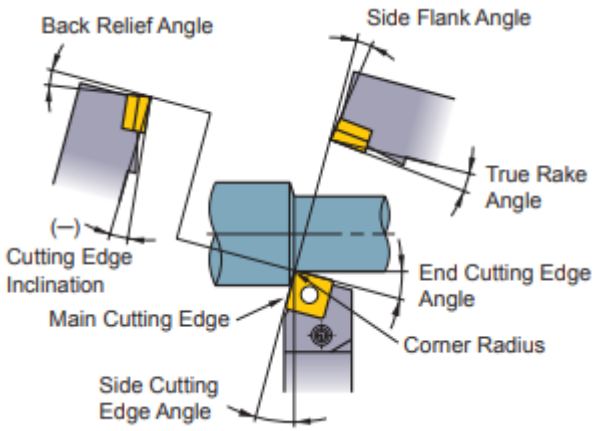

Figure 3.14: Typical single-point tool geometry [35].

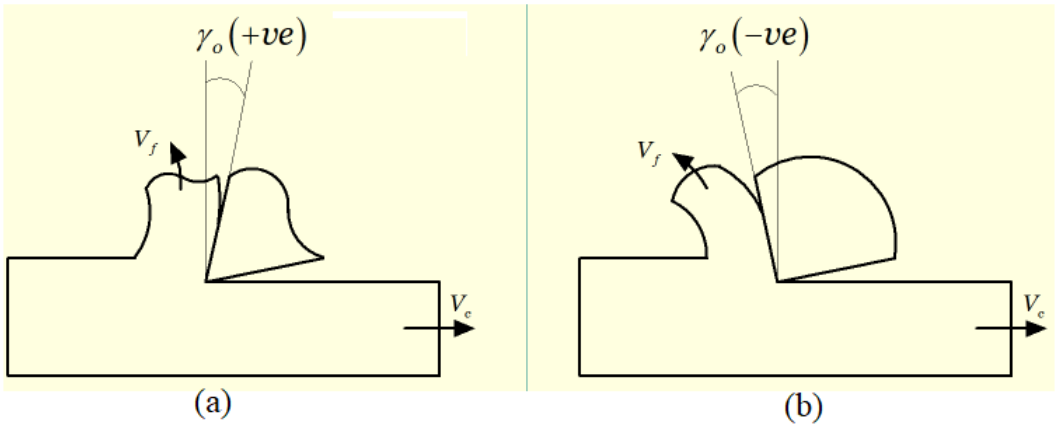

Figure 3.15: Positive (+) and negative (-) rake angles [36].

Flank angle is responsible for the reduction of friction between the flank face and the workpiece, resulting in a smoother feed. Increasing this angle leads to a reduction in tool wear in the flank zone, however it lowers cutting edge strength. Flank angle is increased when machining soft materials and when the workpiece material suffers from strain hardening, and is decreased when machining hard workpieces and when an increased cutting edge strength is required [35].

Side cutting edge angle, refer to Figure 3.14 (also known as lead angle) is responsible for reducing the impact load and affects the chip thickness. Its increase, decreases chip thickness while at the same time increasing the chip contact length, resulting in a dispersion of the cutting force on a longer cutting edge, thus increasing tool life. Increasing the side cutting edge angle can also increase the radial force the tool exerts in the workpiece which can cause bending if a thin/long workpiece is being machined.

The end cutting edge angle, refer to Figure 3.14, avoids unwanted interference between the machined surface and the tool (end cutting edge), usually has values between 5-15°. Decreasing the end cutting edge increases the cutting edge strength, yet it results in an increase in the cutting

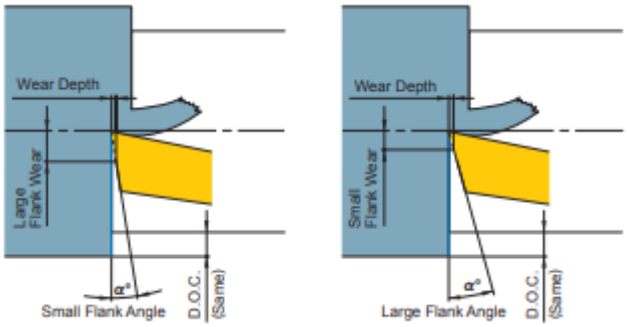

Figure 3.16: Small and large flank angle [35].

edge temperature and can induce vibration in the system. Small end cutting edge angle is used for roughing, whereas large end cutting edge angle is used for finishing operations [35].

3.6 Turning

Turning is a machining process in which a single-point tool removes material from a rotating workpiece. In cylindrical turning, the cutting tool is fed linearly in a direction parallel to the axis of rotation to generate a cylindrical geometry. Turning is usually carried out in a machine called a lathe, which provides the power to rotate the workpiece at a certain rotational speed and feeds the cutting tool at a specific rate and depth of cut.

The orthogonal model can be used as an adequate approximation to the turning process, as long as the feed is small relatively to the depth of cut, which makes most of the cutting action taking place in the feed direction and the cutting on the tip of the tool is negligible. The orthogonal cutting parameters can be converted to the turning parameters and vice-versa (Table 3.3).

Table 3.3: Conversion between orthogonal cutting and turning parameters [29].

Turning Operation	**Orthogonal Cutting Model**
Feed f =	Chip thickness before cut t_o
Depth d =	Width of cut w
Cutting speed v =	Cutting speed v
Cutting force F_c =	Cutting force F_c
Feed force F_f =	Thrust force F_t

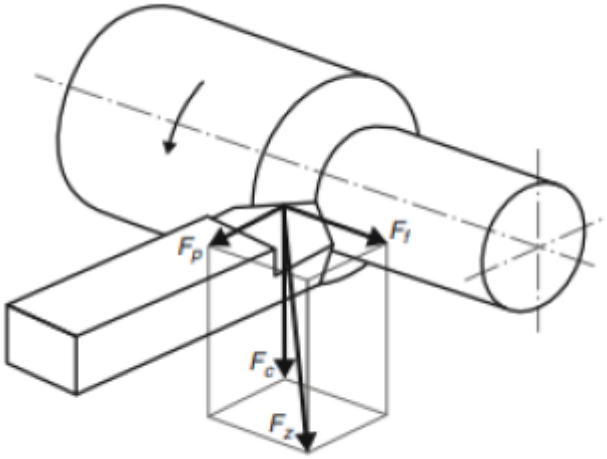

Figure 3.17: Geometry of the turning process [37].

When analyzing forces in a turning process, three components need to be analyzed: feed force F_f, tangential or cutting force F_c and radial or penetration force F_p. Cutting power P_c (kW) is the power the lathe machine needs to have in order to perform a certain operation. It can be calculated using its relation to the cutting parameters, using the following equation:

$$P_c = \frac{a_p \cdot f \cdot v_c \cdot K_c}{60 \times 10^3 \times \eta} (kW) \tag{3.11}$$

where a_p is the depth of cut (mm), f the feed per revolution (mm/rev), v_c the cutting speed (m/min), K_c the specific cutting pressure (MPa) and η is the machine efficiency. The cutting speed (m/min) relates to the rotational spindle speed as:

$$v_c = \frac{\pi \cdot D_m \cdot n}{1000} (m/min) \tag{3.12}$$

D_m stands for the workpiece diameter (mm) and n the rotational spindle speed (rpm). The spindle speed n relates to the feed rate f through the following expression:

$$f = \frac{l}{n} (mm/rev) \tag{3.13}$$

where l represents the cutting length per minute and n the rotational speed of the spindle.

Machining is often the process that determines the final dimensions and finishing quality of a determined part, therefore surface quality plays an important role in machining. Overall surface texture (roughness) is directly related to geometrical factors, workpiece material factors and vibration/machine tool factors. Surface roughness is quantified as an average of the deviations in the normal direction of a certain surface from its ideal form.

For turning operations geometric factors such as nose radius (r_e) and feed (f) can be related to the theoretical arithmetic average of surface roughness (R_{ta}) and the maximum roughness (R_{tmax})

using the following equations (see Figure 3.18):

$$R_{ta} = \frac{f^2}{32 r_e} \tag{3.14}$$

$$R_{tmax} = \frac{f^2}{8 r_e} \tag{3.15}$$

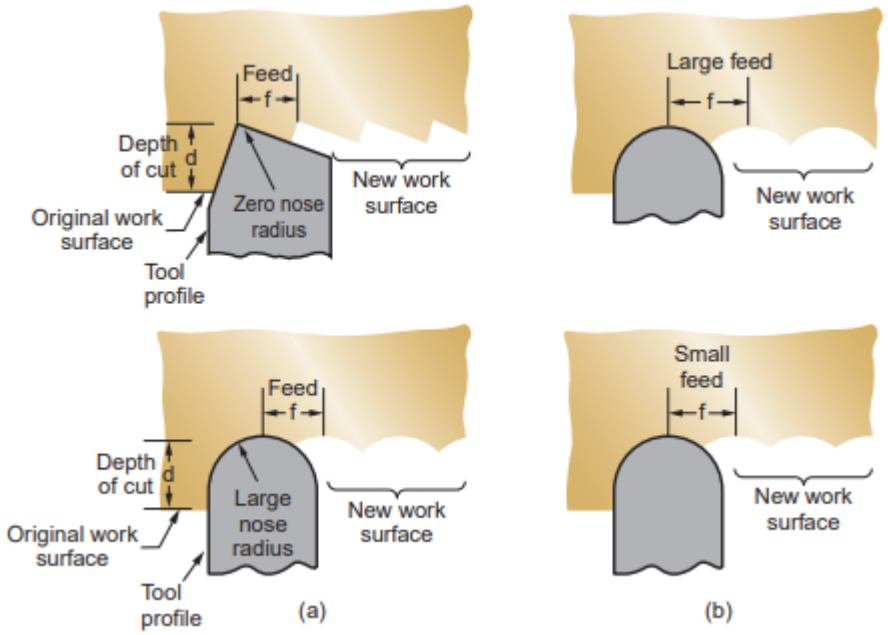

Figure 3.18: Effect of geometric factors in determining the theoretical finish on a work surface for single-point tools: (a) effect of nose radius, (b) effect of feed [29].

3.7 Milling

Milling is a machining operation in which a work part is fed past a rotating cylindrical tool with multiple cutting edges. The axis of rotation of the cutting tool is perpendicular to the feed direction and to the surface being milled. There are two basic types of milling operations, peripheral milling and face milling. Face milling will be the focus on this dissertation since the experimental work will only be on this type of operation. The typical geometry of a face milling operations is illustrated in Figure 3.19 [29].

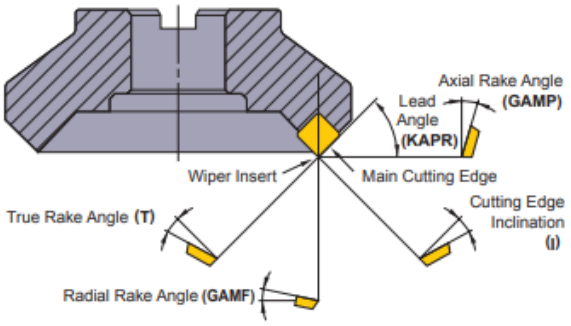

Figure 3.19: Face milling geometry [35].

Axial Rake Angle determines the chip disposal direction, if positive machinability is increased. The Radial Rake Angle determines sharpness and chip disposal is enhanced, if negative. Lead angle is responsible for the chip thickness and if it is small, it leads to thin chips and small cutting impact, however it increases back force, refer to Figure 3.21. Different lead angles and the effects produced in the cutting operations can be seen in Figure 3.20.

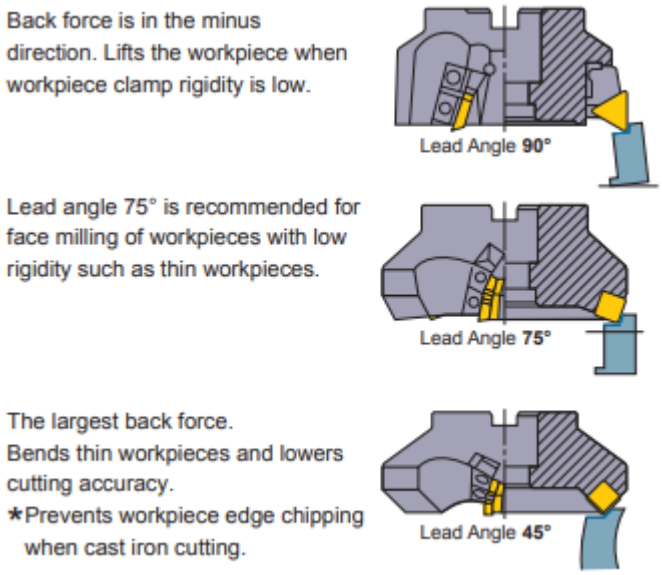

Figure 3.20: Different lead angle values (90º,75º and 45º) and its effects on the cutting performance [35].

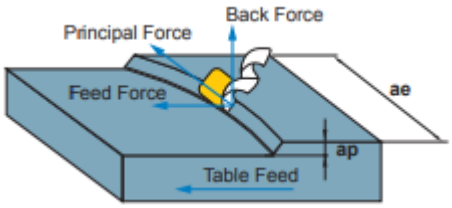

Figure 3.21: Cutting forces in milling operation [35].

The true rake angle if positive, improves machinability but leads to micro-welding in the cutting area, if negative leads to poor machinability but increases the strength of the cutting edge [35]. The cutting edge inclination, as well as the aforementioned axial rake angle determines the chip disposal direction and if it is positive and large improves chip disposal considerably but decreases cutting edge strength. In face milling, there's also the need to choose a machining strategy, which consists of up cutting or down cut milling (also known as climb milling), which is the direction in which the workpiece moves related to the tool rotation. Up cutting or down cutting depends on the conditions of the machine tool, the milling cutter (cutting tool) and the application, however in terms of tool life, down cut milling can be more advantageous [35].

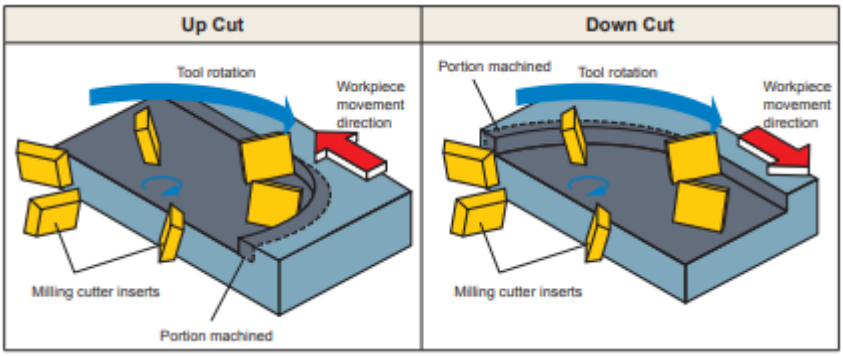

Figure 3.22: Up cut and down cut milling [35].

The cutting power in face milling P_c (kW) can be related to several important parameters using the expression:

$$P_c = \frac{a_p \cdot a_e \cdot v_f \cdot K_c}{60 \times 10^6 \times \eta} \ (kW) \tag{3.16}$$

where a_p is the depth of cut (mm), a_e is the cutting width (mm) (Figure 3.21), v_f represents the table feed per minute (mm/min), K_c the specific cutting force and η the machine efficiency coefficient.

The cutting speed v_c (m/min) relates to the cutter diameter Dc (mm) (Figure 3.23) and the main axis spindle speed n (rpm) through the equation:

$$v_c = \frac{\pi \cdot Dc \cdot n}{1000} \ (m/min) \tag{3.17}$$

Another important parameter in face milling is the feed per tooth f_z (mm/tooth):

$$f_z = \frac{v_f}{z \cdot n} \ (mm/tooth) \tag{3.18}$$

with v_f being the table feed per minute (mm/min), z the number of inserts (teeth) and n the main axis spindle speed.

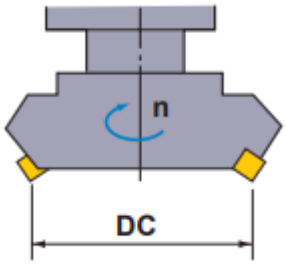

Figure 3.23: Cutter diameter schematic [35].

Table feed v_f (mm/min) is defined as a function of the feed per tooth f_z (mm/tooth), z the number of inserts and n the main axis spindle speed (rpm), as can be seen in the Equation (3.19).

$$v_f = f_z \cdot z \cdot n \ (mm/min) \tag{3.19}$$

Also the cutting time Tc (min) of a determined milling operation is related to the total table feed length L (workpiece length l + cutter diameter Dc) (Figure 3.24) with the table feed per minute v_f as:

$$Tc = \frac{L}{v_f} \ (min) \tag{3.20}$$

Figure 3.24: Total table feed length schematic [35].

In milling operations, the relevant force components (refer to Figure 3.25) are cutting force (F_c), co-linear with the instantaneous cutting speed (v_c), and a radial component, which is the normal force to the cutting speed (F_{cN}). The normalized force components are a function of the entry angle φ (note Figure 3.25). For simplification purposes, these forces can be decomposed into F_x and F_y, with the fixed direction, through the following trigonometric relations [38]:

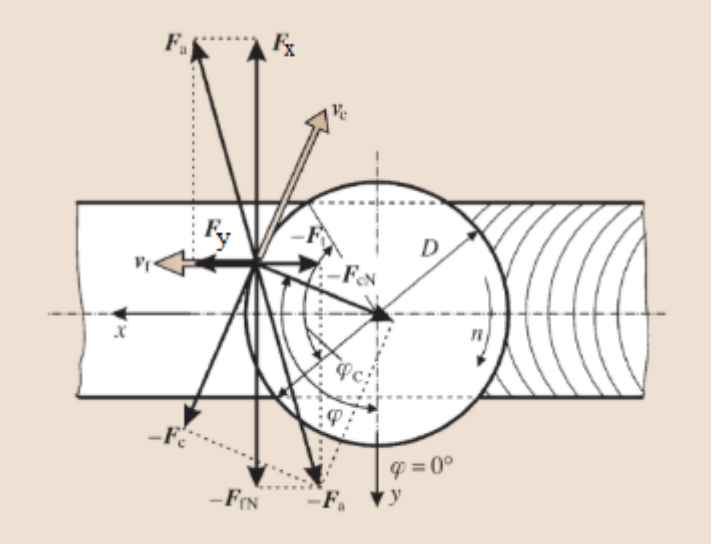

Figure 3.25: Components of cutting force in plain face milling [38].

$$F_c = F_x \sin\varphi + F_y \cos\varphi \tag{3.21}$$

$$F_{cN} = F_x \cos\varphi + F_y \cos\varphi \tag{3.22}$$

Another important aspect to be considering regarding the milling mechanics is that during the cutting operation, the chip section is not constant and is a function of several parameters. Figure 3.26 illustrates the undeformed chip cross-section variability as a function of the entry angle (φ).

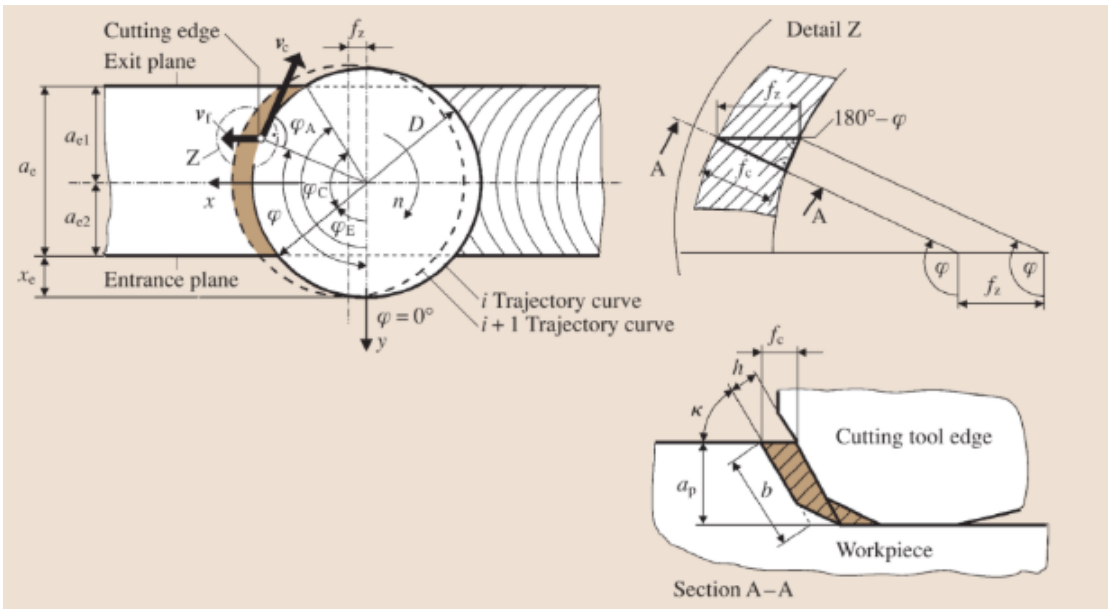

Figure 3.26: Tool-workpiece engagement variables in plain face milling [38]

The undeformed chip cross-section is a function of the undeformed chip width b and the undeformed chip thickness $h(\varphi)$ (Figure 3.26) and is calculated through the following equation:

$$A(\varphi) = bh(\varphi) = a_p f_z \sin\varphi \tag{3.23}$$

Where the undeformed chip width b is calculated as a function of the depth of cut (a_p) and the cutting tool edge inclination angle (k).

$$b = \frac{a_p}{\sin k} \tag{3.24}$$

The undeformed chip thickness on the other hand is a function of the feed per tooth (f_z), the cutting tool edge inclination angle (k) and the entry angle (φ):

$$h = f_z \sin k \sin\varphi \tag{3.25}$$

From equation (3.23) it can be concluded that the point where the undeformed chip cross-section is the highest is exactly when the φ= 90º and it is equal to the feed per tooth (f_z) multiplied by the depth of cut (a_p). This approach simplifies the resolution of the problem, however it does not take into account that the chip area depends on the continuous feed rate; instead this method takes into account two homologous tool positions and calculates the chip cross-section variable with both positions.

3.8 Machinability of AM Materials

Despite offering increased possibilities when it comes to geometrical complexity, the surfaces of additively manufactured metals generally present high surface roughness, which can be incompatible with the components' purpose. Metal cutting operations are often employed in order to overcome such issue.

Fortunato [39] studied the influence of different heat treatments and face milling of a determined maraging steel part (18Ni300) fabricated by a SLM technology and concluded that parts that were subjected to partially heat treatments (solutionizing heat treatment at 815ºC for 1 h followed by air cooling) resulted in the minimum tool wear, whereas samples that weren't subjected to an heat treatment had the worst behaviour in terms of tool wear. Regarding cutting forces, the maximum values were obtained in the non-treated samples and the minimum value for the totally heat-treated (TT) samples (subjected to solutionizing plus ageing heat treatment at 480ºC for 4 h followed by air cooling). Fortunato [39] also concluded that an increase of the cutting speed in the heat-treated samples leads to a decrease in the cutting forces and respectively tool wear, and related it to the occurrence of thermal softening associated with the heat treatment used. This thermal softening is possible because for a heat treatment with ageing, martensite softening occurs above 200ºC, whereas in a sample that is not treated thermically, the microstructural transformation starts above the austenite transformation of 800ºC which explains the increase of cutting

forces with the increase of cutting speed, due to the fact that during cutting, no microstructural transformation takes place and thermal softening is not sufficient to compensate for tool wear.

It was also concluded that increasing the cutting speed also improves the surface roughness of the samples in both partially treated and totally heat-treated samples.

In another study carried out by Milton [40] the milling of different Ti6Al4V SLM samples was compared with the conventionally fabricated titanium alloy. Higher axial loads were verified for the SLMed samples, which may be related with the columnar grain formation (higher density of grain discontinuities) typical of MAM. The measured higher loads lead to lower tool life and higher residual stress when comparing SLM samples with conventional ones.

Polishetty [41] arrived to the same conclusions regarding the increase in the cutting forces during machining of SLM Ti6Al4V when compared to conventionally produced Ti6Al4V. It was also concluded that with the increase of the cutting speed for an SLM sample without heat treatment the cutting forces increase, whereas in a conventional sample decrease with the increase in cutting speed. Surface roughness was also analyzed and was lower in the SLM samples when related to conventionally produced ones, and could be likely linked to the high hardness and brittle nature of SLM Ti6Al4V. The study of cutting speed influence in the surface roughness was also analyzed and it was concluded that surface roughness decreases with an increase in cutting speeds due to the reduction of build-up edge formation and the effect of thermal softening at high cutting speeds that reduces the adhered materials on the tool rake face. However with the increase of the feed rate surface roughness increased in both SLM and conventional samples and could be linked to machine tool vibrations and thermal softening.

Chapter 4

Material Characterization and Experimental Procedure

4.1 Introduction

The main goal of this dissertation is to evaluate the machinability of 18Ni300 maraging steel. AM offers great freedom in terms of design and part complexity, however surface quality does not comply with the demanding industrial requirements of tight dimensional tolerances, so most metal additive manufacturing processes need some sort of post processing operations, for example machining. The goal of this experimental procedure is to evaluate maraging steel machinability since this is an important material in the metallic AM processes. Due to its excellent mechanical properties it is widely used throughout several industries, being one of the main applications the production of inserts for plastic injection moulds, that with the AM's capability of geometrical complexity, it allows solutions that otherwise would not be possible using conventional manufacturing processes (e.g. conformal cooling channels).

Metallographic and microstructural analysis, chemical composition identification, defects and porosity observation and calculation as well as quasi-static compression tests of the AM machined samples were conducted within the material characterization stage.

Metal cutting tests (turning and milling) with load measurement were carried out in order to evaluate the material's machinability. Tool wear and chip morphology were inspected for some of the tested parameters. Important cutting parameters (such as cutting power and specific cutting pressure) were determined and the surface quality of the finished specimens was measured and analyzed.

4.2 Chemical Composition

The chemical composition must comply with the material's standard which is presented in Table 4.1. Chemical composition analysis was not performed for the conventional material in this experimental work, but as in order to establish a comparison between the AM and the conventional

material, chemical composition of the conventional material was obtained from Couto's thesis [42].

Table 4.1: Standard chemical composition of 18Ni300 maraging steel [43], conventional [42] and AM sample composition.

	Standard	**Conventional Sample**	**AM Sample**
Element		**wt %**	
Ni	17.00 to 19.00	18.93	17.62
Co	7.00 to 10.00	8.92	9.36
Mo	4.50 to 5.20	4.88	5.18
Ti	0.30 to 1.20	0.77	0.70
Si	≤ 0.10	0.02	0.08
Mn	≤ 0.15	0.03	0.06
C	≤ 0.03	0.01	0.02
P	≤ 0.01	≈ 0.00	≤ 0.0005
S	≤ 0.01	≈ 0.00	0.005

The chemical composition of the samples was measured by spectrophotometry (SPECTROMAX metal analyzer) and the results were compliant with the nominal compositions presented in the standard. The composition values can be seen in Table 4.1. These values are within the admissible standard limits established. The conventional and AM material present similar chemical compositions.

4.3 Microstructure and Defects

Samples in an as-built state were prepared in order to perform metallographic analysis. These samples were cut in a disc saw machine in order to analyze different material directions (transverse to build and parallel to build diretions). Samples were mounted on thermoset resin, and the same polishing technique was performed in all in order to keep the results coherent. The microscopical analysis of these samples was carried out using a OLYMPUS PMG3 optical microscope (refer to Figure 4.1).

4.3.1 Porosity

Porosity is a very common defect in AM processes, and it is a key indicator of the process performance. Therefore its analysis is crucial to understand the quality of the as built samples. Optical microscopy images were taken and subsequently subjected to analysis, which was carried out using an image analysis software (ImageJ) where the images are converted into a binary color form (Figure 4.2) and the area fraction that does not have material is calculated. It is also important to note that this analysis is the most representative for the higher amount of images analyzed, covering the whole sample area. Accumulated porosity can remain unaccounted if the whole sample is not considered. Additionally this technique takes into account the actual porosity geometry, regardless of its irregularity.

Figure 4.1: Optical microscope OLYMPUS PMG3.

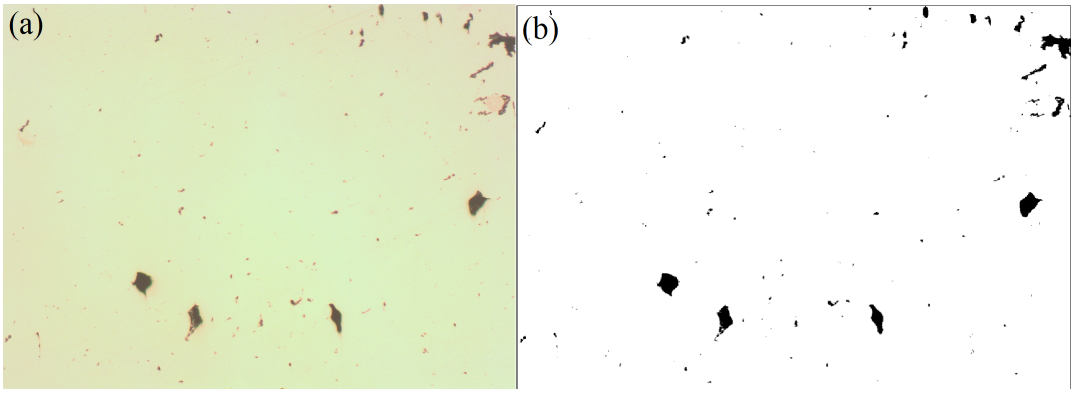

Figure 4.2: Image treatment for porosity analysis in the transverse to build direction: (a) original optical image, (b) binary image for porosity calculation.

It is important to note that two different directions were analyzed through optical microscopy, both for porosity and microstructural analysis. Building direction is defined by the Z axis (parallel to build direction); two different directions parallel to build direction were considered, namely XZ or YZ plane and transverse to build direction (XY plane), a schematic illustration can be seen in Figure 4.3.

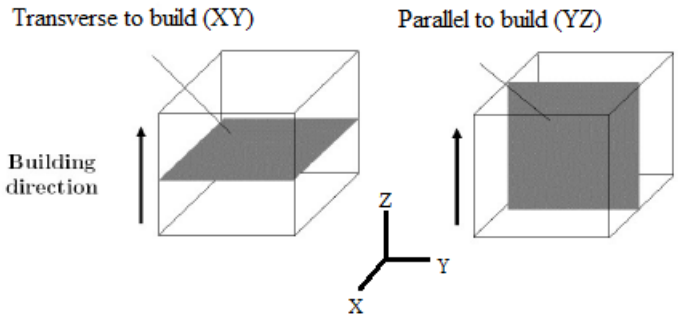

Figure 4.3: Schematics of different building directions (transverse and parallel to building directions), adapted from [42].

A sample taken from the building plate was split in half along the building direction using a disc saw, and one of the halves was set aside to analyze the whole parallel to build plane, whereas the other half was cut into three pieces along transverse to build direction planes in order to analyze the influence of the building height in the relative density of the samples. Each surface was labelled and subjected to optical microscopy observations. A schematic image of the samples labelling is illustrated in Figure 4.4. Surfaces labelled as A are the surfaces perpendicular to build direction (parallel to plane XY) and surface B corresponds to the surfaces parallel to build direction (parallel to plane ZY or ZX).

The results obtained were subjected to an arithmetic average of the several sections in a determined surface in order to achieve a better estimate of the relative density in each sample. Results can be seen in Table 4.2.

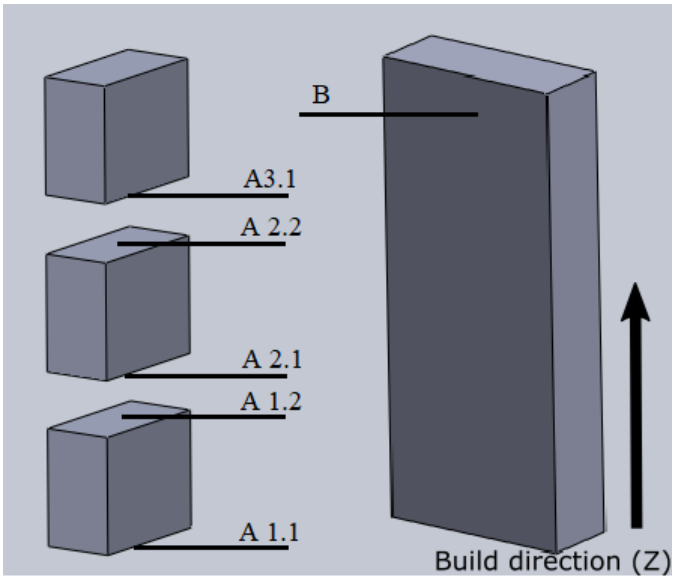

Figure 4.4: Schematic of the parallel and transverse to build surfaces analysed by optical microscopy.

The average porosity for the whole sample is around 0.95% which leads to a relative density

Table 4.2: Porosity results per surface analyzed.

Surface	A1.1	A1.2	A2.1	A2.2	A3.1	B
Porosity (%)	0.75	0.94	0.89	1.03	0.94	0.95

of 99.05%. Note that the surface with the least porosity is the bottom surface which is the surface attached to the building substrate, which can be related to the fact that this is one of the first layers being built, therefore there may be less defects related to the poor overlap of subsequent layers.

4.3.2 Microstructure

Eletrolytic etching is useful in AM materials since it allows to identify important microscopical aspects of a powder bed fusion process, such as melt pool boundaries and laser scan paths. Electrolytic etching of the polished samples was carried out using an eletrolysis cell where DC current is applied for a determined duration in order to reveal metallurgical characteristics. The eletrolytic etching was done in a Struers LECTROPOL-5 (Figure 4.5) which automatically determines the best etching parameters in order to prevent human error and time consumption since etching is a hardworking trial and error process.

Figure 4.5: Eletrolytic etching equipment (Struers LECTROPOL-5).

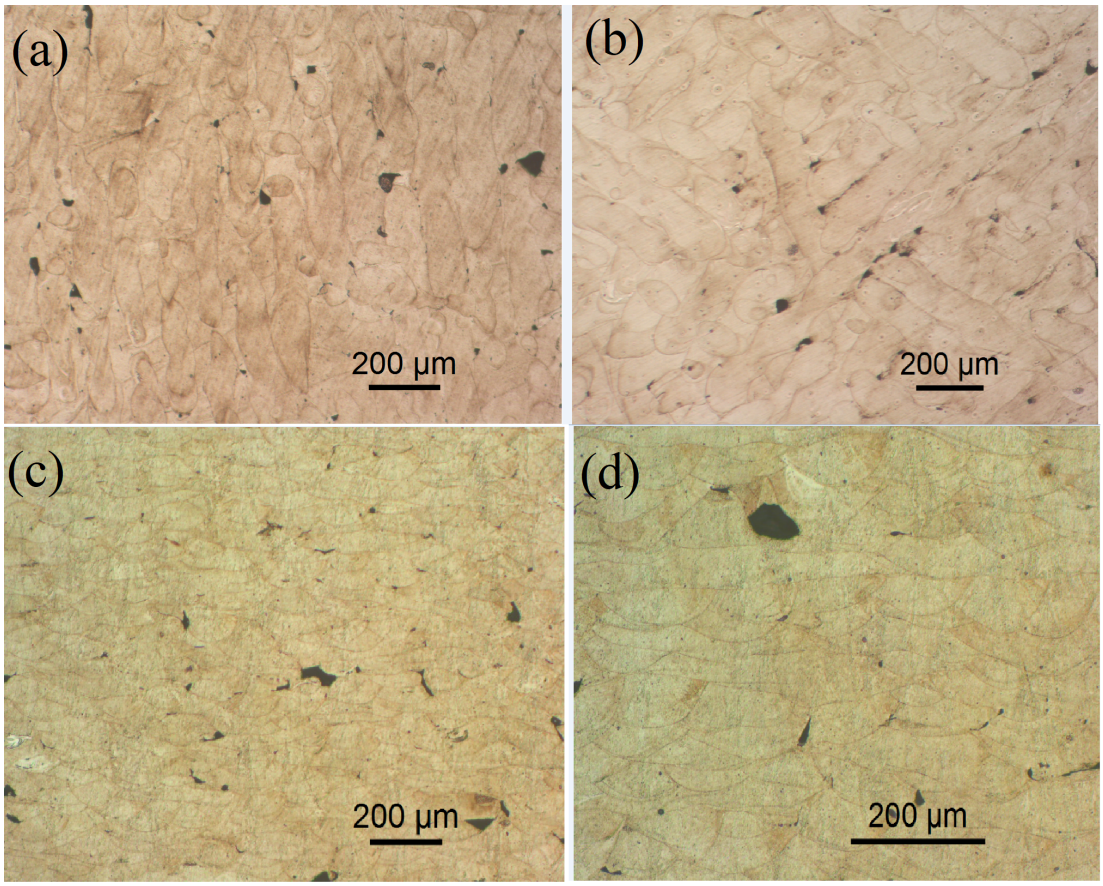

Figure 4.6: Optical images of eletrolitically etched surfaces: (a) and (b) transverse to build direction surfaces; (c) and (d) parallel to build direction surfaces.

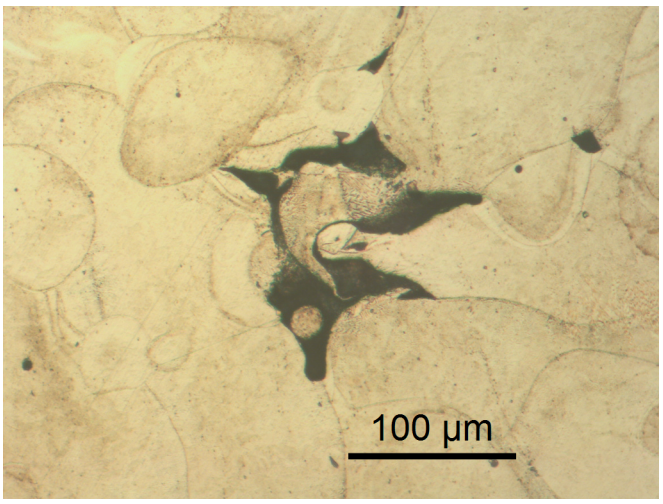

Figure 4.7: Optical image of lack-of-fusion defect with unmelted powder particles.

In Figure 4.6 (a) and (b) optical images of the transverse to build directions surfaces are depicted and it is possible to observe the multiple laser scan paths across the surface. The laser paths do not appear in an orderly orientation due to the challenging task of polishing the samples in

the exact perpendicular and parallel directions to the building reference. Therefore it is possible to observe multiple laser scan paths in this surface. The fact that chess scanning strategy (view Figure 2.3) was employed also hinders the visualisation of a linear laser path. Figure 4.6 (c) and (d) show a parallel surface to the building direction, and in these optical images it is possible to observe the overlap of the molten pools. Also, the half-elliptical shapes can be informative since its geometrical properties can be related to SLM process parameters, namely, the height of these half-ellipses are approximately equal to the powder layer thickness and the base widths are approximately equal to the laser spot diameter [44]. Also, in Figure 4.7 its possible to observe a typical lack-of-fusion defect with unmelted powder particles.

4.4 Surface Roughness

Another important parameter in AM manufactured samples is overall surface quality, and in order to quantify the improvement in the surface roughness after the machining tests, it is an important parameter to quantify. Surface roughness was measured using a portable rugosimeter MITUTOYO Surftest SJ-210 provided in the DEMEC Workshops. Surface roughness was analyzed in the XY Plane as well as in the XZ or YZ planes (view Figure 4.3). Surface roughness for both as built surfaces is depicted in Table 4.3.

Table 4.3: Surface roughness measurements for the transversal and longitudinal surface.

	R_a (μm)	R_z (μm)
XZ/YZ	5.2353	44.96
XY	9.706	48.030

Note that surface roughness (R_a) in the XY surface is almost the double of the XZ/YZ surface, which might be linked to the fact that this surface is the top surface of the as-built sample which exhibit the laser scan paths in it. The laser scan paths result in a higher surface roughness when compared to the XZ/YZ surface which has the melt pool boundaries presenting lower surface roughness.

4.5 Compression Tests

Quasi-static compression tests were performed for the AM samples in order to characterize the 18Ni300 alloy behaviour in compression, namely the flow stress. The compression tests were carried out in the LET facilities (DEMEC-FEUP) in a MTS 810 servo-hydraulic machine, as displayed in Figure 4.8. The samples for the compression tests were pre-machined into cylinders with 4 mm diameter and 6 mm of length (refer to Figure 4.9). The samples were placed in the testing machine between two tungsten carbide plates in order to prevent damage of the machine plates. The tests were carried out at a speed of 1 mm/min, moreover, it was necessary to define stoppage criteria, which were 90 kN maximum load or 4 mm displacement.

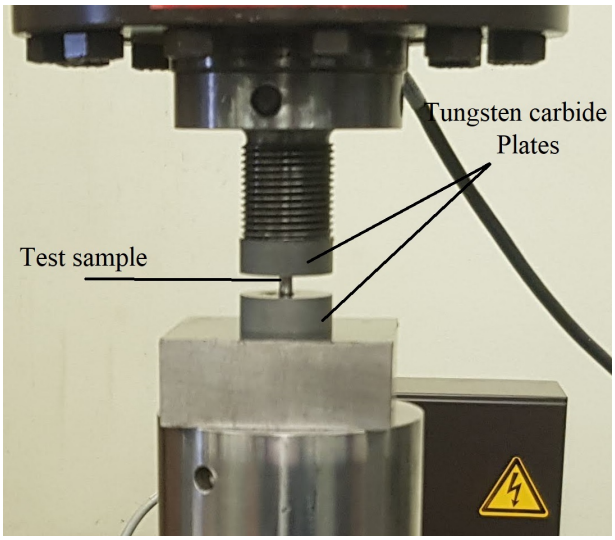

Figure 4.8: Compression test machine (MTS 810) and samples setup.

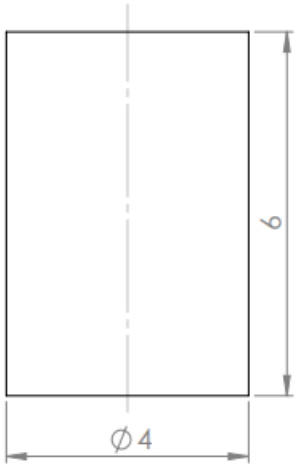

Figure 4.9: Compression testing samples drawing.

In order to ensure test repeatablility, three different samples were analyzed, which were labelled as C1, C2 and C3. The initial and final geometry of the samples can be seen in Figure 4.10. Since no compression tests were carried out for the conventional material, in order to compare the quasi-static behaviour of these samples with the conventional one, data from Couto [42] thesis was also plotted in 4.11.

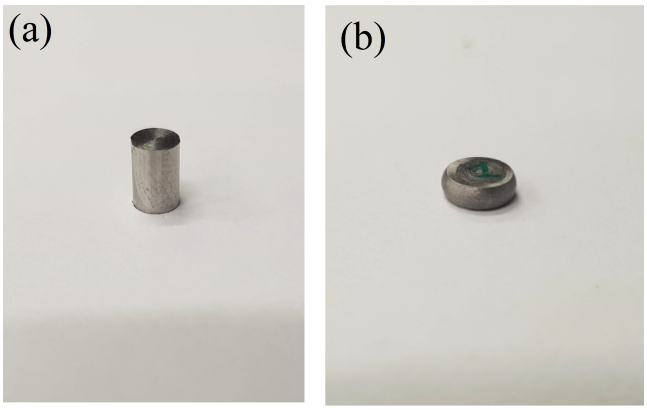

Figure 4.10: Testing samples before (a) and after (b) the compression tests.

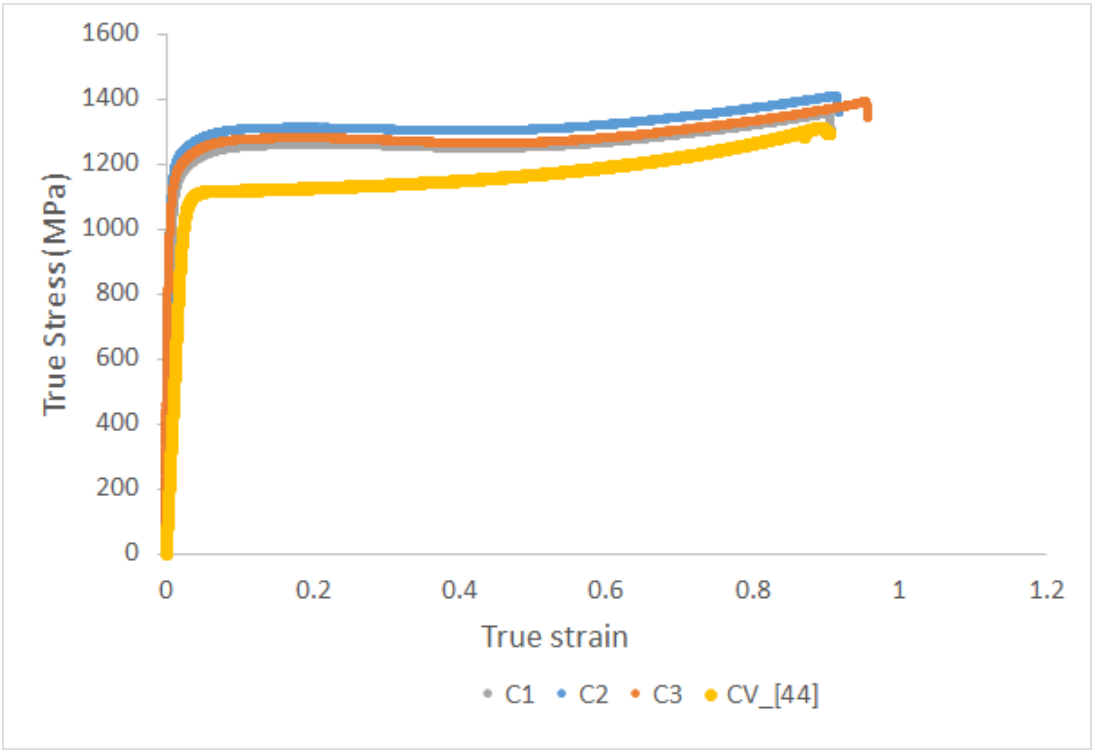

Figure 4.11: True stress-strain curves for the three test samples (AM) and the conventional material [42].

As observed in Figure 4.11, the AM samples have similar behaviour presenting high repeatability. The average yield strength obtained for these samples is around 1100 MPa, which is in accordance with the literature for additive manufactured 18Ni300 maraging steel, which for the least strong direction (Z axis) is about 1000 MPa [43]. Due to being compressed in the same direction as build direction (Z axis) it is expected that the measured yield strength is the minimum for the material, given its anisotropy. The columnar grain formation in Z direction increases grain discontinuity density in the direction perpendicular to build direction, meaning an increase of strength in the XY direction. AM samples have higher yield strength than the conventional

material, which is explained by the finer crystalline structure of these materials, due to the rapid solidification [45]. When comparing both materials, AM presents an higher yield strength than the conventionally produced samples. All the tests were finished when the maximum displacement criterion reached its value of 4 mm.

4.6 Hardness Measurements

Hardness was measured in the metallography lab of INEGI using a EMCO Test M4U-075 hardness measuring machine (refer to Figure 4.12), in two different planes (XZ/YZ and YZ), according to the surface labelling done in 4.3.1. Three measurements were done per surface.

Figure 4.12: Hardness measuring machine (EMCO® Test M4U-075).

Table 4.4: Hardness (HV30) measurements for the different surfaces.

	Hardness (HV30)			
Measurement	**A1.1**	**A2.1**	**A3.1**	**B**
(1)	353	350	356	360
(2)	356	363	354	363
(3)	360	352	347	352
Average ($\bar{x}$)	356	355	352	358

No significant differences were found between the two observed surfaces. The obtained values go in line with the ones found in literature [44], which are about 37 HRC when converted to the Rockwell hardness scale.

4.7 Turning Tests

4.7.1 Turning Tests Setup

The turning operation adopted to perform the experimental turning tests was external cylindrical turning. Two cutting specimens were submitted to the testing campaign, one made from the conventional (CV) material and the other made from AM material. Each specimen had a total length of 120 mm. In order to support the workpiece and reduce vibrations, the cutting length to be machined in each operation was the only section not supported by the chuck. The samples were divided into four sections of 25 mm each (labelled L1-L4). Each section was marked and submitted to a different array of parameters (different combinations of cutting tools, feed rates, depths of cut and cutting speeds), the different combinations provided information that allowed for the comparison of each cutting parameter and tool geometry influence in the cutting forces. Each section allowed 18 different combinations of parameters to be carried out (subjected to a combinations of all feed rates, depths of cut and two cutting speeds per section). No more operations were able to be tested in each length due to the fact that the final diameter shouldn't surpass a minimum value because it would compromise structural integrity of the specimen. The minimum diameter obtained in all the tests was 13 mm. It is important to state that for each section a new insert was used in order to minimize tool wear effects. The cutting conditions used in the experimental campaign are presented in Table 4.5.

Table 4.5: Cutting conditions for the experimental turning tests.

Feed rate (mm/rev)	0.05	0.1	0.2	
Depth of cut (mm)	0.1	0.2	0.3	
Cutting speed (m/min)	60	90	120	150

Turning tests were performed in a OKUMA® LB3000 EX II CNC Lathe (Figure 4.15). In order to evaluate force components evolution over time, a piezoeletric dynamometer was used in the experimental setup enabling the measurement of the three force components (F_f, F_p and F_c). A piezoeletric dynamometer specialized for the turning operations (Kistler® 9129AD, refer to Figure 4.15) connected to a multi-channel signal amplifier (Kistler® 5070A, note Figure 4.15) and a computer with a data acquisition system was used. The toolholder was fixed to the dynamometer plate which was directly attached to the turret of the lathe (Kistler® toolholder type 9129AE25, Figure 4.14), this setup can be seen in Figure 4.13. Figure 4.15 illustrates a schematic of the data acquisition setup.

Figure 4.13: Dynamometer and workpart setup in CNC machine.

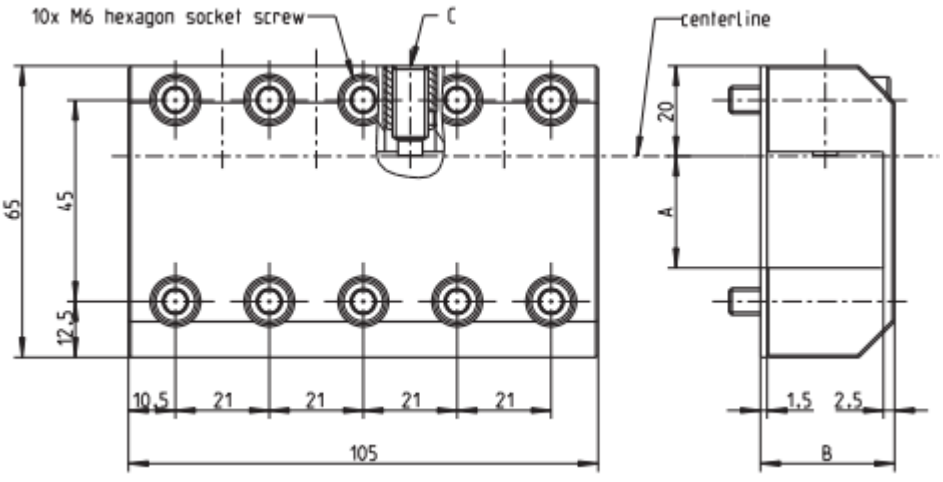

Figure 4.14: Tool holder for lathe chisel for axially mounted dynamometer, Type 9129AE25, Kistler® [46].

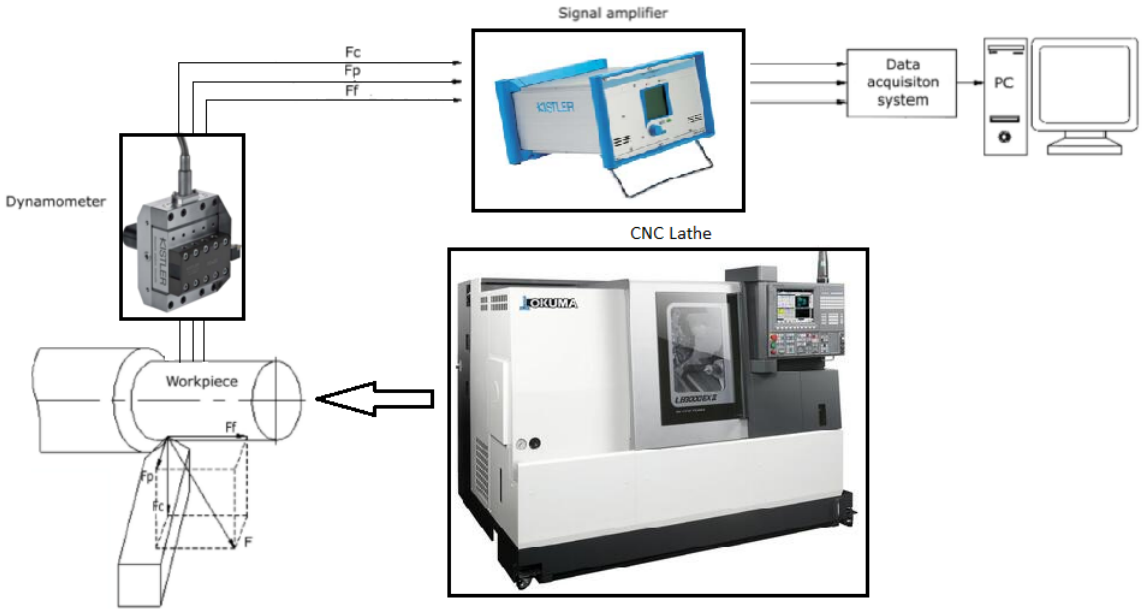

Figure 4.15: Data acquisition setup adapted from [47].

4.7.1.1 Turning Insert

The cutting inserts have been chosen according to manufacturers' recommendation (Palbit S.A.) for the experimental tests campaign presented. Two cutting inserts with a rhombic shape of 55º were chosen to conduct the experimental turning tests (see Figure 4.16). The main difference between the tools is the distinct rake face geometry, one insert fully suited for the finishing operations with a chip-breaker rake face (DCGT 11T304-FS) and the other with a flat rake face, without a chip-breaker (DCGW 11T304) serving as a control insert in order to compare overall cutting performance between each other.

As mentioned, the main difference between both tool inserts is the presence and absence of a chip-breaker, the nominal geometrical dimensions being similar for both inserts. The designation and the ISO reference for the inserts as well as the dimensions are presented in Table 4.6.

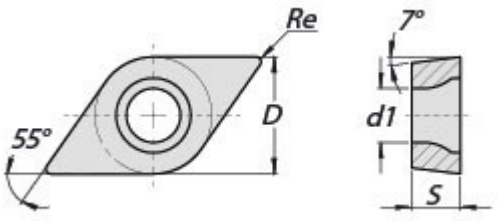

Figure 4.16: Geometrical parameters of the turning inserts.

Table 4.6: Inserts designation and dimensions.

Designation	**ISO reference**	**Dimensions (mm)**			
		D	**S**	**Re**	**d1**
T1	DCGT 11T304-FS	9.525	3.97	0.40	4.40
T2	DCMW 11T304				

Both inserts have the same substrate composition, cemented carbide and the same coating grade. The coating grade is recommended by the manufacturers for finishing operations and consists of a AlTiN applied using a PVD (Physical Vapor Deposition) process. The coating grade and manufacturer's description are indicated in Table 4.7.

Table 4.7: Coating grade and respective description in accordance to Palbit S.A. catalogue.

Designation	**ISO reference**	**Coating Grade**	**Description**
T1	DCGT 11T304-FS	PH7920	A micro grain size combined with the AlTiN PVD coating make it suitable for roughing to finishing operations under good cutting conditions to light interrupted cutting at medium cutting speeds. Suitable for stainless steels & heat resistant super alloys.
T2	DCMW 11T304		

4.7.1.2 Chip Breaker Geometry

Chip breakers improve chip control during cutting operations and enhance tool durability. They promote chip breakage, reducing chip length, which may in turn result in less or no entanglement around the workpiece or cutting tool as well as vibration reduction, improving overall process performance and safety. In order to evaluate the effect of a chip-breaking rake face, a control cutting tool with a flat rake face (DCMW insert, T2) and a tool with a chip-break (DCGT-FS insert, T1) were used in the experimental tests, the details of both tools are illustrated in Figure 4.17.

(a) (b)

Figure 4.17: Turning inserts, Palbit S.A.: (a) DCMW 11T304; (b) DCGT 11T304-FS.

4.7.1.3 Toolholder

The toolholder used for conducting the turning tests was chosen according to the geometry of the inserts and the cutting direction. The toolholder's designation is SDJC L 2020 K11 and its geometrical features are illustrated in Figure 4.18 whereas the dimensions are indicated in Table 4.8. This toolholder specifically, has a 93º side cutting edge angle for the fixture of the insert, the other geometrical angles are 0º.

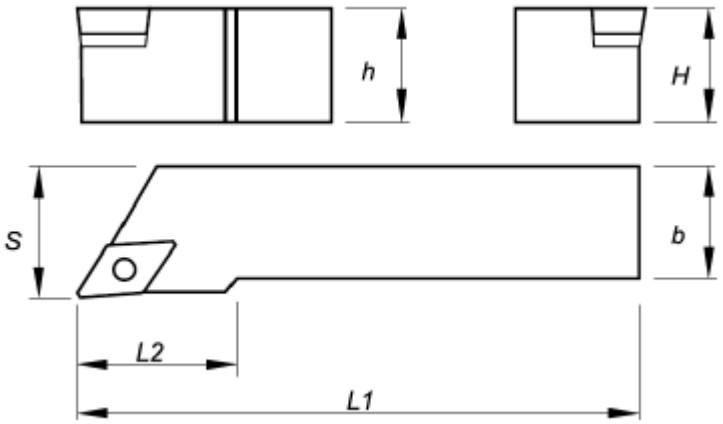

Figure 4.18: Toolholder geometrical features.

Table 4.8: Toolholder geometrical dimensions in accordance with Palbit S.A. catalogue.

Designation	Dimensions (mm)				
SDJC L 2020 K11	H=h	b	L1	L2	S
	20	20	125	22	25

4.7.2 Turning Parameters

In order to evaluate the AM material and comparing it with the conventional material, several aspects were evaluated such as cutting forces, tool wear, chip formation, surface quality, specific cutting pressure and cutting power, for a wide range of parameters within the fine-cutting/finishing operations. Several turning parameters were selected that are usually used in post-processing finishing operations which as-built AM parts are submitted to, allowing for a better understanding of the influence of each parameter in the cutting operation. A list of the different parameters and the respective code used are presented in Table 4.9. Also, in Appendix A a more extensive enumeration and nomenclature used in each particular turning test, as well as the parameters used, is depicted in Table A.1.

All cutting operations were performed in dry cutting conditions, since little amount of material was removed in each test and cutting inserts were replaced after a limited number of operations. Tool wear was not a major concern and cutting fluid would also add more complexity to the machinability analysis. Moreover, cutting fluid could jeopardise the functionality of the data acquisition system, which would require some type of protection in order to prevent damage in these devices.

Table 4.9: Different turning parameters and respective code.

T1	DCGT tool
T2	DCMW tool
V1	Cutting speed of 60 m/min
V2	Cutting speed of 90 m/min
V3	Cutting speed of 120 m/min
V4	Cutting speed of 150 m/min
a1	Depth of cut of 0.1 mm
a2	Depth of cut of 0.2 mm
a3	Depth of cut of 0.3 mm
f1	Feed rate of 0.2 mm/rev
f2	Feed rate of 0.1 mm/rev
f3	Feed rate of 0.05 mm/rev

4.7.3 Surface quality

In order to evaluate the influence of the several cutting parameters in the surface quality of the samples, new turning operations had to be carried out with a combination of several parameters. These turning operations were necessary because the surface quality of each sample section (L1-L4) after the turning tests was that of the last cutting operation performed. All the new turning operations for surface roughnes measurements were carried out using the tool with the chip breaker (DCGT Tool, T2).

4.8 Milling Tests

Milling experimental tests were also carried out using a similar methodology to the one used in turning tests, the experimental procedure will be explained in the next sections. The particular milling operation in this analysis is face milling. Similarly to what was performed during the turning tests, in order to evaluate the AM material and the conventional materials machinability, several aspects were evaluated such as cutting forces, tool wear, chip formation, surface quality, specific cutting pressure, cutting power, for a wide range of parameters.

4.8.1 Milling Tests Setup

The experimental milling campaign was also carried out in Palbit S.A. facilities. All the tests were carried out in a 3-axis CNC machine (MAS® MCV 1270 Figure 4.19). Several cutting speeds, depths of cut and feed rates were combined throughout the experimental tests in order to evaluate the effect of each parameter in the resulting cutting forces and specific cutting pressure. A piezoeletric dynamometer (Kistler® 9257B) coupled to the workpiece with a special fixture system was used. Figure 4.20 illustrates the dynamometer and fixture system assembly. The dynamometer was connected to a multi-channel signal amplifier (Kistler® 5070A) connected to a computer with a data acquisition system (ADVANTECH, refer to Figure 4.21).

Figure 4.19: MAS®MCV 1270 3-axis CNC machine.

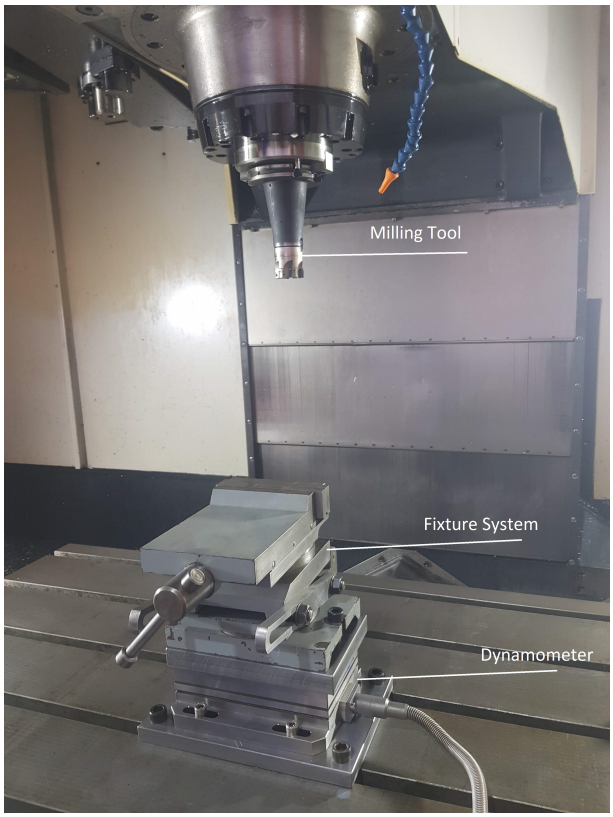

Figure 4.20: Milling tests setup.

Figure 4.21: ADVANTECH portable data acquisition module.

4.8.1.1 Cutting Insert

Due to the inherent complexity of the milling process, in order to simplify the cutting forces and subsequent analysis, only one cutting insert was used. Once again, the cutting insert was selected with the help and expertise of Palbit S.A. Due to the more challenging analysis the milling tests represent, tool geometry influence was not studied and a single insert was used. Its reference is XPET 060204 PDER-LP with AlTiN PVD coating grade labelled PH7920 (the same used in the turning inserts). The geometry, ISO reference and dimensions of the cutting insert are shown in Figure 4.22 and Table 4.10.

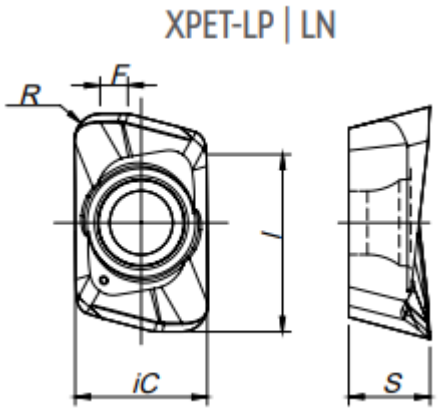

Figure 4.22: Geometrical parameters of the milling insert.

Table 4.10: Milling insert designation and geometrical dimensions.

ISO Reference	Dimensions (mm)				
	iC	S	I	R	F
XPET 060204 PDER-LP	3.9	2.4	5.3	0.4	0.8

4.8.1.2 Milling Tool

The milling tool used for this operation was chosen based on the milling inserts used and the type of milling operation (shouldering). With the expertise of PALBIT S.A. a shouldering milling tool was chosen with the reference LINE PRO 021E20090-05-04-020090 [48]. The dimensions and geometry of the milling tool are illustrated in Table 4.11 and Figure 4.23.

Table 4.11: Milling tool designation and geometrical dimensions.

Reference	No. of inserts (Z)	Dimensions (mm)			
		ϕD_c	L	L1	(MAX) a_p
021E20090-05-04-020090	5*	21	90	35	4

*only one used in the tests

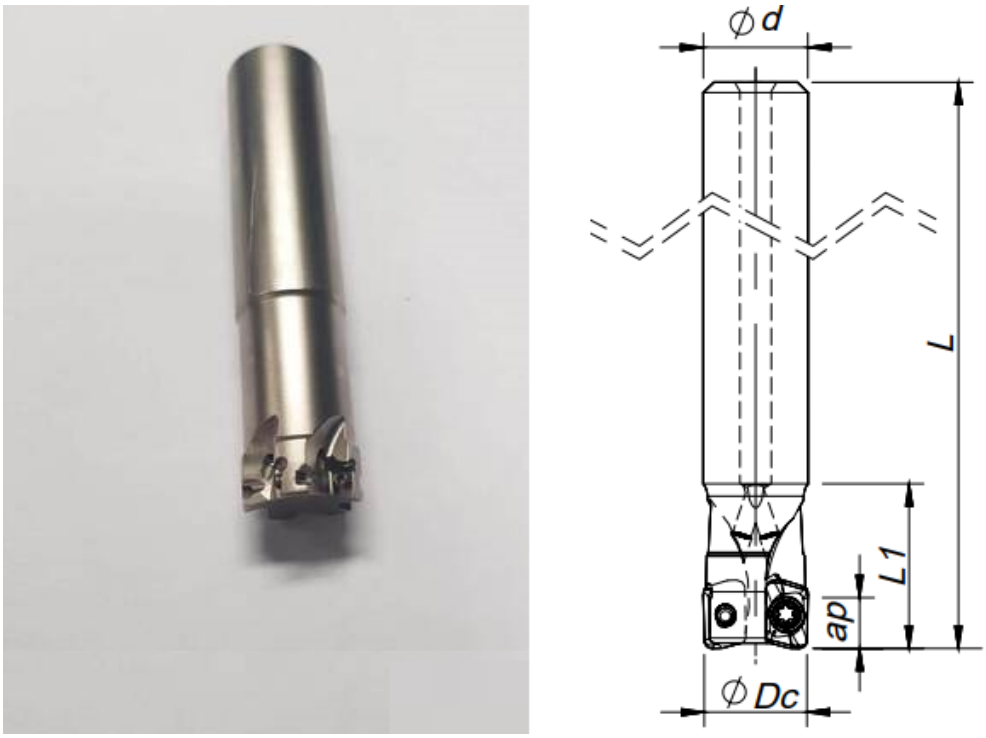

Figure 4.23: Milling tool geometry and dimensional parameters.

4.8.2 Milling Parameters

A list of the several milling parameters and nomenclature to differentiate each operation is depicted in Table 4.12. All cutting operations were performed without the use of cutting fluid, for the reasons mentioned in 4.7.2.

Table 4.12: Different milling parameters and respective code used.

V1	Cutting speed of 80 m/min
V2	Cutting speed of 160 m/min
V3	Cutting speed of 240 m/min
V4	Cutting speed of 320 m/min
a1	Depth of cut of 0.2 mm
a2	Depth of cut of 0.4 mm
a3	Depth of cut of 0.6 mm
f1	Feed per tooth of 0.05 mm/t
f2	Feed per tooth of 0.1 mm/t
f3	Feed per tooth of 0.2 mm/t

Two specimens were submitted to the experimental milling test campaign, one made from the AM material and the other from the conventional (CV) material. Each specimen had a total length of 120 mm and width of 16 mm. The engagement angle between the selected milling

tool and the workpiece is 99.26º. Also, the milling tool was centered in the middle of workpiece in order to prevent assymetries. The samples were divided into four sections (L1-L4), each one subjected to different cutting parameters, being cutting speed the only difference between sections. In Appendix D, Table D shows the different cutting parameters used for each run/cut as well as the identification code for each operation. Each cutting length was subjected to 9 different operations, and when a section was finished, a new insert was used in order to minimize the effect of tool wear, which could jeopardize the data measurements.

Chapter 5

Machining Tests Results and Discussion

5.1 Turning Tests

In this section the results from the turning tests will be analyzed, several aspects will be compared such as the use of different cutting inserts, influence of turning parameters in cutting forces, cutting power and specific cutting pressure as well as the chip morphology, tool wear and surface quality.

5.1.1 Cutting Forces

As mentioned previously, force data was obtained by means of a dynamometer. The resultant force acting on the tool was divided into the three main components and plotted in a graph.

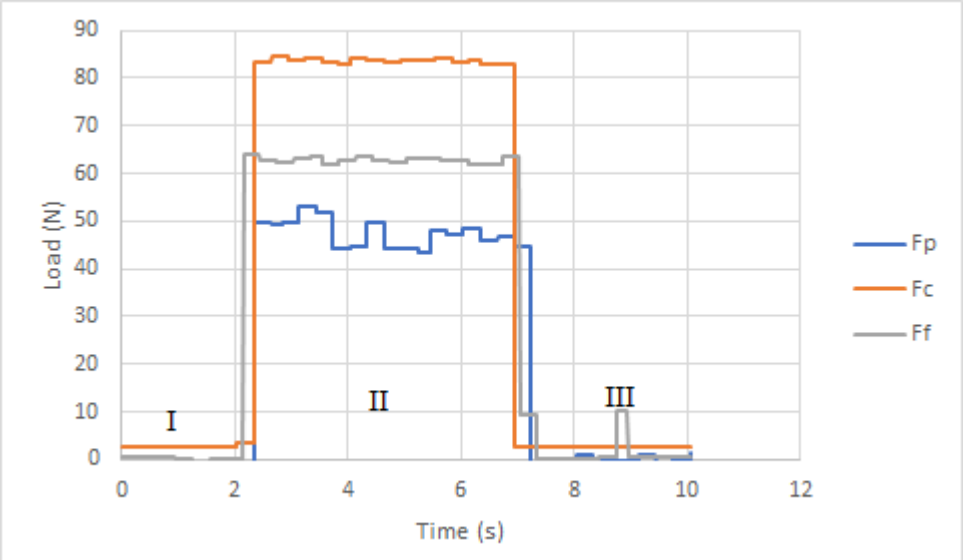

Figure 5.1: AM specimen load spectrum resulting from a cutting tool T2 (DCMW tool), v_c= 90 m/min, f= 0.2 mm/rev and a_p= 0.3 mm.

In figure 5.1 the load force vs. time of a particular cutting operation is illustrated, and it can be seen that several regions appear in the graph: the first region (I) corresponding to the initiation of the data acquisition system, where the lathe is fully stopped, a second region (II) where the actual turning/cutting operation occurs and a third one (III), which corresponds to the return of the cutting tool. Only the main cutting region (region II) will be analyzed in the following sections. Firstly the secondary force components will be analysed (feed and penetration forces), followed by a more careful analysis of the main cutting force. All the load values obtained are an average of the main cutting region (region II). In order to clarify the deviation from the average values portrayed, standard deviation error bars will also be shown in the load plots.

5.1.1.1 Feed and Penetration Forces

For the maximum cutting speed (150 m/min), average feed force (F_f) was analyzed as a function of the feed rate, and penetration force (F_p) as a function of the depth of cut. Figures 5.2 and 5.3 show the plotted data of these variables.

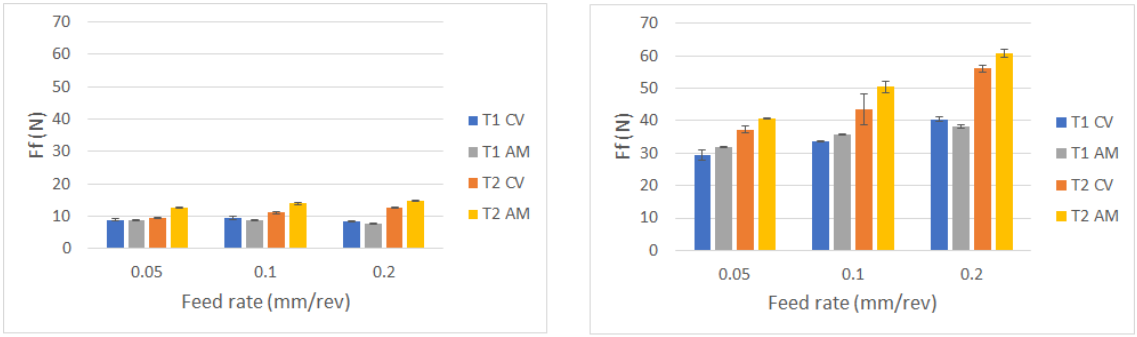

Figure 5.2: Evaluation of the feed force as a function of the feed rate for: (a) a_p=0.1 mm and v_c=150 m/min; (b) a_p=0.3 mm and v_c=150 m/min.

When analyzing the differences between both tools, it is clear that for each set of parameters the forces obtained in the tests using the tool without a chip breaker (T2) are higher than the ones with the chip breaker (T1). Regarding the feed force, when working with the smallest depth of cut (a_p=0.1 mm), the influence of the feed rate is barely noticeable since for the three sets of feed rates there are no major changes in the force. However, these variations are more significant when the depth of cut is increased (a_p=0.3 mm): in Figure 5.2 (b) it is clear that with an increased feed rate, the feed force also increases.

When comparing Figure 5.2 (a) with Figure 5.2 (b) it can be concluded that feed force (F_f) is highly dependent on the depth of cut as expected [49] since, when using the cutting tool T1, for a depth of cut increase from a_p=0.1 mm to a_p=0.3 mm and for a feed rate of 0.05 mm/rev the feed force showed an increase of approximately 21 N (235%) in the conventional material and an increase of approximately 23 N (260%) in the AM material.

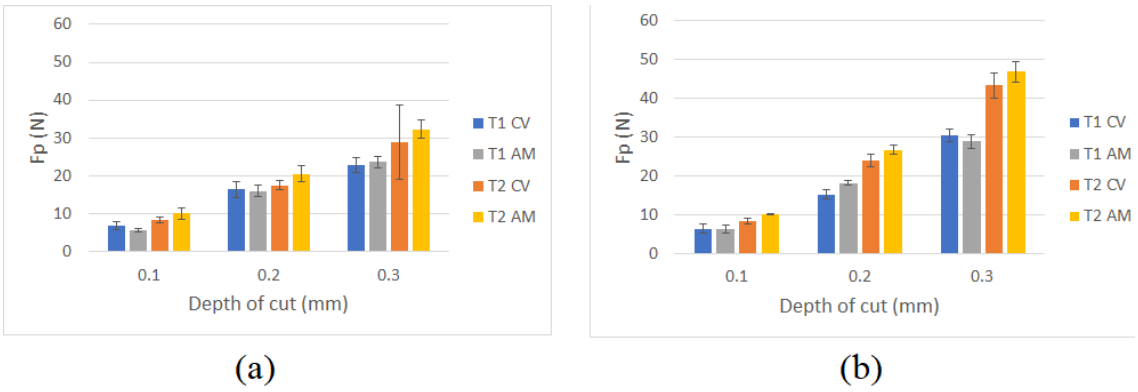

Figure 5.3: Evaluation of the penetration force as a function of the feed rate for: (a) f=0.05 mm/rev and v_c=150 m/min; (b) f=0.2 mm/rev and v_c=150 m/min.

When evaluating the average penetration force, the force magnitude increases with increased depths of cut. In contrast with feed force, there is not a clear dependency of the feed rate in the penetration force. Although in some cases the force increases significantly (a_p=0.3 mm) from f=0.05 mm/rev to f=0.2 mm/rev when using the cutting tool T2 an increase of approximately 15 N (54%) for the conventional material and an increase of approximately 15 N (47%) in the AM material. These differences are not so significant when the depth of cut is smaller. For increased depths of cut, the effect of the feed rate is more significant in the penetration forces.

5.1.1.2 Main Cutting Force

Main cutting force (F_c) is the most relevant force component analyzed when evaluating machinability. Figure 5.4 presents the evolution of the average cutting force as a function of the different turning parameters, the different tools and the different specimens (conventional and AM) that were tested. It is noticeable that when increasing either the depth of cut and/or the feed rate, the magnitude of the cutting force increases for both tools (T1 and T2) and both materials (CV and AM). Only one turning operation is not in accordance with this fact (a_p= 0.1mm; f=0.05 mm/rev and v_c=60 m/min for T1) which may indicate that during this test something anomalous occurred (e.g. chip entanglement around the tool which results in an increase of the cutting force), since for all the other combinations of tool and material the force decreases slightly for these set of parameters.

In almost all situations the cutting forces have higher magnitude when the tool without chip breaker (T2) is being used, which was expected given the fact that a tool with a chip break rake face improves chip evacuation resulting in a decrease in shear resistance, and reduces cutting force magnitude.

The highest cutting force values were attained for the parameters that resulted in a higher uncut chip section, a_p= 0.3 mm and f=0.2 mm/rev, which was expected since an increase in these parameters increases chip section, which increases its shear resistance and thus increases the force needed to complete the shear deformation.

Regarding the cutting speeds, and its influence in the cutting force, there is not a clear pattern regarding the increase of the cutting speed since the cutting force values vary only slightly with this increase even if the turning parameters are at both extremes (highest/lowest feeds/depths of cut). Therefore it can be concluded that there is not a clear influence of the different tested cutting speeds in cutting forces. In some cases a very slight decrease in cutting force happens which may be caused by thermal softening related to an increase in the cutting speed, that causes the material to become softer, leading to an easier chip removal thus resulting in a lower cutting force. Note that these differences are not very significant, which allows to conclude that while being an important parameter, cutting speed is not as influential in the cutting force as the feed rate and depth of cut.

No significant differences were found when measuring the cutting forces for AM and conventional materials for the same cutting tool and in some cases, the cutting force is higher in the conventional material whereas in other cases is higher in the AM material. There is, however, a clear tendency for obtaining slightly higher cutting loads for the conventional material, using the T1 tool. When considering T2 tool, the opposite is verified.

Average resultant force (F_R) as a function of the several parameters involved is illustrated in Figure 5.5. All the different parameters combinations are shown in order to compare this force magnitude with the main cutting force. For smaller feeds and depths of cut, resultant force values are very close to the cutting force, for the smallest cutting speed (60 m/min) and for a_p= 0.1mm and f=0.1 mm/rev, for the cutting tool T1 the difference between the resultant force and the cutting force is approximately 1.6 N (4%) for the conventional material and approximately 3 N (7%) for the AM material, which means that the cutting force is the main force component involved in this parameter combination.

Regarding higher depths and feed rates, the values are more discrepant; for example for the combination of parameters, a_p=0.3 mm and f=0.2 mm/rev, for a cutting speed of 60 m/min and for the cutting tool T1, the difference between the resultant force and the cutting force is approximately 18 N (11%) for the conventional material and approximately 11 N (7%) for the AM material, leading to the conclusion that for higher feeds and depths of cut the penetration and feed forces have a more relevant contribution in the resultant force.

The obtained results are coherent with previously performed machinability tests on a similar alloy [42] (same material but from a different build batch), with the same cutting cutting tools and similar cutting parameters, only minor differences are verified between tests (average difference is about 5 N). It can be concluded that the tests present excellent repeatability even if materials were manufactured in distinct AM machines for different manufacturers. Figures 5.6 and 5.7 compare the results of the turning tests of this thesis with the similar turning tests performed in [42]. The labelling of these plots is described as follows: T1 and T2 refers to the tools, AM and CV to the materials (additive manufactured and conventionally manufactured). A comparative table depicting load values for both thesis is presented in Appendix C.

Figure 5.4: Cutting force (F_c) evolution as a function of the turning parameters and the cutting tools for the both specimens (CV and AM).

Figure 5.5: Resultant force (F_R) evolution as a function of the turning parameters and the cutting tools for the both specimens (CV and AM).

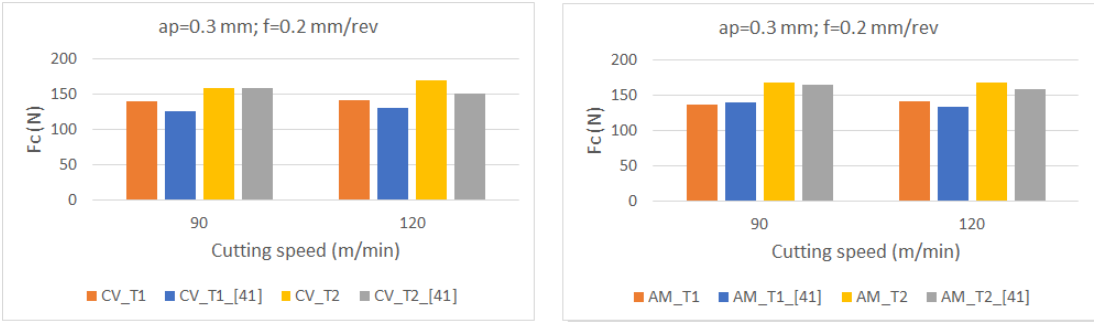

(a) (b)

Figure 5.6: Cutting force comparison between André's results [42] and this thesis' results for an a_p= 0.3 mm and f= 0.2 mm/rev; (a) conventional material; (b) AM material.

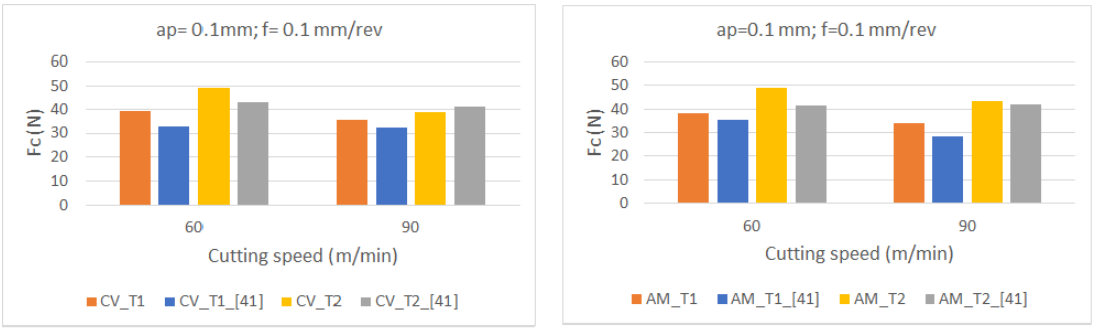

(a) (b)

Figure 5.7: Cutting force comparison between André's results [42] and this thesis' results for an a_p= 0.1 mm and f= 0.1 mm/rev; (a) conventional material; (b) AM material.

5.1.2 Cutting Power

The power consumption required to perform a certain turning operation can be calculated using the equation mentioned in 3.6 or, based on the experimental results obtained from the average cutting force and the cutting speed:

$$P_c = F_c \cdot v_c \times F_f \cdot v_f \tag{5.1}$$

The second term ($F_f \cdot v_f$) of this equation will be discarded in the following analysis due to the fact that its magnitude is much smaller than that of the first term ($F_c \cdot v_c$) of the equation.

Since cutting power is a function of the cutting force, and the latter is heavily influenced by the feed rate and depth of cut, an analysis was carried out to evaluate the influence of these parameters in the cutting power. For the highest cutting speed, v_c=150 m/min, a comparative analysis between tools and materials was carried out and the influence of the feed rate and depth of cut is portrayed in Figures 5.8 and 5.9.

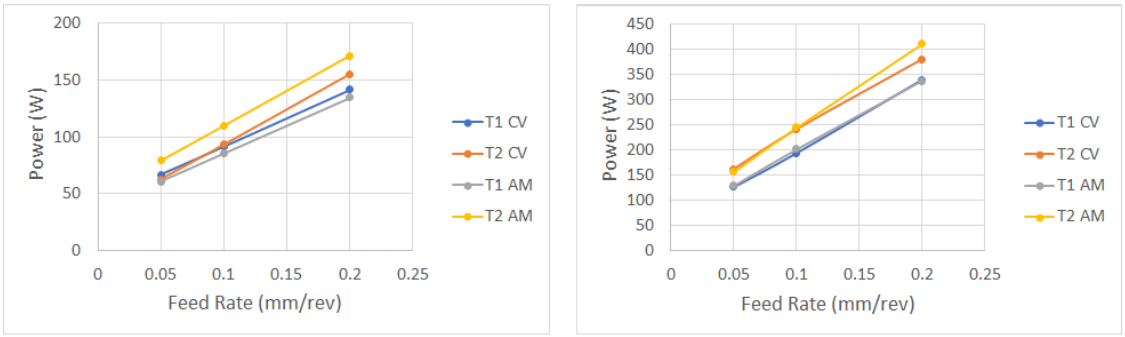

Figure 5.8: Cutting power as a function of the feed rate for: (a) a_p=0.1 mm and v_c=150 m/min; (b) a_p=0.3 mm and v_c=150 m/min.

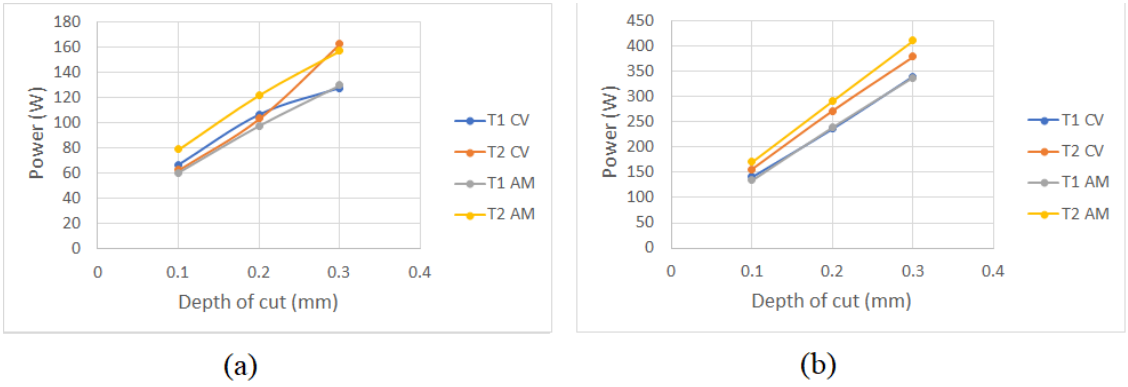

Figure 5.9: Cutting power as a function of the depth of cut for: (a) f=0.05 mm/rev and v_c=150 m/min; (b) f=0.2 mm/rev and v_c=150 m/min.

Cutting power increases almost linearly with the increase of either the feed rate and the depth of cut. For almost all situations, the tool without the chip breaker (T2) presents a higher power consumption, as expected, considering that the cutting forces were also higher than the ones achieved with cutting tool T1. When comparing both materials, when using cutting tool T2, the power consumption in the AM materials is higher than the power consumption of the conventional material. However, when using cutting tool T1, the power consumption of the AM material is slightly lower or practically the same as the conventional material, which is in accordance with the cutting forces obtained in 5.1.1.2.

5.1.3 Specific Cutting Pressure

Specific cutting pressure is an important parameter to assess material machinability or resistance to cutting. It is calculated as the ratio between the main cutting force (F_c) and the cross-section area of an undeformed chip (A).

$$K_c = \frac{F_c}{A} \tag{5.2}$$

The cross-section area of an undeformed chip is calculated as a function of the depth of cut (a_p) and the feed rate (f):

$$A = a_p \cdot f \tag{5.3}$$

Results for the different cutting speeds tested are shown in Figures 5.10 to 5.13.

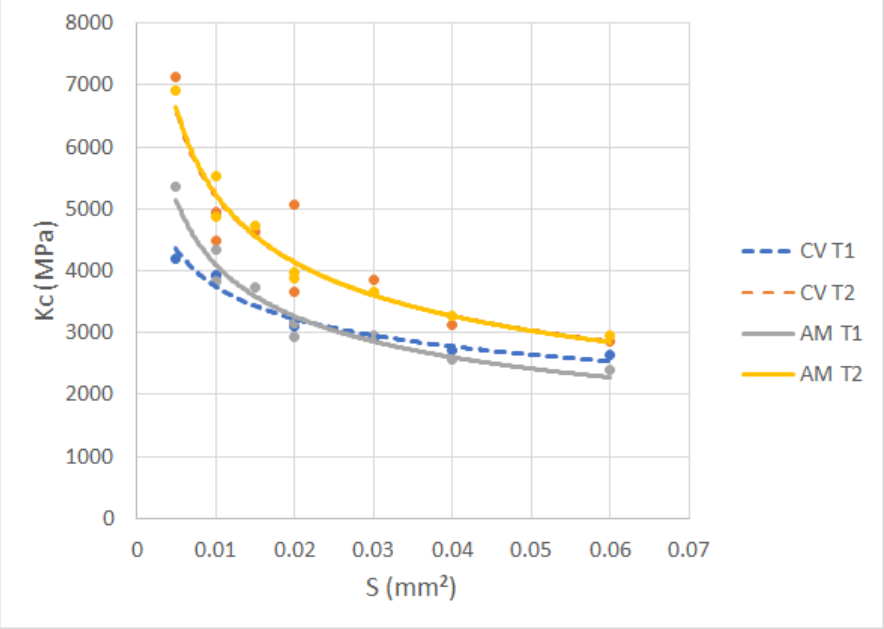

Figure 5.10: Specific cutting pressure, K_c, as a function of the cross-section area of undeformed chip, S, for the conventional and AM material and for the different tools, for a cutting speed, v_c=60 m/min.

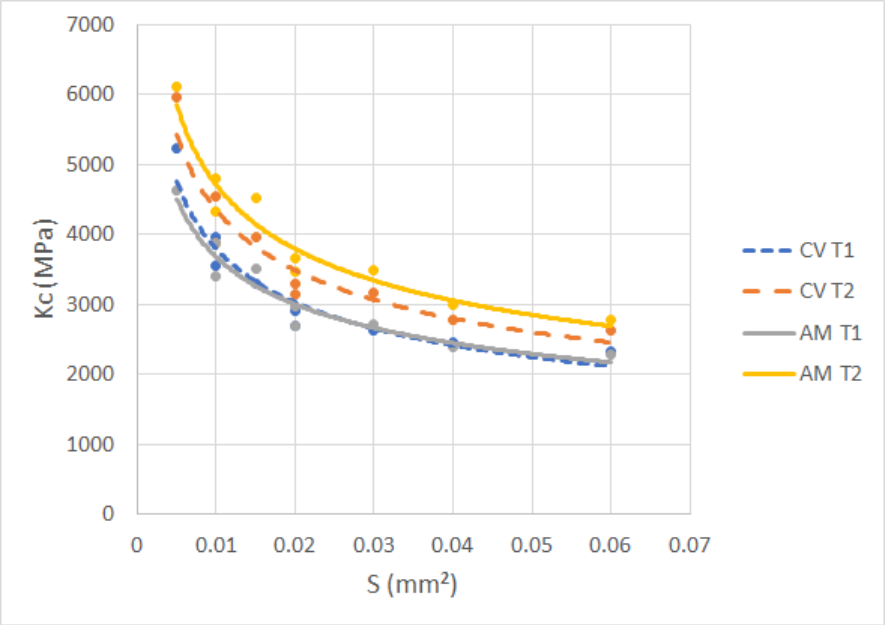

Figure 5.11: Specific cutting pressure, K_c, as a function of the cross-section area of undeformed chip, S, for the conventional and AM material and for the different tools, for a cutting speed, v_c=90 m/min.

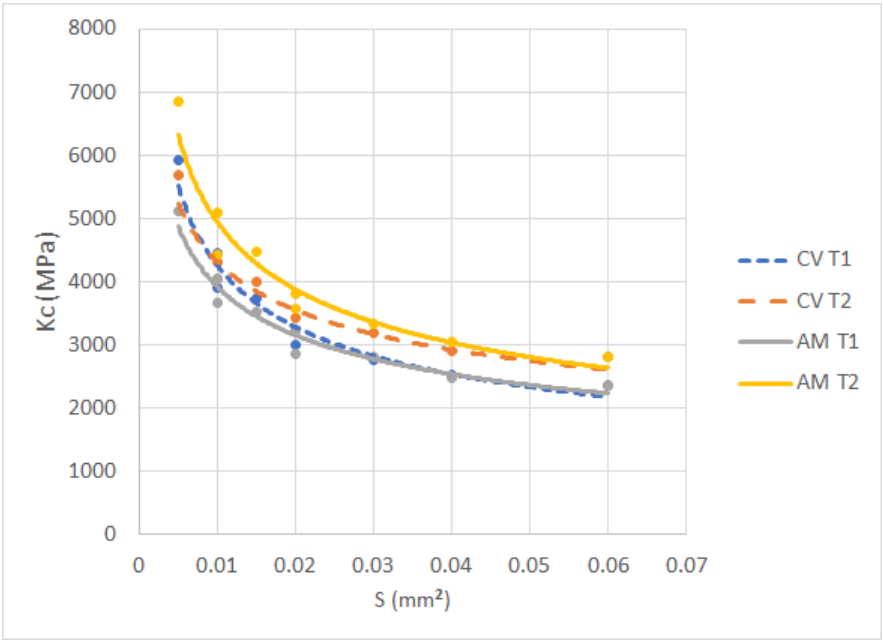

Figure 5.12: Specific cutting pressure, K_c, as a function of the cross-section area of undeformed chip, S, for the conventional and AM material and for the different tools, for a cutting speed, v_c=120 m/min.

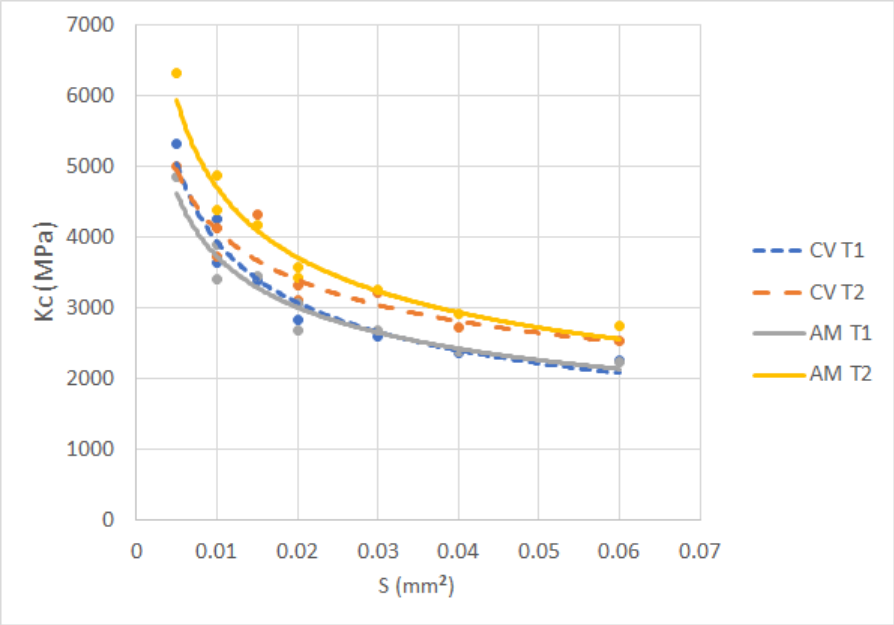

Figure 5.13: Specific cutting pressure, K_c, as a function of the cross-section area of undeformed chip, S, for the conventional and AM material and for the different tools, for a cutting speed, v_c=150 m/min.

Analyzing these graphs, for smaller depths of cut and feed rates, which translate into smaller cross-section areas of the chips, the specific cutting pressure shows an exponential growth. When chip size is increased, specific cutting pressure tends to stabilize at a certain value. However higher discrepancies between different tools appear. The difference between materials, in general, is not very significant.

Comparing both tools, for all the cutting speeds, cutting tool T2 presents higher cutting pressure values, and generally the highest values are achieved when machining the AM material which is related to the fact that for most cases, the main cutting force is higher for the AM material than the conventional one.

When evaluating the influence of the cutting speed, the values of the specific cutting pressure are very similar for different cutting speeds, therefore the conclusion can be taken that cutting speed is not as influential in the cutting pressure as the other turning parameters (e.g. feed rate).

5.1.4 Chip Morphology

During the turning tests, for each combination of parameters, samples of the chips were collected and labeled. Figures 5.14 to 5.17 show the different chip geometries as a function of the different cutting parameters (depth of cut, feed, cutting speed and tool used) for both materials (AM and CV).

All chips were classified in accordance with ISO 3685 standard (Figure 3.10) and only 5 types of chip geometries were obtained: 1.3, 2.3, 4.1, 4.2 and 4.3 (refer to Table 5.1). The chip classification for each turning test is depicted in Table 5.2. Note that this analysis is subjective and sometimes, the classification of a certain chip can fall into one or more categories, due to the fact that more than one chip geometry may be present in the chips collected. Chip analysis is an important aspect in order to evaluate material's machinability since it can be related to overall surface quality and safety during the operations.

Table 5.1: Chip forms obtained in the turning tests.

Chip classification	**Correspondent geometry**
1.3	Snarled ribbon chips
2.3	Snarled tubular chips
4.1	Long washer-type helical chips
4.2	Short washer-type helical chips
4.3	Snarled washer-type helical chips

Almost all cutting parameters configuration resulted in long, continuous and snarled chips, which are unfavorable shapes. The only favorable chip geometry was obtained when using cutting tool T2 in the conventional material, for a cutting speed of 90 m/min and with a feed rate of 0.2 mm/rev and a depth of cut of 0.3 mm, which resulted in short, washer-type helical chips. This type of chip geometry allows ease chip disposal and improves surface quality since, long chips tend to get tangled around the cutting tool and may damage the surface of the workpiece.

Cutting speed does not seem to have a significant influence in the chip morphology. In terms of the cutting tool, it can be concluded that the use of a chip breaker with these parameters does not have a significant difference in the chip geometry, considering that the chips obtained with or without the chip breaker are long and snarled. This can be related to the fact that, during the cutting operations, the rate at which the chip is fed into the tool is not high enough to cause the breakage of the chip, leading to long chip geometry instead of short chips, which is the main function of a chip breaker in a cutting tool.

When increasing the feed rate, the chip geometries are altered for almost every case; in most cases the snarled chips become long continuous chips without snarling. Low influence of the depth

of cut on the chip morphology was noticed.

No significant differences were found regarding chip morphology according the material manufacturing process (AM or conventional).

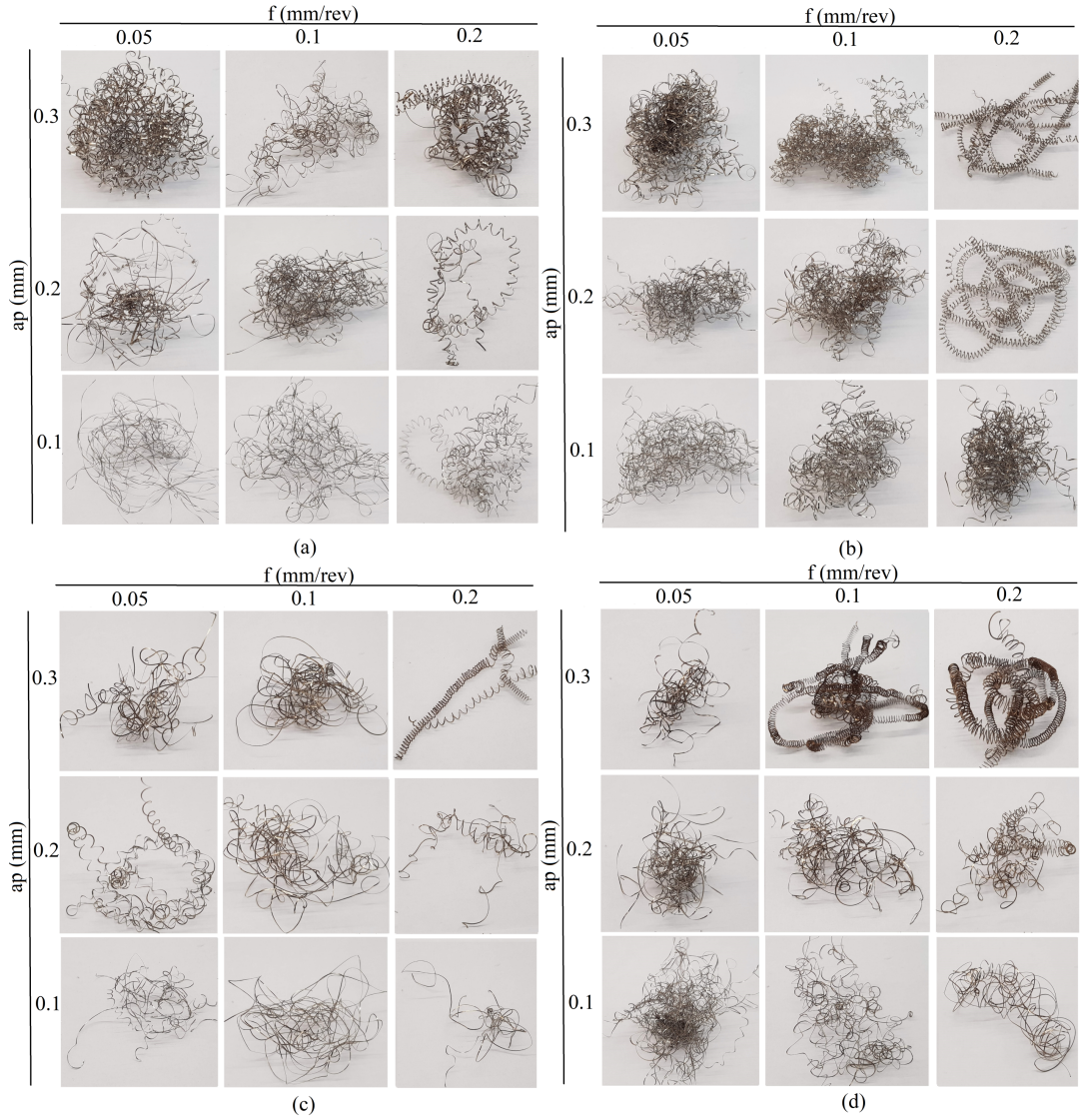

Figure 5.14: Chip morphology of the AM material obtained from the turning tests: (a) T1, v_c=60 m/min; (b) T1, v_c=90 m/min; (c) T2, v_c=60 m/min; (d) T2, v_c=90 m/min.

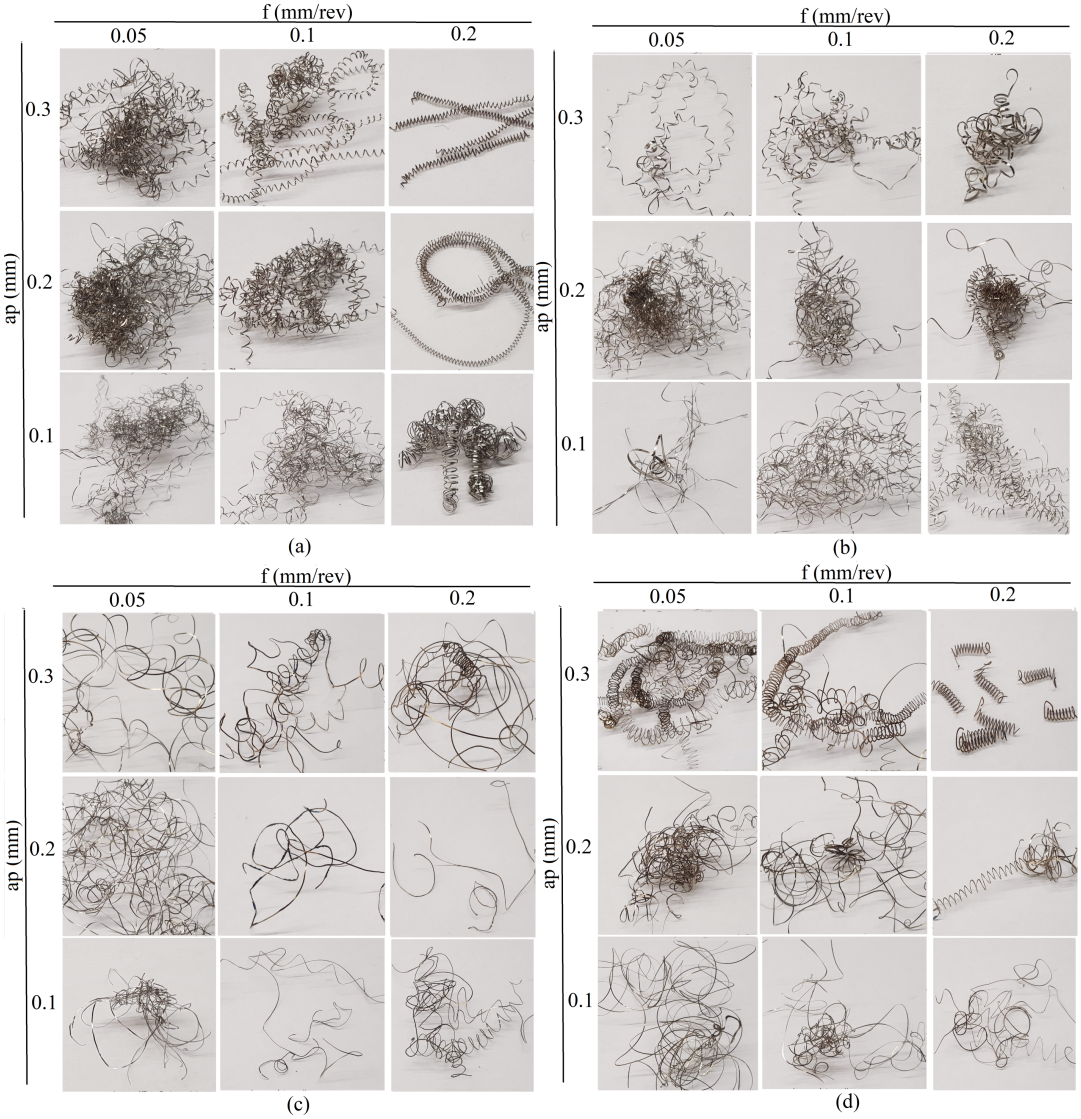

Figure 5.15: Chip morphology of the conventional (CV) material obtained from the turning tests: (a) T1, v_c=60 m/min; (b) T1, v_c=90 m/min; (c) T2, v_c=60 m/min; (d) T2, v_c=90 m/min.

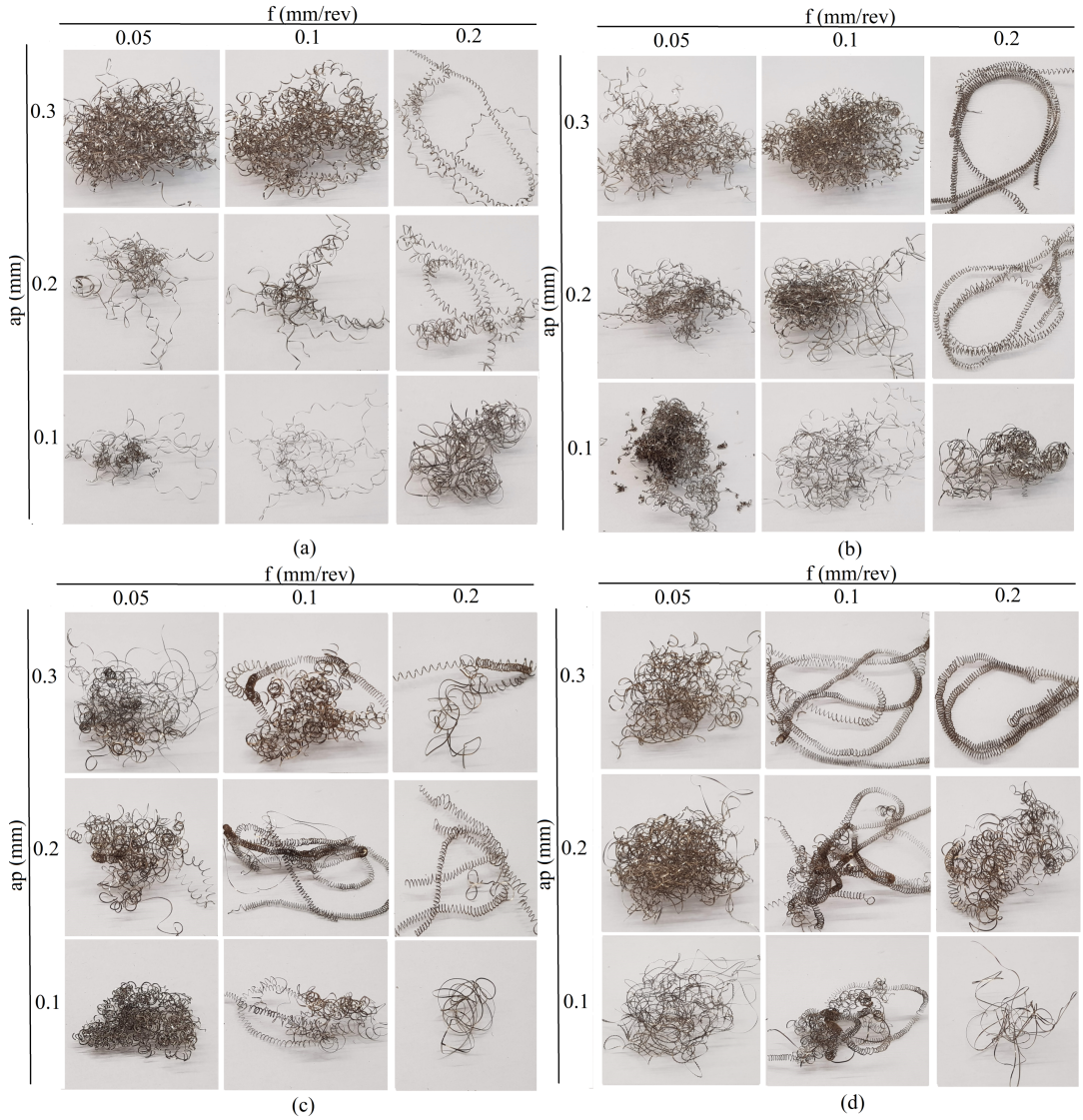

Figure 5.16: Chip morphology of the AM material obtained from the turning tests: (a) T1, v_c=120 m/min; (b) T1, v_c=150 m/min; (c) T2, v_c=120 m/min; (d) T2, v_c=150 m/min.

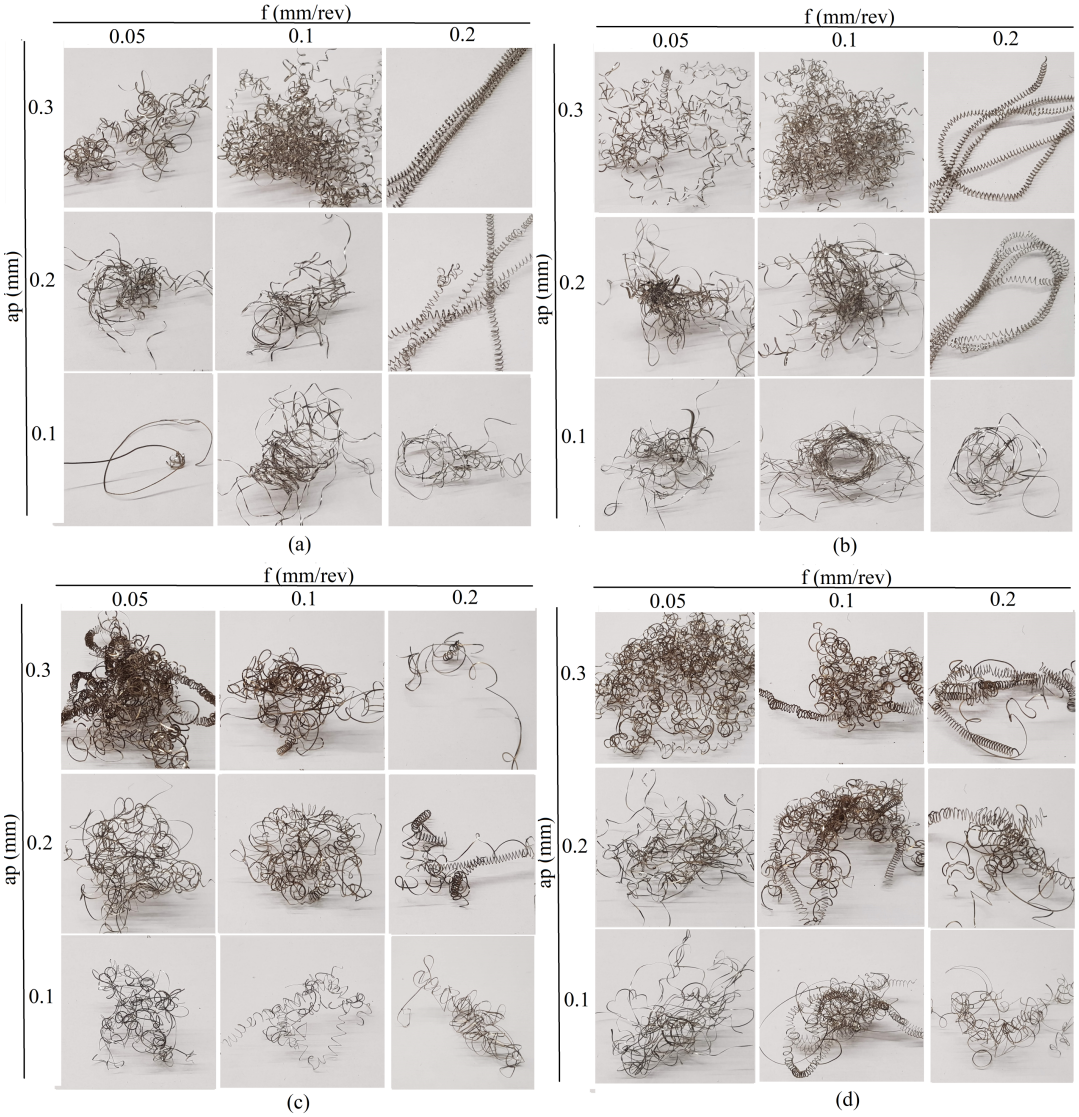

Figure 5.17: Chip morphology of the conventional (CV) material obtained from the turning tests: (a) T1, v_c=120 m/min; (b) T1, v_c=150 m/min; (c) T2, v_c=120 m/min; (d) T2, v_c=150 m/min.

Table 5.2: Chip classification for each cutting parameter in accordance with the ISO 3685 standard.

			Conventional		**AM**	
Cutting speed	**Depth of cut (mm)**	**Feed**	**Tool**		**Tool**	
(m/min)	**(mm)**	**(mm/rev)**	**T1**	**T2**	**T1**	**T2**
150	0.3	0.05	2.3	2.3	2.3	2.3
		0.1	4.3	4.3	4.3	4.1
		0.2	4.1	4.3	4.1	4.1
	0.2	0.05	1.3	2.3	2.3	2.3
		0.1	1.3	4.3	1.3	4.1
		0.2	4.1	2.3	4.1	4.3
	0.1	0.05	1.3	1.3	2.3	1.3
		0.1	1.3	4.3	1.3	4.3
		0.2	1.3	2.3	2.3	1.3
120	0.3	0.05	2.3	4.3	2.3	2.3
		0.1	4.3	2.3	4.3	4.3
		0.2	4.1	1.3	4.1	2.3
	0.2	0.05	1.3	2.3	1.3	2.3
		0.1	1.3	4.3	2.3	4.1
		0.2	4.1	4.3	4.3	4.1
	0.1	0.05	1.3	2.3	1.3	4.3
		0.1	1.3	2.3	1.3	4.3
		0.2	1.3	2.3	2.3	1.3
90	0.3	0.05	4.1	4.3	2.3	1.3
		0.1	2.3	4.3	4.3	4.3
		0.2	2.3	4.2	4.1	4.3
	0.2	0.05	2.3	1.3	1.3	1.3
		0.1	1.3	1.3	2.3	2.3
		0.2	2.3	2.3	4.1	2.3
	0.1	0.05	1.3	1.3	1.3	1.3
		0.1	2.3	1.3	2.3	2.3
		0.2	4.3	2.3	2.3	1.3
60	0.3	0.05	2.3	2.3	2.3	2.3
		0.1	4.3	1.3	2.3	1.3
		0.2	4.1	4.1	4.3	4.1
	0.2	0.05	2.3	2.3	1.3	2.3
		0.1	4.3	1.3	2.3	1.3
		0.2	4.1	2.3	2.3	2.3
	0.1	0.05	2.3	1.3	1.3	1.3
		0.1	2.3	1.3	1.3	1.3
		0.2	4.3	1.3	4.3	1.3

5.1.5 Tool Wear

Tool wear is a key factor in order to assess material's machinability, since harder to machine materials present a higher tool wear. As mentioned previously, during the turning tests, for each section of the workpiece specimens, a new cutting insert was used in order to prevent inaccuracies due to tool wear in the cutting forces. In most cases, the tool wear was only superficial, and no clear geometrical changes occured; only small portions of the coating were removed due to the abrasion between the workpiece and the cutting tool.

The most severely damaged inserts are illustrated in Figures 5.19 to 5.21. In the most damaged inserts, the coating is damaged in the rake face, and also, these tools present build-up edges (BUE). For comparison purposes the geometry of the unused cutting inserts is portrayed in Figure 5.18.

Comparing the tool wear in the conventional material versus the AM material, the most damaged cutting inserts appear when machining the conventional material. A plausible explanation for this occurance may be related to the fact that the AM material has a lower relative density than the conventional one, which may lead to chips breaking easier due to porosity effects, eventually resulting in a lower tool wear. Figure 5.19 portrays the cutting insert with the most tool wear in which, the chip breaker is also damaged.

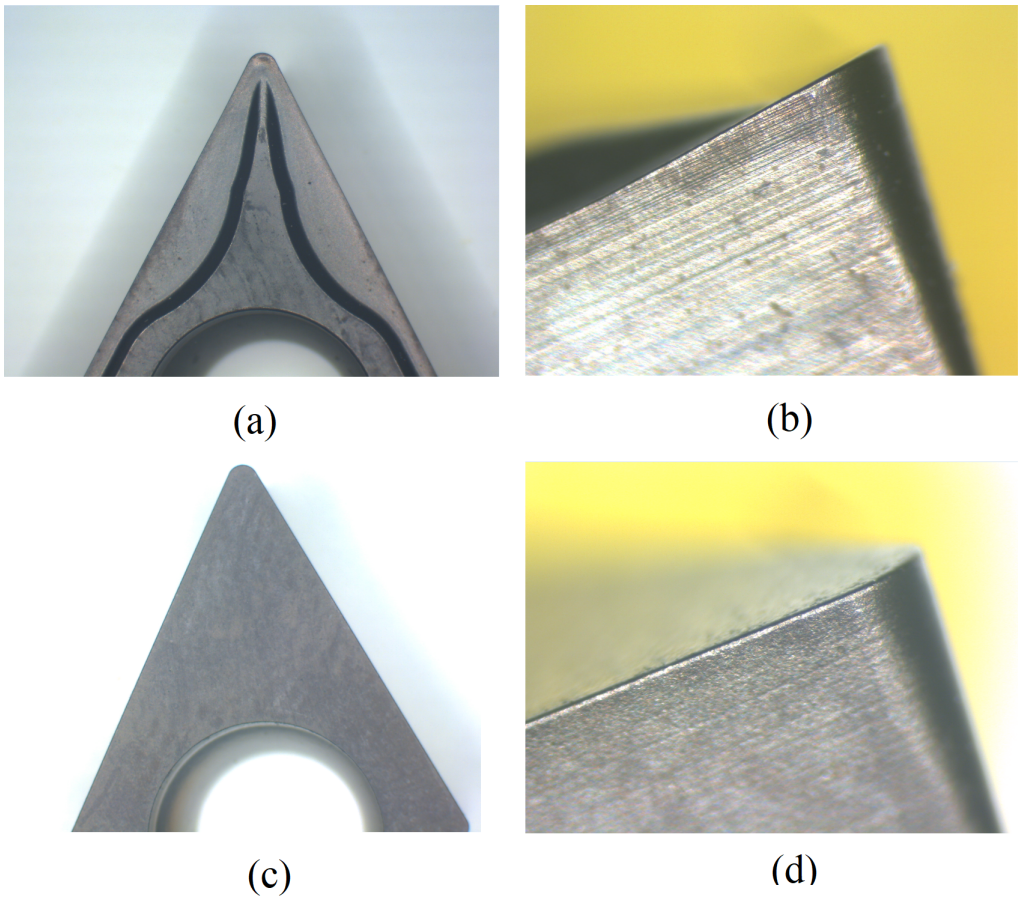

Figure 5.18: Unused cutting inserts: (a)(b) DCGT tool (T1); (c)(d) DCMW tool (T2).

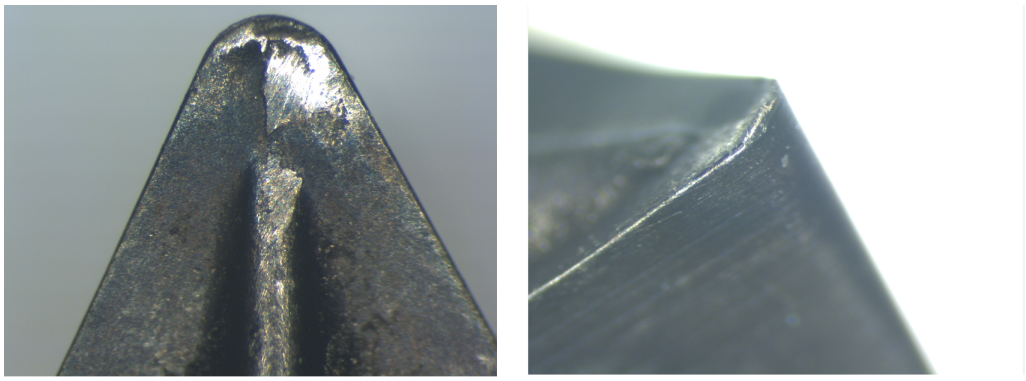

Figure 5.19: Tool wear detail of cutting tool DCGT (T1) used in the machining of the conventional material, for the specimen length L1: (a) rake face; (b) clearance face and tool tip edge.

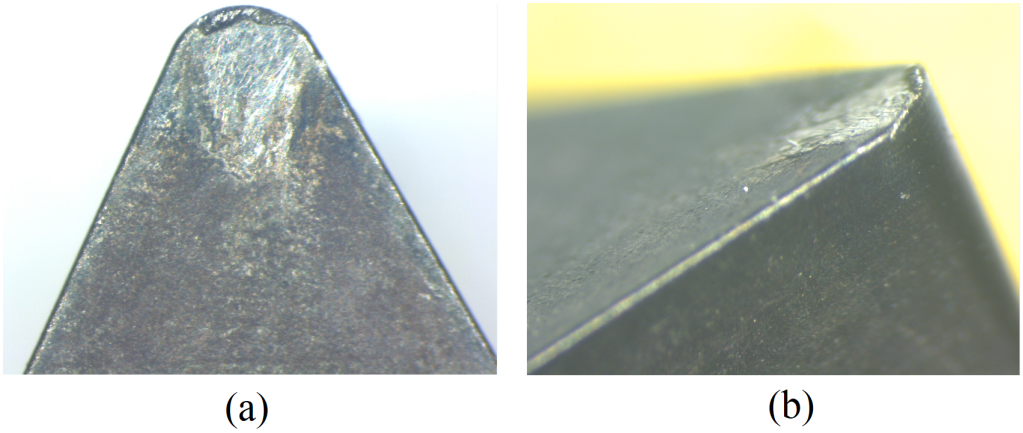

Figure 5.20: Tool wear detail of cutting tool DCMW (T2) used in the machining of the conventional material, for the specimen length L3: (a) rake face; (b) clearance face and tool tip edge.

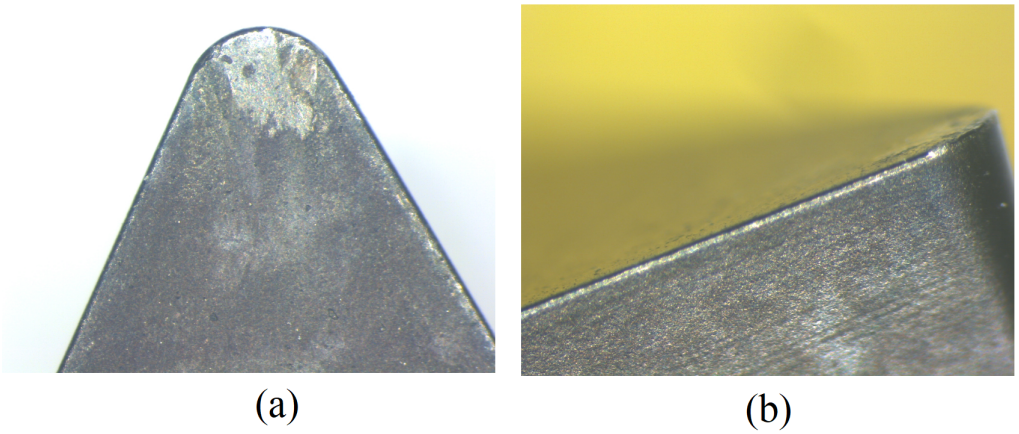

Figure 5.21: Tool wear detail of cutting tool DCMW (T2) used in the machining of the AM material, for the specimen length L4: (a) rake face; (b) clearance face and tool tip edge.

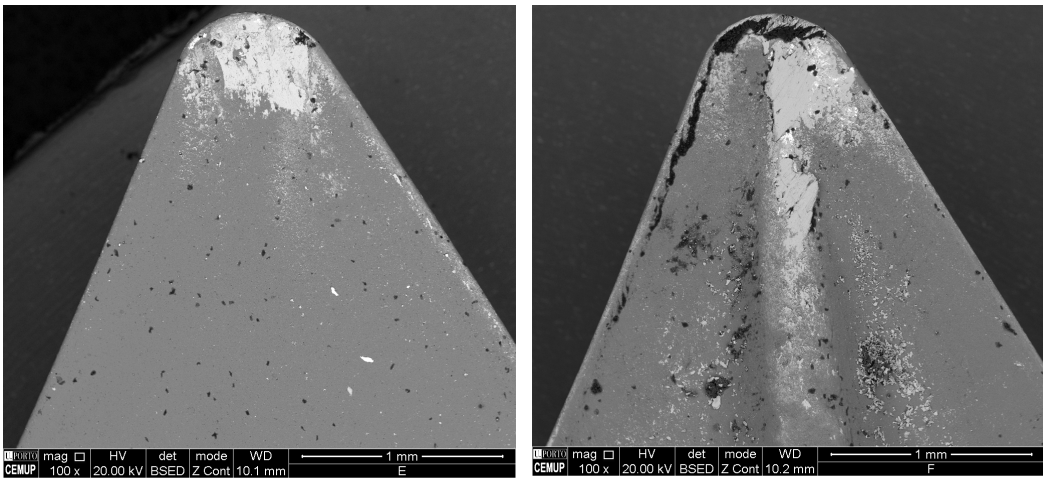

Figure 5.22: SEM images of the cutting edge: (a) DMCW tool used in the machining of the AM specimen for section L4; (b) DCGT tool used in the machining of the conventional specimen for section L1.

Scanning Electron Microscopy (SEM) images of both cutting inserts were obtained. The presence of a Built-up Edge (BUE) is clearly noticeable in Figure 5.22 (b). Unfortunately no chemical analysis was performed in order to understand the chemical composition of the lighter gray area, but the most likely occurrence is workpiece material adherent to the cutting edge.

5.1.6 Surface Quality

The turning operations for surface roughness measurements were performed in the Department of Mechanical Engineering Workshop and the parameters chosen for each cutting length in Table 5.3 as well as a schematic of the length labelling done in the samples (Figure 5.23).

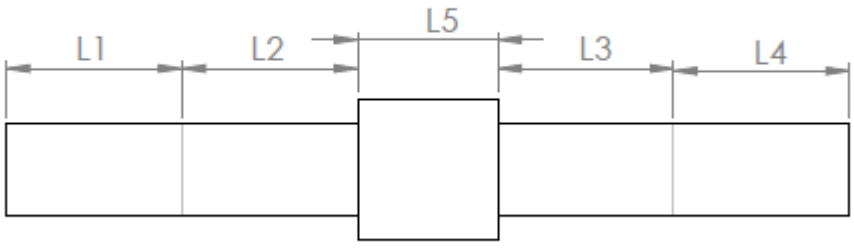

Figure 5.23: Sample length labelling for surface roughness measurements.

Note that in section L5 a distinction needs to be made for the cutting speeds because the section diameter was different in both samples, however all the corresponding cutting speeds in m/min was approximately v_c = 100 m/min.

Table 5.3: Turning parameters for posterior surface roughness measurements and respective cutting speed (labelling used in the turning operations).

			n (rpm)
Section	a_p **(mm)**	f **(mm/rev)**	**CV/AM**
L1	0.1 mm	0.05 mm/rev	1800
L2	0.1 mm	0.2 mm/rev	
L3	0.3 mm	0.2 mm/rev	
L4	0.3 mm	0.05 mm/rev	
L5	0.1 mm	0.1 mm/rev	2500

Surface roughness measurements were carried out in the CETRIB - Tribology Laboratory of INEGI. Each section was subjected to several measurements and average results were considered, as depicted in Table 5.4.

Figure 5.24 shows the influence of the feed rate on the surface roughness of AM and conventional 18Ni300 maraging steel, for an a_p of 0.1 mm. Most probably due to chip accumulation (BUE), surface roughness was poor for the smallest feed-rate, which is supported by the detailed image of section L1 in Figure 5.25, where surface deterioration is observed at macroscopic scale. Tool wear and vibration may, as well, be the cause of the resultant poor surface finish. Nonetheless, generally, with the increase of the feed rate, the surface roughness increases, as expected. When comparing both materials, without taking into account section L1, the surface roughness values are very similar and it can be concluded that no significant difference regarding surface quality between samples was found.

Table 5.4: Surface roughness measurements for the turning samples.

			R_a (μm)		R_z (μm)	
Section	a_p	f **(mm/rev)**	**CV**	**AM**	**CV**	**AM**
L1	0.1	0.05	0.410	1.270	2.437	10.413
L2	0.1	0.2	2.717	2.603	13.293	12.723
L3	0.3	0.2	2.727	2.687	13.143	13.407
L4	0.3	0.05	0.580	0.827	3.673	5.523
L5	0.1	0.1	0.683	0.650	4.127	3.840

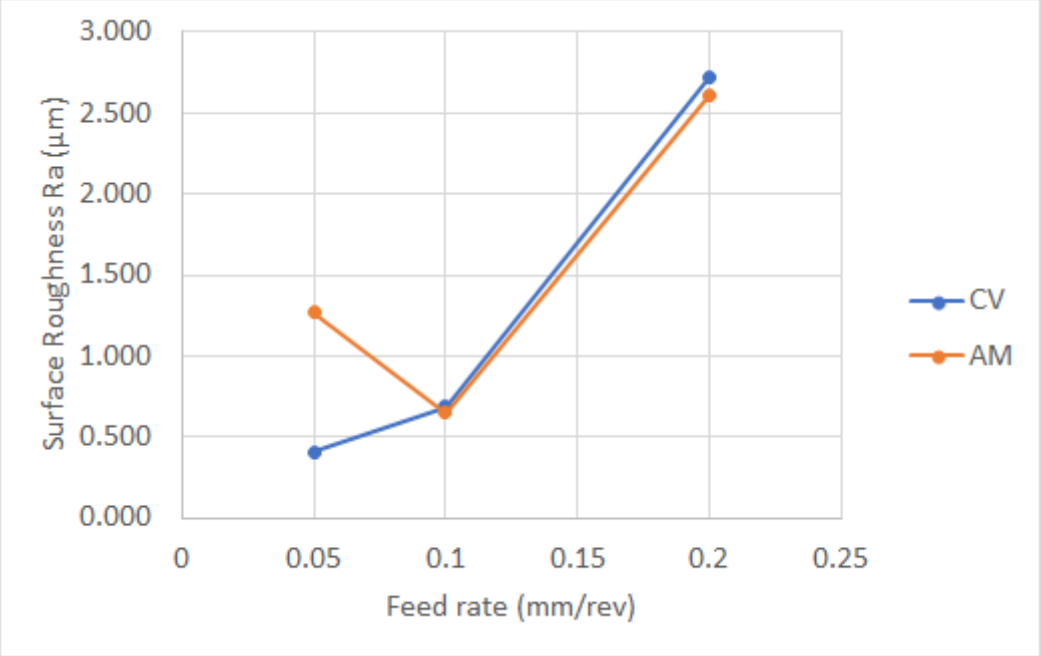

Figure 5.24: Surface roughness as a function of the feed rate for an $a_p = 0.1$ mm.

Figure 5.25: Section L1 detail.

It was also possible to observe the 3D surface roughness distribution using an optical profilometer measuring machine. However, due to the extended time consumption, this machine was only used for one section subjected to analysis. The 3D roughness profile and respective linear roughness profile is illustrated in Figure 5.26. Note that the linear profile in Figure 5.26 was not obtained in the optical surface roughness measuring machine, instead it was obtained from the measurements carried out in the conventional rugosimeter.

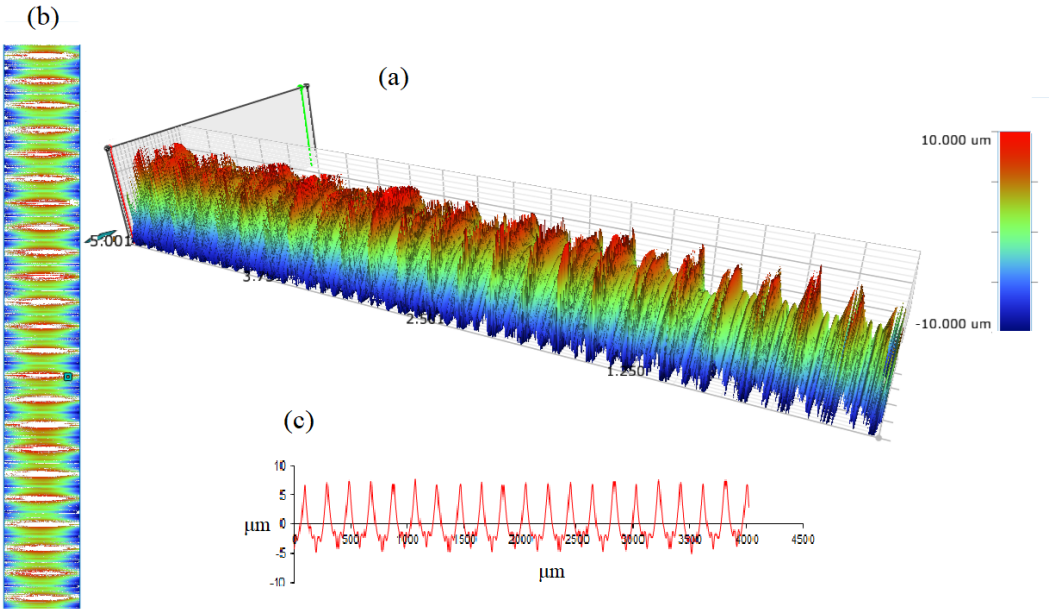

Figure 5.26: Surface roughness profile obtained with an optical profilometer for the AM sample machined with the parameters a_p=0.1 mm and f= 0.2 mm/rev: (a) 3D profile; (b) Surface roughness colour map; (c) Linear roughness profile.

5.2 Milling Tests

The results from the milling tests will be analyzed and, as performed for the turning tests, several aspects will be analyzed, including the influence of the milling parameters in the cutting forces, power consumption and specific cutting pressure, tool wear evaluation, chip geometry and surface quality.

5.2.1 Cutting Forces

Cutting forces analysis in a milling operation requires a more careful analysis than in a turning operation because the forces measured vary with the cutting tool angular position (φ). This effect is shown in Figure 5.27 where the force components present variation with the rotational angle of the milling tool. The plot shown in Figure 5.27 is divided into two different regions, the section in which the cutting insert is in contact with the workpiece, designated tool engagement, and a secondary region, called air cut where the cutting insert does not cut material but, some friction may occur between the workpiece and the cutting insert during this stage. When analyzing Figure 5.27, high load oscillation is observed. Probable cause for such effect is vibration resultant from the lack of stiffness of the setup. Another reason may be the fact that only one cutting insert was used in a 5 slot milling tool, which may result in an unbalanced equipment, which in turn make the setup susceptible to such vibration. Also, the chips produced show a serrated geometry which are favourable to vibration. A scheme of the dynamometer and the respective measured force

components referential is illustrated in Figure 5.28. The F_z force component (parallel to the axis of rotation of the tool), which is a passive force, is not as important in the cutting operation as the F_x and F_y force components, being discarded in the load analysis. Also, a data acquisition sample rate needed to be defined before the milling tests. The sample rate chosen was 5 kHz, however, in a post experimental analysis it proved to be a low sample rate because the number of data points measured were a limiting factor when evaluating higher cutting speeds.

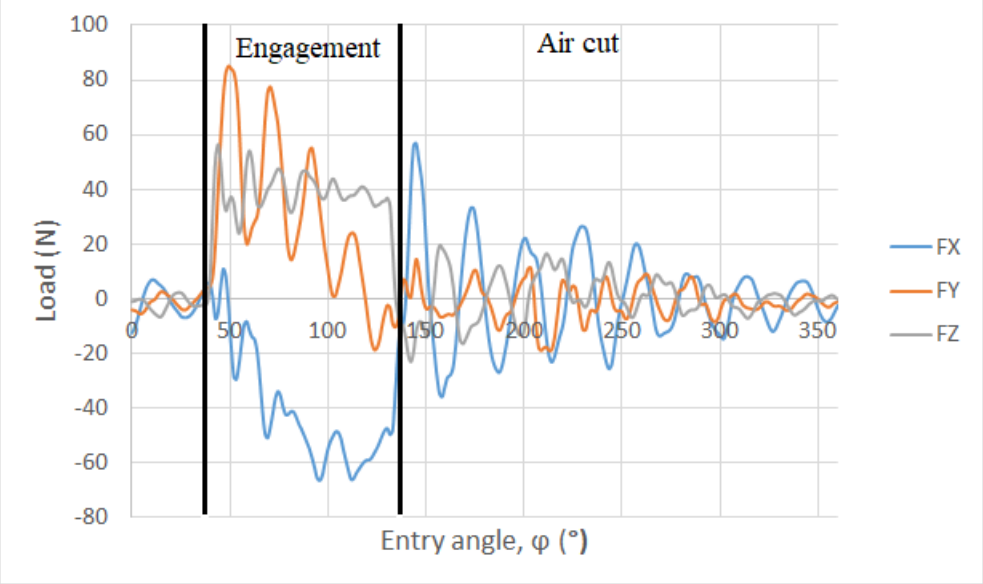

Figure 5.27: Load variation for one rotation of the spindle in the AM sample, for the parameters v_c=80 m/min, a_p= 0.2 mm and f_Z = 0.05 mm/tooth.

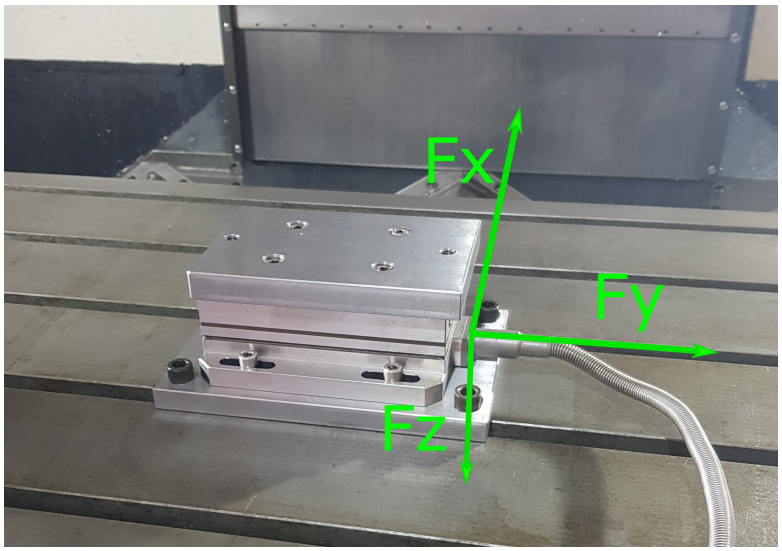

Figure 5.28: Dynamometer fixture in the worktable and respective measured forces referential.

Despite the high load vibration, a cutting force evolution trend can be identified, which seems to go in line with literature [50]. In order to avoid false load peaks derived from vibration, an

analytical model response was adjusted (using the sum of the squared differences method) to each cutting load component (F_x,F_y), enabling further analysis based on those results, namely the experimentally calculated specific cutting pressure and cutting power. With this regard, two distinct approaches regarding load adjustment were taken into consideration. The first method (M1) was identical to the one described in Coelho et al. [50], which does not take into account the specific cutting pressure variation in analytical forces determination during each cutting test. Moreover, it was applied to each individual test, meaning that the identified K_c (calculated through the analytical model explained hereafter) is calculated based on the cutting conditions of that test. This method assumes that the chip thickness (h) varies continuously during the movement of the cutting edge, that is said assumed the approximation $h = f_z \sin\varphi$, however, a more exact relation was used. The description of M1 as well as the equations used is described in the following paragraphs:

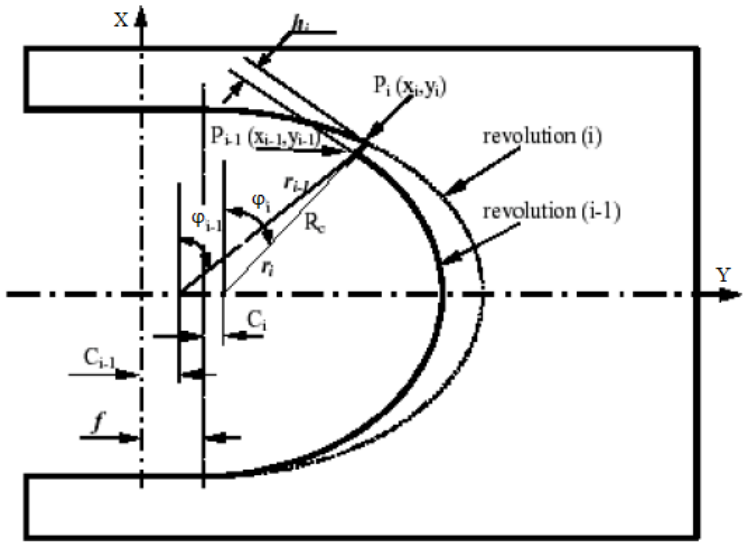

Figure 5.29: Schematic of the movements of the cutting edge on the workpiece for two consecutive turns of the milling tool. Adapted from [50].

According to Figure 5.29, the coordinates of the point $P(x_{i-1}, y_{i-1})$ can be calculated as a function of the center of the milling tool, C_{i-1}, the entry angle φ_{i-1} and the feed per rotation, f.

$$x_{i-1} = R_c \cos\varphi_{i-1} \tag{5.4}$$

$$y_{i-1} = R_c \sin\varphi_{i-1} + (f/2\pi)\varphi_{i-1} \tag{5.5}$$

where R_c is the radius of the milling tool and C_{i-1} is the displacement of the center, which can be calculated by:

$$C_{i-1} = (f/2\pi)\varphi_{i-1} \tag{5.6}$$

When the cutting edge is at the next revolution, the angle is φ_i and center of the milling tool is at the position C_i, the correspondent positional points of the cutting edge $P(x_i, y_i)$ at this revolution (i) are:

$$x_i = R_c \cos \varphi_i \tag{5.7}$$

$$y_i = R_c \sin \varphi_i + (f/2\pi)\varphi_i \tag{5.8}$$

At the angle φ_{i-1}, in Figure 5.29 there is a line, r_{i-1} described by the following equation:

$$r_{i-1} \Rightarrow x_{i-1} = \tan\left(\frac{\pi}{2} - \varphi_{i-1}\right) y_{i-1} - \left(\frac{f\varphi_{i-1}/2\pi)}{\tan \varphi_{i-1}}\right) \tag{5.9}$$

At the angle φ_i, there is also a line r_i described by the following equation:

$$r_i \Rightarrow x_i = \tan\left(\frac{\pi}{2} - \varphi_i\right) y_i - \frac{f(1+\varphi_i/2\pi)}{\tan \varphi_i} \tag{5.10}$$

Considering the generic position illustrated in Figure 5.29 it can be noted that point P_{i-1} belongs to both lines. Considering this condition and combining the equations results in:

$$R_c \cos \varphi_{i-1} - \tan\left(\frac{\pi}{2} - \varphi_i\right)\left[R_c \sin \varphi_{i-1} + \left(\frac{f}{2\pi}\right)\varphi_{i-1}\right] + \frac{f(1+\varphi_i/2\pi)}{\tan \varphi_i} = 0 \tag{5.11}$$

Equation (5.11) cannot be solved by direct methods and numerical methods must be applied. The numerical method adopted in this analysis will be sucessive bisections method, resulting in the solutions of φ_{i-1} as a function of φ_i, which then can be used to calculate both points, P_{i-1} and P_i. The undeformed chip thickness h_i can then be calculated with the coordinates of these points:

$$h_i = \sqrt{(x_i + x_{i-1})^2 - (y_i - y_{i-1})^2} \tag{5.12}$$

The forces acting on the tool insert are composed by two components: the cutting force, F_c, in the direction of the cutting speed and the radial force in the perpendicular direction to the cutting force, F_{cN}. In the model adopted by Coelho et Al. [50] the component F_c is proportional to the undeformed chip thickness and F_{cN} depends on the apparent coefficient of friction (μ) between the chip and the tool's rake face.

$$F_{ci} = K_c w h_i + F_{EC} \tag{5.13}$$

$$F_{cNi} = F_{ci}\mu + F_{ER} \tag{5.14}$$

where K_c is the specific cutting pressure and w the undeformed chip width. The force components F_{ER} and F_{EC} are the residual forces that describe the elastic-plastic deformation of the metal and

depend on the tool radius, at some fixed cutting conditions; these components can be reasonably represented by a constant value and don't change with the variation of the entry angle (φ).

During a milling operation, the cutting edge rotates and the milling tool center shifts between different positions, therefore the directions of the cutting forces are constantly changing. The forces measured by the dynamometer F_x and F_y need to be converted in the cutting directions (collinear with the cutting speed and perpendicular to the latter). In order to make this conversion the following equations were used:

$$F_{xi} = -F_{ci}\sin\varphi_i + F_{cNi}\cos\varphi_i \tag{5.15}$$

$$F_{yi} = F_{ci}\cos\varphi_i + F_{cNi}\sin\varphi_i \tag{5.16}$$

Substituting the equations (3.35) and (3.36) in equations (3.37) and (3.38) results+:

$$F_{xi} = -(K_c w h_i + F_{EC})\sin\varphi_i + (K_c w h_i \mu + F_{EC}\mu + F_{ER})\cos\varphi_i \tag{5.17}$$

$$F_{yi} = (K_c w h_i + F_{EC})\cos\varphi_i + (K_c w h_i \mu + F_{EC}\mu + F_{ER})\sin\varphi_i \tag{5.18}$$

These equations allow a description of the experimental load time histories permitting for a more precise load analysis capturing average trends and filtering vibrations. Through numerical solving methods the coefficient of friction, μ, the specific cutting pressure, K_c and both residual force components F_{EC} and F_{ER} were calculated for each set of cutting parameters. An example of the application of this method for an engagement angle of 100 % (workpiece width higher than the diameter of the cutting tool) is portrayed in Figure 5.30.

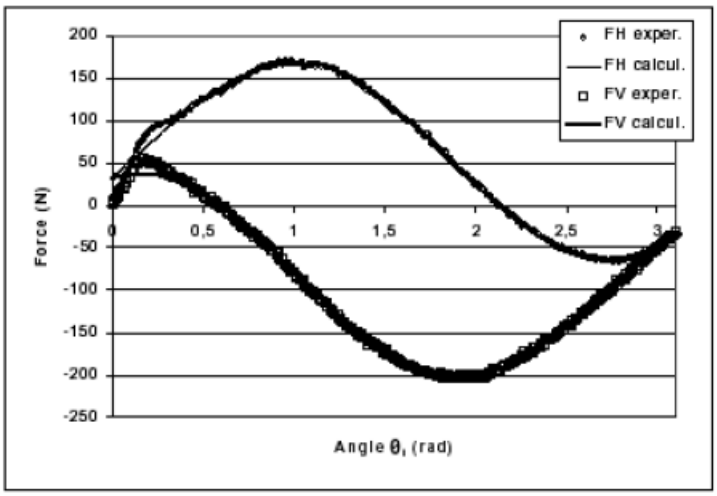

Figure 5.30: Load fitting comparison with the experimental data presented in Coelho et al. [50] for an engagement angle of 100 %.

Given that the undeformed chip section along each milling cutting rotation is variable and the specific cutting pressure depends on the chip geometry, a second method (M2) was employed, which takes into account the actual chip cross-section for each position of the tool insert within the engagement angle. Meaning that in the equations (4.14) and (4.15) K_c is replaced by $K_c(updated)$, where $K_c(updated)$ is calculated as a function of the undeformed chip thickness h_i:

$$K_c(updated) = \frac{1}{h_i^{m_c}} K_{cx} \tag{5.19}$$

$K_c(updated)$ is the updated specific cuting pressure and its a function of h_i, the undeformed chip thickness for a given position of the cutting edge i, m_c an exponent coefficient and K_{cx} the specific cutting pressure for a chip thickness of 1 mm. In this process a unique K_c expression was used for all test data fitting as well as the same friction.

An example of the analytical adjustment using method 1 is shown in Figure 5.31. With the adjusted analytical forces F_x and F_y, the principal cutting force F_c and its normal F_{cN} were calculated for each cutting parameters configuration of the milling tests. The engagement angle in the milling tests was only 99.26º however, as can be seen in Figure 5.30 this model could be applied to a milling operation where the engagement angle was 180º (100%).

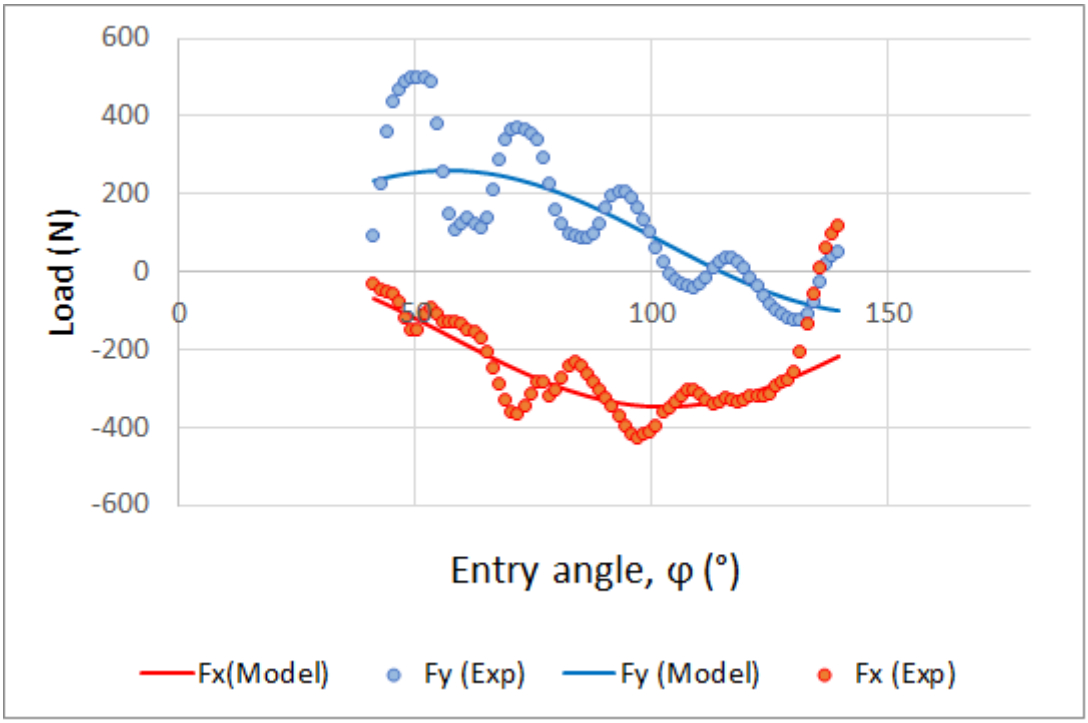

Figure 5.31: Force data adjustment with the numerical model during the engagement for the AM material, v_c = 80 m/min, a_p = 0.6 mm and f_z = 0.2 mm/tooth

For higher cutting speeds (v_c = 240 m/min and v_c = 340 m/min) the sampling rate did not allow the identification of the cutting load evolution pattern. Figure 5.32 illustrates an example of the load variation for an higher cutting speed.

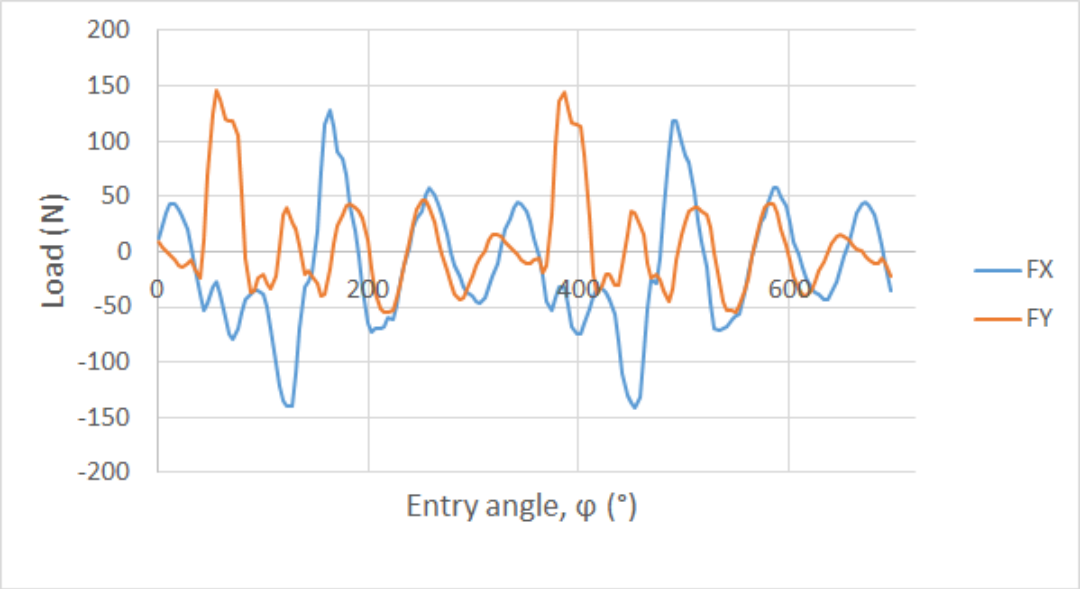

Figure 5.32: Measured load for a cutting speed of 240 m/min in two consecutive tool full rotations, for an a_p= 0.2 mm and f_z=0.1 mm/tooth.

After applying this method (M2) for all combinations of parameters and for the two lowest cutting speeds (V1 and V2), the maximum cutting force (that occurs exactly in the mid- engagement) was calculated as well as the resultant force (of F_c and F_{cN}) in the same position. The obtained results are illustrated in Figure 5.33 and 5.34, respectively.

Analysing the main cutting force, with an increase in either the depth of cut (a_p) or the feed rate (f_z) it increases for both the conventional (CV) and additive (AM) material, reaching the maximum values with the parameters that result in a higher undeformed chip cross-section, in similarity to what occurred in the turning tests. The maximum value obtained was approximately 330 N for both materials and cutting speeds. The influence of the cutting speed in the cutting force is not as relevant as the other milling parameters since for most combinations of parameters the magnitude of the cutting force for both materials is similar, presenting only slight differences in some cases.

Comparing the cutting force in both materials tested, in the majority of the parameters tested the cutting force component values are similar, which allow to conclude that no significant differences between materials exist when regarding this force component.

Comparing the main cutting force with the resultant force it is noticeable that for all the combinations of parameters the cutting force is the main force component due to the fact that the resultant force has a small increase when compared to the cutting force for all combinations of parameters. This difference is maximum for the most severe cutting parameters (a_p = 0.6 mm and f_z = 0.2 mm/tooth), for a cutting speed of 80 m/min and for the CV material the difference is 28.25 N (8.6%) and for the AM material is 32.25 N (9.7%).

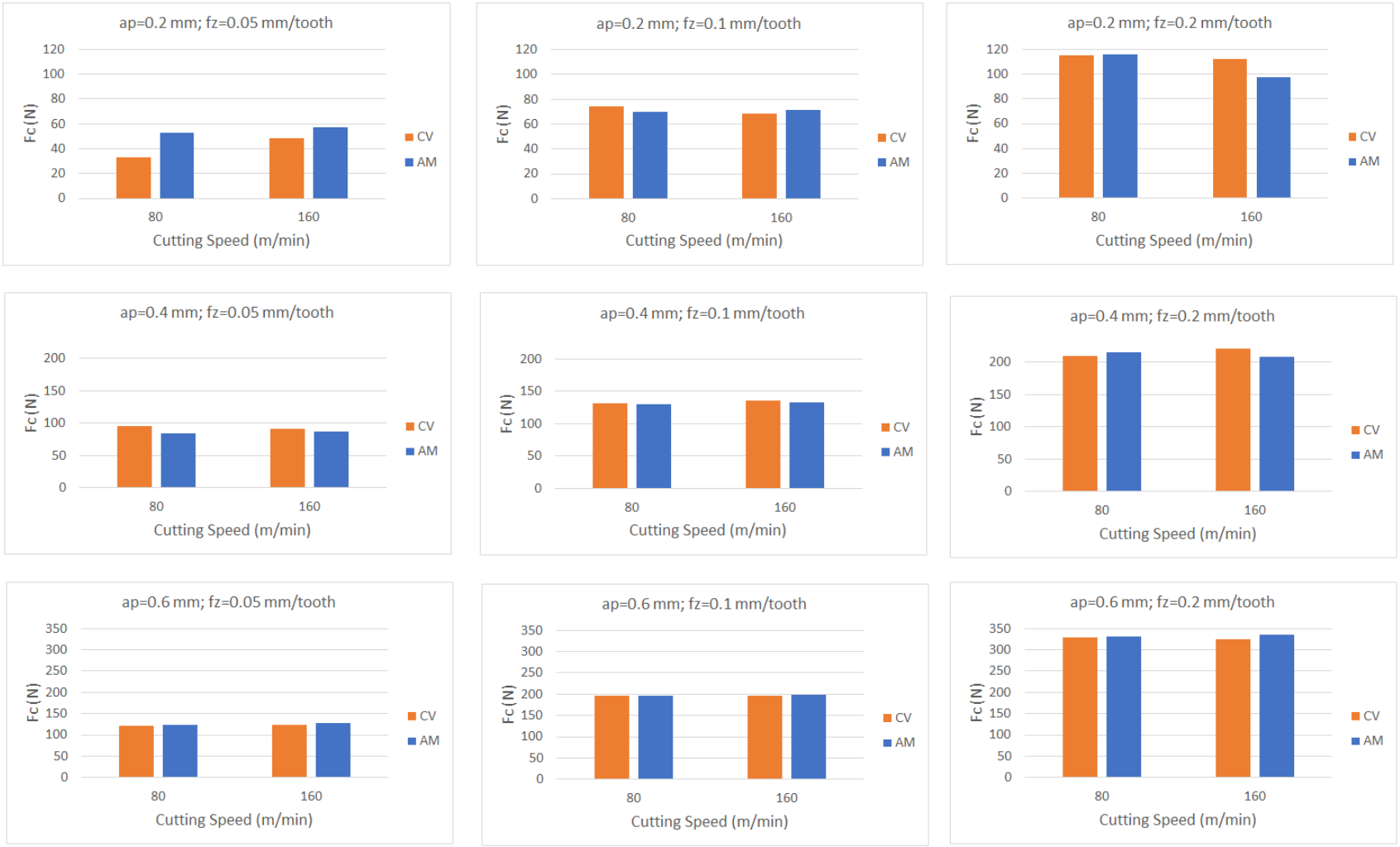

Figure 5.33: Cutting force (F_c) evolution as a function of the milling parameters for both materials (AM and CV).

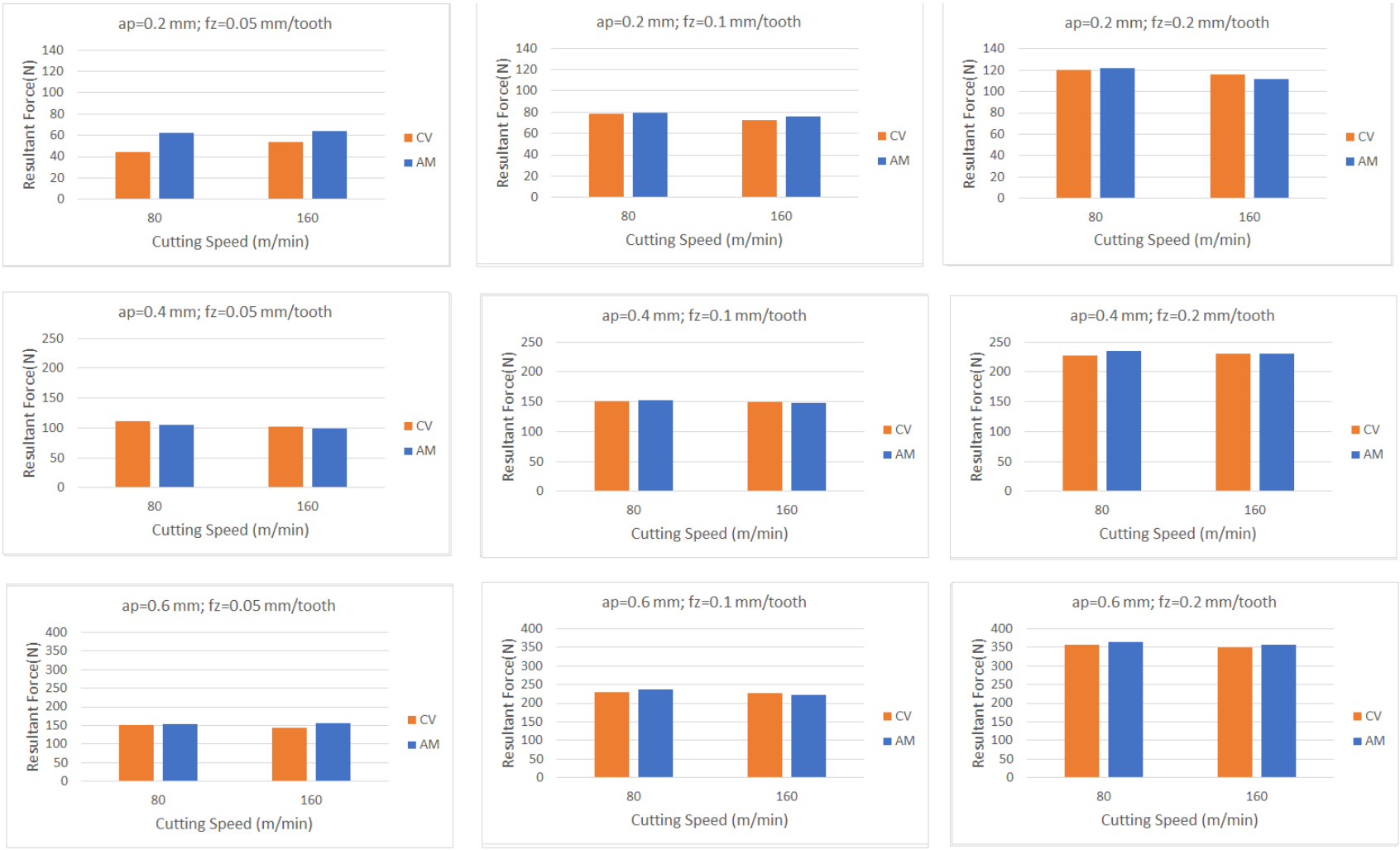

Figure 5.34: Resultant force (F_R) evolution as a function of the milling parameters for both materials (AM and CV).

5.2.2 Cutting Power

Power consumption during the milling operations was calculated as a function of the main cutting force (F_c), the radius of the milling tool (R_C) and the spindle angular frequency (ω).

$$P_c = F_c \cdot R_c \cdot \omega \tag{5.20}$$

Cutting power was analysed as a function of the cutting parameters for both cutting speeds (V1 and V2). Results are shown in Figure 5.35 and 5.36.

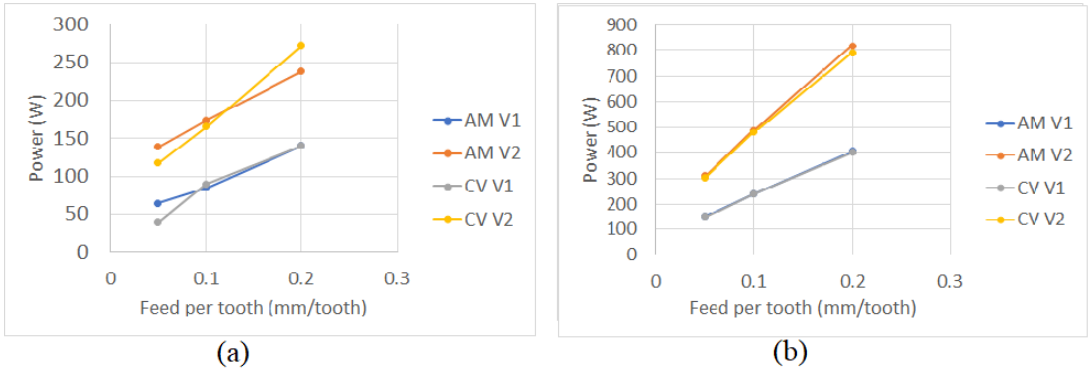

Figure 5.35: Cutting power as a function of the feed per tooth for: (a) a_p = 0.2 mm and (b) a_p = 0.6 mm

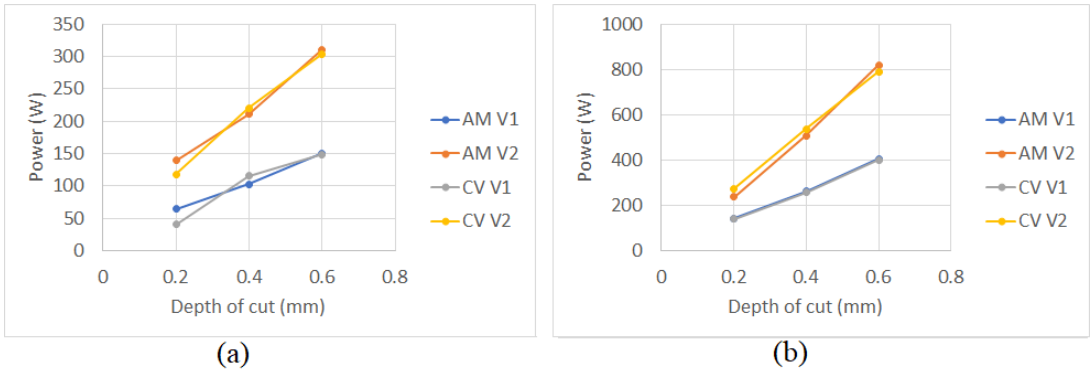

Figure 5.36: Cutting power as a function of the depth of cut for: (a) f_z = 0.05 mm/tooth and (b) f_z = 0.2 mm/tooth

Cutting power presents an almost linear variation with the increase in the feed rate (f_z) and the depth of cut (a_p). Since the power consumption depends on the cutting speed, when this parameter increases the cutting power increases as well. In fact for all the combinations of the parameters with an increase in the cutting speed from V1 = 80 m/min to V2 = 160 m/min the cutting power approximately doubles.

The power consumption for both materials is similar except for the smaller depth of cut (a_p = 0.2 mm) where for a lower feed rate (f_Z = 0.05 mm/tooth) in the highest cutting speed the cutting power for the conventional material is lower than that of the AM material (difference of

approximately 25 W). For the higher feed rate (f_z = 0.2 mm/tooth) this difference is inverted and the power consumption in the conventional material is higher than that of AM (difference of about 45 W).

5.2.3 Specific Cutting Pressure

Specific cutting pressure was inversely identified with methods M1 and M2. For M1 it is possible to display K_c in function of chip section or feed. Method 2 due to being determined based on equation (5.19) where K_c is determined solely as a function of feed-rate, it can only be displayed in function of feed-rate. Figure 5.37 shows the milling specific cutting pressure inversely calculated using the M1 method as described in Coelho et al. [50].

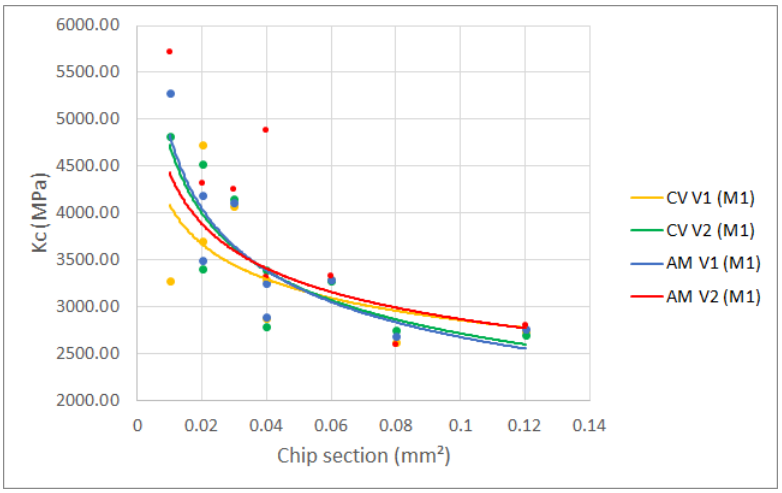

Figure 5.37: Specific cutting pressure calculated through Method 1 (M1).

In Figure 5.38 and 5.39 the milling specific cutting pressure is displayed as a function of undeformed chip thickness, based on the second approach (M2) and compared with the K_c determined by M1.

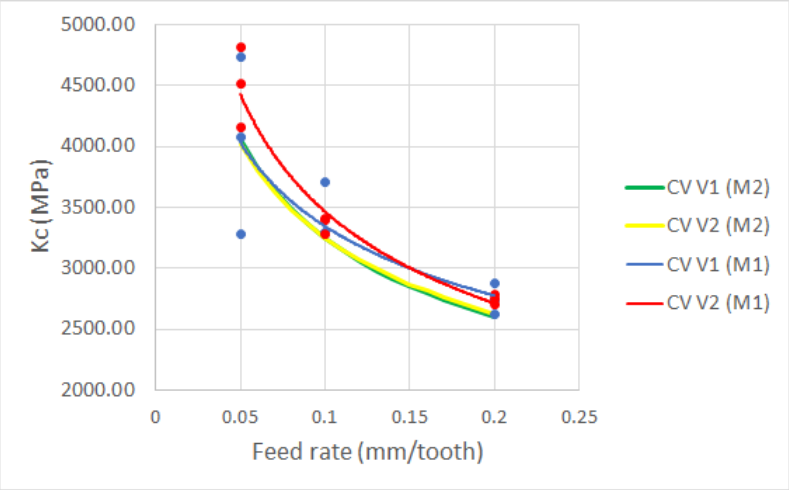

Figure 5.38: Specific cutting pressure as a function of the feed rate calculated through both methods, for the conventional material.

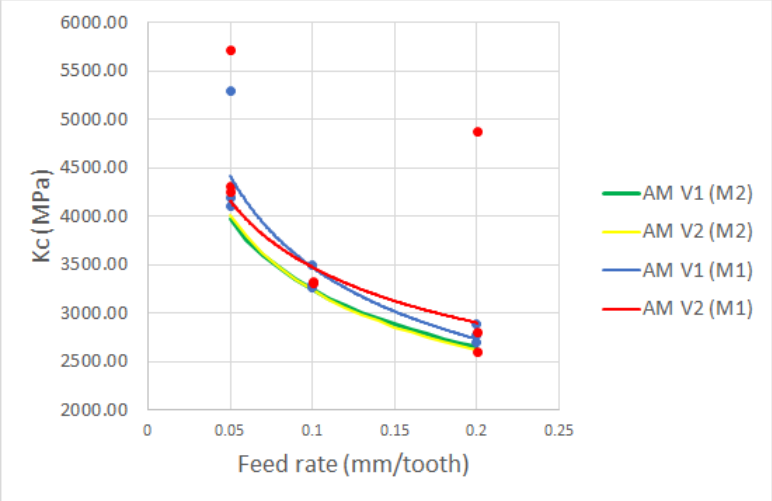

Figure 5.39: Specific cutting pressure as a function of the feed rate calculated through both methods, for the AM material.

When analyzing Figure 5.38 and 5.39, M2 method has lower values of K_c when compared to M1 for most of the chip thicknesses. This method is a more rigorous approach to the problem of the specific cutting pressure calculation, since it takes into account the variability of the chip thickness throughout all the engagement stage, therefore it can be considered a good alternative to the method proposed by Coelho et Al. [50]. When using the second method, no significant difference between cutting speeds is noticed, which may be linked to the fact that the specific cutting pressure function was inversely determined based on data that included both V1 (80 m/min) and V2 (160 m/min) speed. Using M1 slight differences appear with the change of cutting speed however, these discrepancies are not very significant. In Figure 5.39 (relative to the AM material) it is possible to see that scatter is higher than in Figure 5.38, which may be due to the also higher

load scatter in the metal cutting of additively manufactured specimens. Since it is more prone to defects such as porosity, loads may have an higher vibration.

In order to validate the specific cutting pressure results obtained in the milling tests, a comparison has been made with the already mentioned turning test results. This comparison is depicted in Figure 5.40. For this comparison, method number two was used. For simplicity purposes, only one cutting speed was selected for each test, being the turning tests labelled as CV_T and AM_T and the milling tests CV_M and AM_T.

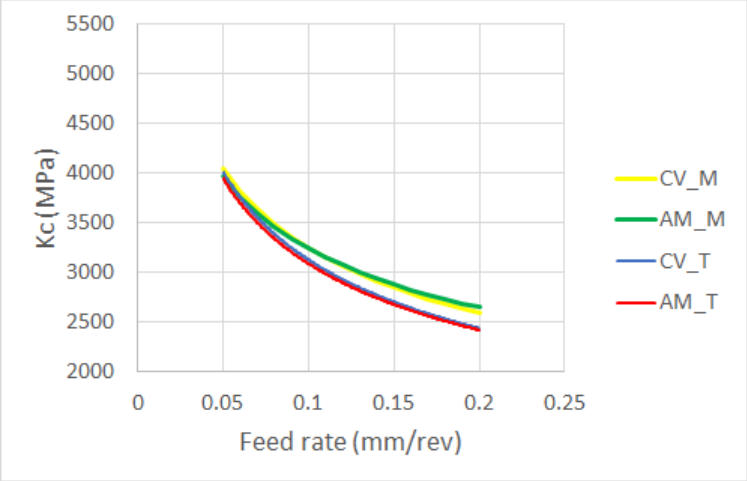

Figure 5.40: Specific cutting pressure comparison between the milling and turning tests.

Similar values were obtained for the specific cutting pressure calculated in the turning and milling tests using method number two, especially for smaller undeformed chip thicknesses. For higher feed rates, the results are more divergent, however only slight differences exist. The seen differences can be related to the fact that orthogonal conditions were not ensured in milling operations. The differences in tool geometry between turning and milling can be pointed as a plausible reason for the slight discrepancy.

5.2.4 Chip Morphology

The chips obtained in the milling tests are all short chips in contrast with the turning tests, because of the interrupted cut present in this process. Due to the time consuming and cumbersome logistic process of chip collection, during the milling tests chip collection was only done for the combinations of parameters present in Table 5.5 and not for all the tests carried out. Note that these parameters were repeated for each cutting speed, but only cutting speeds V1 and V2 were analyzed.

Table 5.5: Chips collection for milling tests overview.

Cutting speed (v_c)	a_p **(mm)**	f_z **(mm/tooth)**
V1	0.2	0.05
V1	0.2	0.2
V1	0.6	0.05
V1	0.6	0.02
V2	0.2	0.05
V2	0.2	0.2
V2	0.6	0.05
V2	0.6	0.02

In Figures 5.41 to 5.44 it is possible to observe the SEM images of some of the chips collected. Note that in all cases two very distinct surfaces are present, a smoother surface that represents the face of the chip that was in contact with the cutting tool (submitted to high pressure and sliding friction) and a more irregular surface which represents the opposite face (coined by the intense plastic deformation). The irregular surface texture present in the face opposite to the cutting tool is related to the presence of adiabatic shear bands (ASB) that result from the high rate of deformation the workpiece material is subjected to.

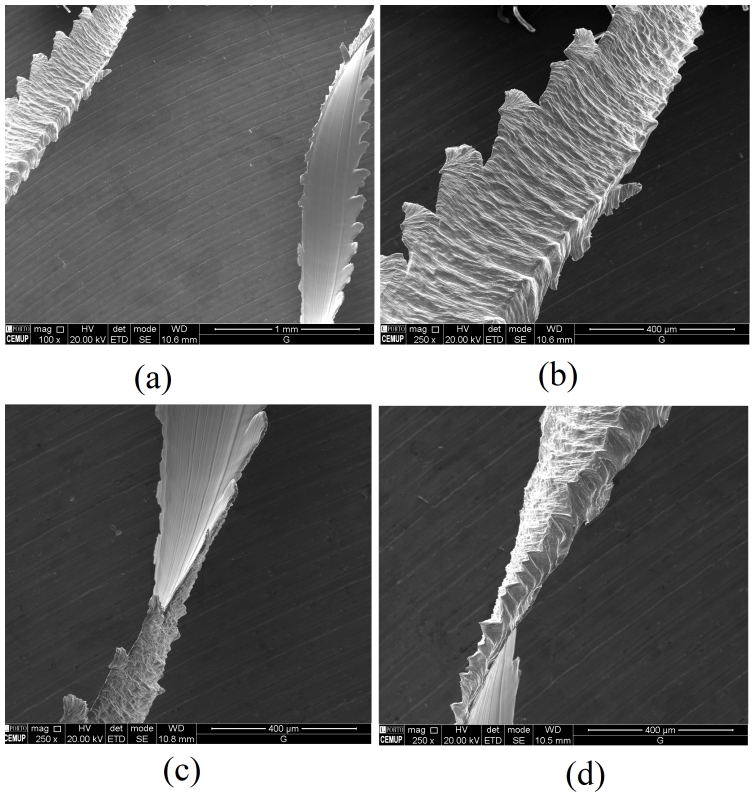

Figure 5.41: SEM images obtained from the milling tests of the conventional (CV) material, v_c = 160 m/min, a_p = 0.2 mm, f_z = 0.05 mm/tooth

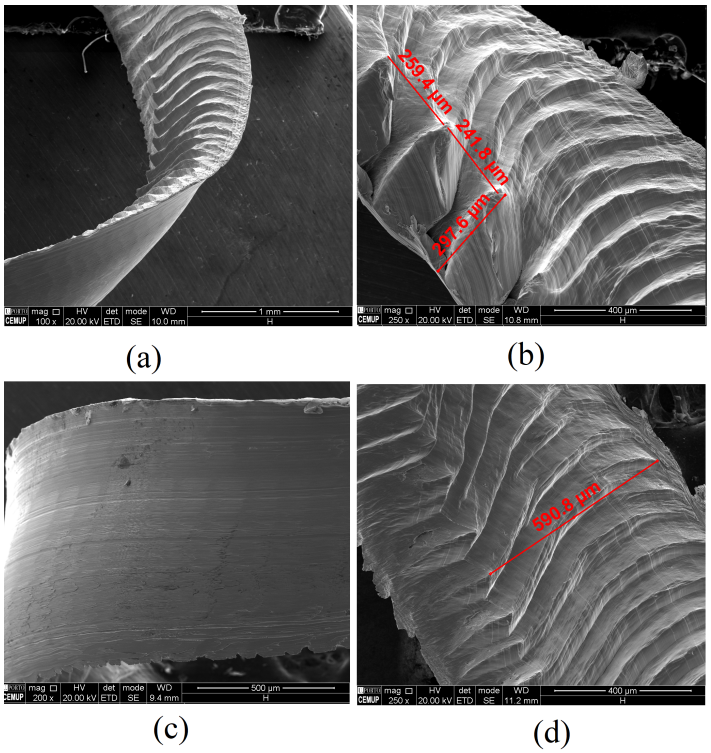

Figure 5.42: SEM images obtained from the milling tests of the conventional (CV) material, v_c = 160 m/min, a_p = 0.6 mm, f_z = 0.2 mm/tooth

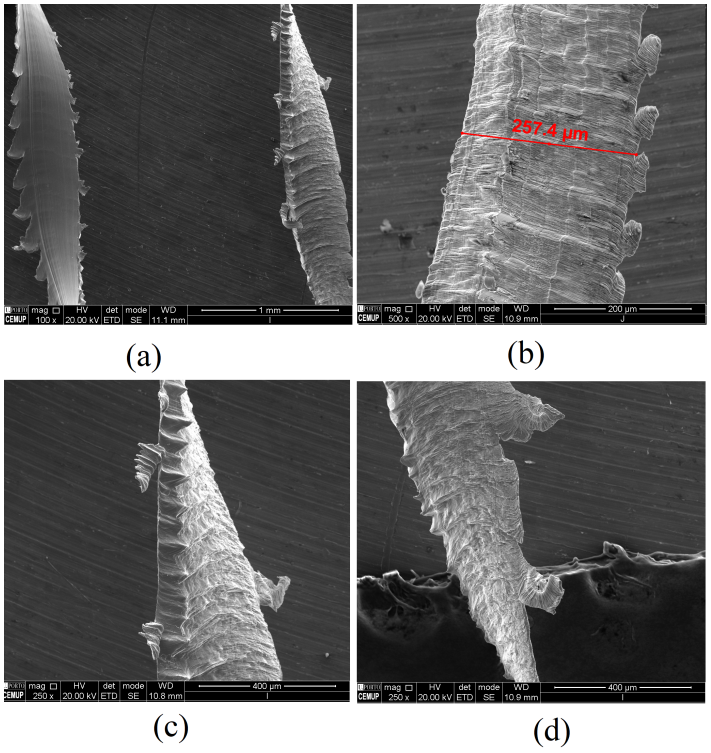

Figure 5.43: SEM images obtained from the milling tests of the AM material, v_c = 160 m/min, a_p = 0.2 mm, f_z = 0.05 mm/tooth

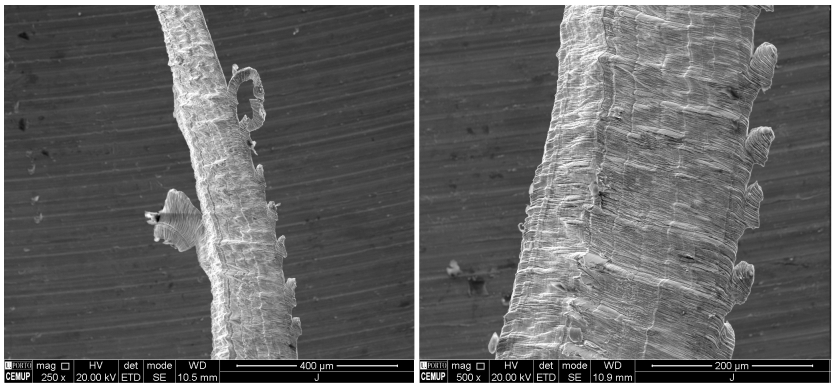

Figure 5.44: SEM images obtained from the milling tests of the AM material, v_c = 160 m/min, a_p = 0.6 mm, f_z = 0.2 mm/tooth

5.2.5 Tool Wear

Tool wear was inspected through optical microscopy and SEM images. Figure 5.45 shows the geometry of the unused cutting insert. The images for the tools used in the machining of both materials, for two distinct cutting speeds, are illustrated in Figure 5.46 to 5.49. The damage found through microscopical observation of the inserts is mostly superficial, where small portions of the coating were removed. In all the inserts, small portions of the workpiece material were found in the cutting edge which resulted from the adhesion of the workpiece material during the cutting stage.

Figure 5.45: XPET PDER-LP Milling insert: (a) rake face view; (b) clearance face view.

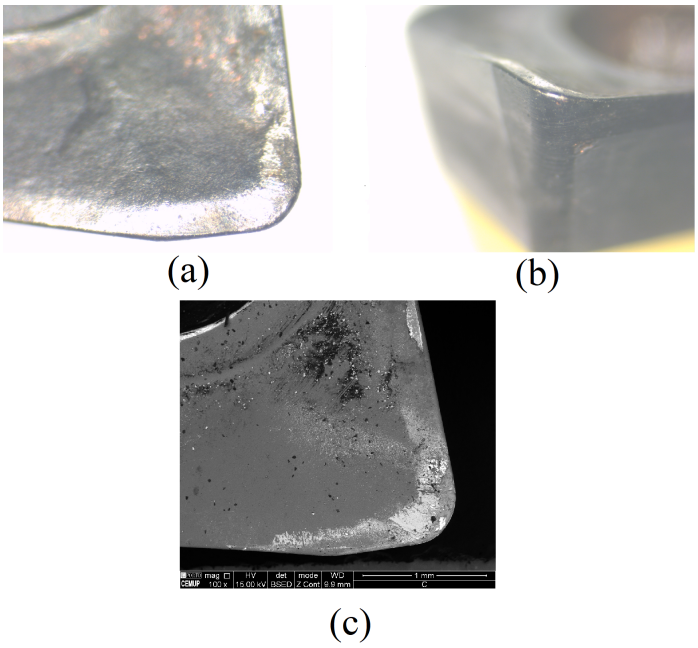

Figure 5.46: Cutting insert used in the milling tests for machining of the conventional specimen for a cutting speed of v_c = 80 m/min: (a) and (b) optical images of the rake and clearance face, respectively; (c) SEM image of the cutting edge.

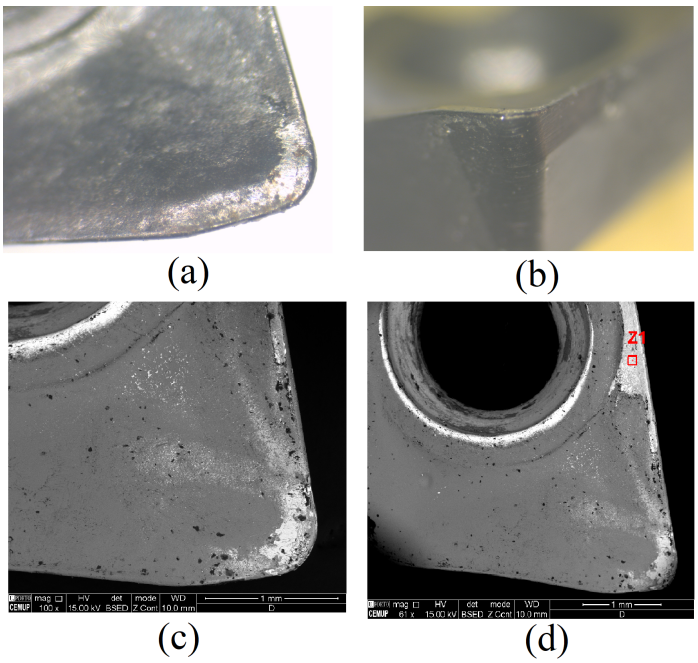

Figure 5.47: Cutting insert used in the milling tests for machining of the AM specimen for a cutting speed of v_c = 80 m/min: (a) and (b) optical images of the rake and clearance face, respectively; (c) and (d) SEM image of the cutting edge.

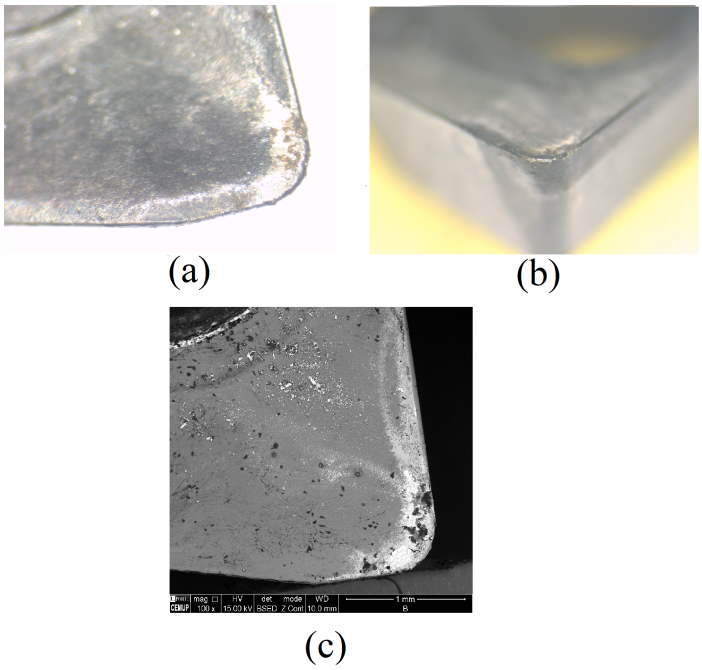

Figure 5.48: Cutting insert used in the milling tests for machining of the conventional specimen for a cutting speed of v_c = 160 m/min: (a) and (b) optical images of the rake and clearance face, respectively; (c) SEM image of the cutting edge.

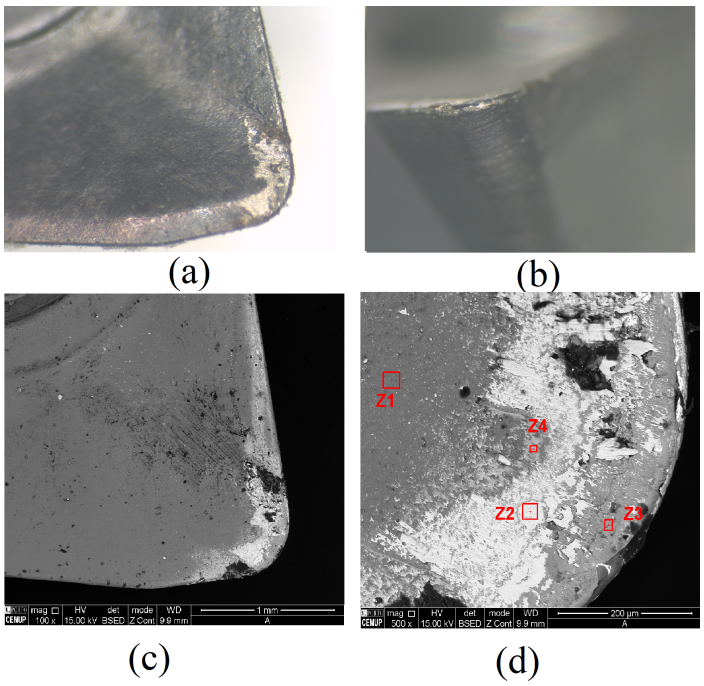

Figure 5.49: Cutting insert used in the milling tests for machining of the AM specimen for a cutting speed of v_c = 160 m/min: (a) and (b) optical images of the rake and clearance face, respectively; (c) and (d) SEM image of the cutting edge.

In Figure 5.47 the light grey zone (Z1) was chemically analysed in order to understand what type of material was present. It was concluded that the material was tungsten carbide (WC), the substrate material of the cutting insert and small portions of the coating material (AlTiN) were present as well. This area is quite distanced from the cutting edge, which may indicate that this damage is caused by the chip flow and not the actual wear from the cutting operation itself. A more detailed chemical analysis of the cutting edge was carried out for the cutting insert used in the machining of the AM specimen. In Figure 5.49 four distinct zones were identified: Z1 corresponds to the coating material AlTiN, Z2 to the 18Ni300 maraging steel (workpiece material), Z3 a mixture of the coating and workpiece material and Z4 Fe_2O_3 (Iron Oxide). Table 5.6 shows the most abundant chemical elements for each zone.

Table 5.6: Most abundant chemical components found in each zone.

Zone	**Most abundant elements**
Z1	Al, Ti, N
Z2	Fe, Ni, Co, Mo, Ti
Z3	Ti, O, Al, Fe
Z4	O, Fe, Ti

5.2.6 Surface Quality

Table 5.7 shows the last cutting parameters used in each specimen as well as the surface roughness values measured. Additionally to the two cutting speeds evaluated in other sections, two higher cutting speeds were also analyzed.

Table 5.7: Surface roughness measurements for the milling samples.

				Ra (μm)		**Rz** (μm)	
Section	v_c **(m/min)**	a_p **(mm)**	f_z **(mm/t)**	**CV**	**AM**	**CV**	**AM**
L1	80	0.6	0.2	0.310	0.740	1.847	3.960
L2	160	0.6	0.2	0.483	0.530	2.493	3.960
L3	240	0.6	0.2	0.450	0.307	2.630	1.913
L4	320	0.6	0.2	0.400	0.887	2.663	5.780

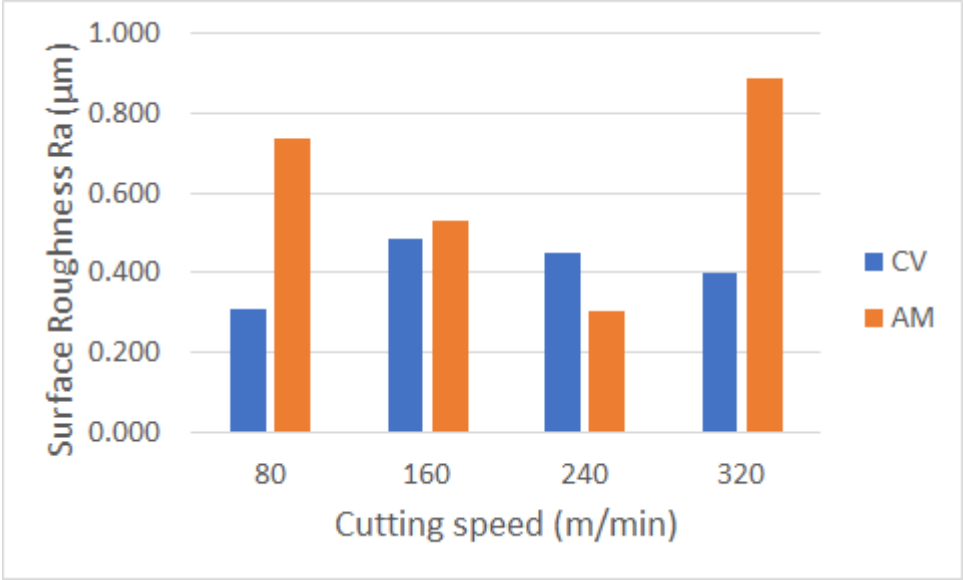

Figure 5.50: Surface roughness comparison between both materials for all the cutting speeds

For most cases, the surface roughness is higher in the AM specimen than the conventional specimen. One of the causes might be that AM specimens are prone to the existence of defects than the conventionally produced ones, which may lead to a poorer surface quality. Nonetheless, surface roughness consistently ranged below $R_a = 0.8\mu m$, which corresponds to a very significant improvement when comparing with as-built surface roughness. However, since the feed rate is the most influential parameter regarding surface quality, no clear conclusions can be drawn from the analysis of surface roughness of the milling samples.

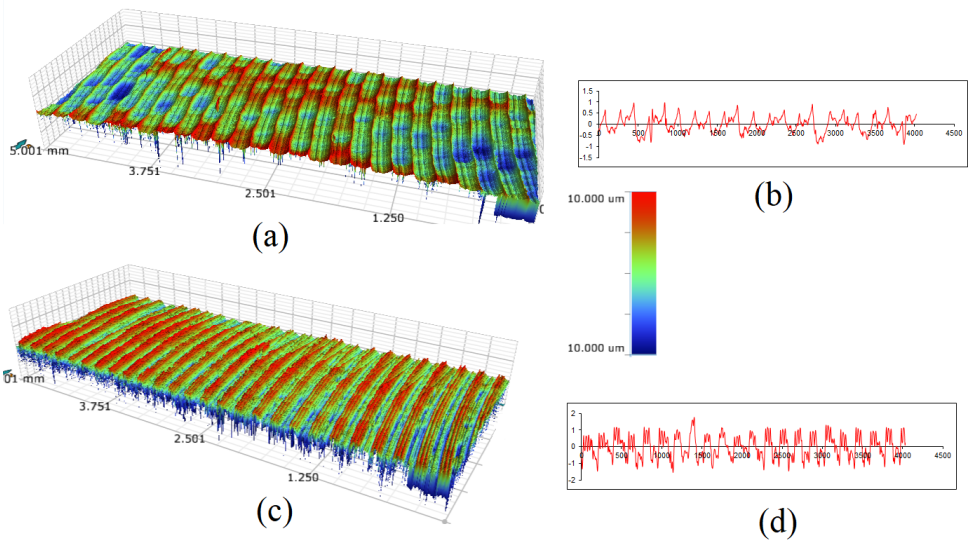

Figure 5.51: Surface roughness profile obtained with an optical profilometer for the conventional sample for distinct cutting speeds (a) and (b) v_c = 80 m/min; (c) and (d) v_c = 160 m/min.

Figure 5.51 depicts the 3D profile of two distinct surfaces, being the difference between surfaces the cutting speeds each was subjected to. Analyzing Figure 5.51 it is possible to observe the influence of the cutting speed in the surface topology. With an increased cutting speed the surface topology is more irregular, one of the causes for this effect might be the vibration occurrence when the cutting speed is increased.

Chapter 6

Conclusions and Future Work

6.1 Conclusions

The proposed objectives for this dissertation were accomplished and allowed to draw conclusions regarding the machinability of the 18Ni300 maraging steels and the comparison between additivelly and conventionally manufactured materials.

- Additivelly manufactured samples presented an higher flow stress than the conventional material in the quasi-static compression tests.
- Regarding the cutting forces, all components are highly dependent on the depth of cut and feed rate, and increase with the increment of these parameters, since it corresponds to an increase in the chip section.
- In milling and turning, the cutting force component is the most influential regarding the maximum resultant load.
- The influence of the cutting speed in the main cutting force was not very noticeable, minor changes appear when increasing the cutting speed, which allows the conclusion that this parameter does not have as much influence as the depth of cut and feed rate, for the tested cutting speeds range.
- The turning insert without a chip breaker (DCMW) presented higher main cutting force for all sets of cutting parameters.
- Cutting power presents an approximately linear relation to the cutting parameters (depth of cut and feed rate), similarly to the main cutting force. The DCMW turning insert also presented higher power consumption, as expected.
- Even though additively manufactured 18Ni300 maraging steel showed higher flow stress than the conventional counterpart, no additional power requirement was noticed nor a marked difference in specific cutting pressure identified.

- Specific cutting pressure did not present significant distinction among the tested materials (AM and conventional) despite the distinct flow stresses of the materials. Tool geometry plays, however, a significant role in the specific cutting pressure, being higher for tools without chip-breaking grooves.
- Most of the chips obtained in the turning tests are long or snarled chips, classified as unfavorable, whereas in the milling tests all the combinations of parameters led to short chip due to the interrupted cut nature of this operation.
- In turning operations, the feed rate is the most influential parameter regarding chip geometries since when increasing the feed rate from minimum to maximum for almost every case it changes the chip form.
- An increase in the feed rate could lead to more favorable chip geometries when using the tool with a chip-breaker (DCGT).
- Tool wear was more noticeable in the conventional material than the AM material and was more noticeable in the turning tests due to a longer machining length.
- Despite being distinct metal cutting operations, the estimated specific cutting pressure presents similar trend and values between turning an milling.
- Vibratory process was verified during milling which may be attributed to vibrations of the setup or formation of serrated chips.

6.2 Future Work

- To perform instrumented machining tests for roughing operations, higher feed rates, depths of cut and cutting speeds.
- Machinability studies of 18Ni300 for drilling and orthogonal cutting operations.
- Different cutting conditions for milling and turning tests, namely the usage of a cutting fluid.
- Usage of more cutting inserts in the milling tests and establish a comparison with the experimental results of this thesis.
- In the milling tests, performing the same tests but with an engagement angle of 180º where the milling tool is smaller than the width of the workpiece in conditions of orthogonal milling.
- Use and higher sampling rate than the one used in these experimental tests, for the same conditions.
- In order to reduce vibration noise in the load acquisition, use a stiffer fixture system for dynamometer+workpiece.

- Assemble the dynamometer in turret of the milling machine and perform the same operations and establish a comparison between results.
- Perform numerical simulations for both metal cutting processes and compare the results with the experimental data.

References

[1] Simon Ford and Mélanie Despeisse. Additive manufacturing and sustainability: an exploratory study of the advantages and challenges. *Journal of Cleaner Production*, 137:1573 – 1587, 2016.

[2] 3d printing engineering- 3d print, scan, cad, consultancy services. https://3d-printing-engineering.com/am-vs-traditional-manufacturing/. (Accessed on 02/28/2020).

[3] Hadley Brooks and Kevin Brigden. Design of conformal cooling layers with self-supporting lattices for additively manufactured tooling. *Additive Manufacturing*, 11:16 – 22, 2016.

[4] What is rapid prototyping? | definition and best practices. https://www.productplan.com/glossary/rapid-prototyping/. (Accessed on 02/28/2020).

[5] Ian Gibson, David W Rosen, Brent Stucker, et al. *Additive manufacturing technologies*, volume 17. Springer, 2014.

[6] Danielle Strong, Michael Kay, Brett Conner, Thomas Wakefield, and Guha Manogharan. Hybrid manufacturing – integrating traditional manufacturers with additive manufacturing (am) supply chain. *Additive Manufacturing*, 21:159 – 173, 2018.

[7] Mohsen Attaran. The rise of 3-d printing: The advantages of additive manufacturing over traditional manufacturing. *Business Horizons*, 60(5):677 – 688, 2017.

[8] ISO/ASTM 52900:2015. additive manufacturing — general principles — terminology. URL: https://www.iso.org/obp/ui/#iso:std:iso-astm:52900:ed-1:v1:en.

[9] Powder bed fusion | additive manufacturing research group | loughborough university. https://www.lboro.ac.uk/research/amrg/about/the7categoriesofadditivemanufacturing/powderbedfusion/. (Accessed on 11/19/2019).

[10] William E. Frazier. Metal additive manufacturing: A review. *Journal of Materials Engineering and Performance*, 23(6):1917–1928, Jun 2014.

[11] Nesma Aboulkhair, Nicola Everitt, Ian Ashcroft, and Christopher Tuck. Reducing porosity in alsi10mg parts processed by selective laser melting. *Additive Manufacturing*, 1-4, 08 2014.

[12] Dario Pitassi, Enrico Savoia, Vigilio Fontanari, Alberto Molinari, Valerio Luchin, Gianluca Zappini, and Matteo Benedetti. Finite element thermal analysis of metal parts additively manufactured via selective laser melting. *Finite Element Method-Simulation, Numerical Analysis and Solution Techniques*, 2018.

[13] Bi Zhang, Yongtao Li, and Qian Bai. Defect formation mechanisms in selective laser melting: A review. *Chinese Journal of Mechanical Engineering*, 30(3):515–527, May 2017.

[14] Jing CHEN, Wei HOU, Xiuzhuan WANG, Songlin CHU, and Zhiyi YANG. Microstructure, porosity and mechanical properties of selective laser melted alsi10mg. *Chinese Journal of Aeronautics*, 2019.

[15] Xin Zhou, Xihe Liu, Dandan Zhang, Zhijian Shen, and Wei Liu. Balling phenomena in selective laser melted tungsten. *Journal of Materials Processing Technology*, 222:33 – 42, 2015.

[16] Chor Yen Yap, C. Chua, Z. Dong, Z. Liu, D. Zhang, L.E. Loh, and Swee Leong Sing. Review of selective laser melting: Materials and applications. *Applied Physics Reviews*, 2:041101, 12 2015.

[17] Available materials for metal additive manufacturing: Characteristics & applications | farinia group. https://www.farinia.com/additive-manufacturing/3d-materials/characteristics-and-applications-of-available-metals-for-additive-manufacturing. (Accessed on 12/10/2019).

[18] T. DebRoy, H.L. Wei, J.S. Zuback, T. Mukherjee, J.W. Elmer, J.O. Milewski, A.M. Beese, A. Wilson-Heid, A. De, and W. Zhang. Additive manufacturing of metallic components – process, structure and properties. *Progress in Materials Science*, 92:112 – 224, 2018.

[19] Wei Sha and Zhanli Guo. Maraging steels. Woodhead Publishing Series in Metals and Surface Engineering. Woodhead Publishing, 2009.

[20] Pinto Soares. *Aços- características e tratamentos*. Publindústria, 2010.

[21] Eric A Jägle, Zhendong Sheng, Philipp Kürnsteiner, Sörn Ocylok, Andreas Weisheit, and Dierk Raabe. Comparison of maraging steel micro-and nanostructure produced conventionally and by laser additive manufacturing. *Materials*, 10(1):8, 2017.

[22] Naoki Takata, Ryoya Nishida, Asuka Suzki, Makoto Kobashi, and Masaki Kato. Crystallographic features of microstructure in maraging steel fabricated by selective laser melting. *Metals*, 8:440, 06 2018.

[23] Naoki Takata, Ryoya Nishida, Asuka Suzuki, Makoto Kobashi, and Masaki Kato. Crystallographic features of microstructure in maraging steel fabricated by selective laser melting. *Metals*, 8(6):440, 2018.

[24] Metal powders – the raw materials. https://www.metal-am.com/introduction-to-metal-additive-manufacturing-and-3d-printing/metal-powders-the-raw-materials/. (Accessed on 11/26/2019).

[25] Maraging steel: Unique properties and uses | engineeringclicks. https://www.engineeringclicks.com/maraging-steel/. (Accessed on 11/26/2019).

[26] Comparison between additive manufacturing and wrought part realized with maraging steel., insights. https://www.tec-eurolab.com/eu-en/comparison-between-additive-manufacturing-and-wrought-part-realized-with-maraging-steel.aspx. (Accessed on 02/04/2020).

[27] Wei Du, Qian Bai, and Bi Zhang. A novel method for additive/subtractive hybrid manufacturing of metallic parts. *Procedia Manufacturing*, 5:1018 – 1030, 2016.

[28] M.P. Groover. *Fundamentals of Modern Manufacturing: Materials, Processes, and Systems*. John Wiley & Sons, 2010.

[29] Thomas Childs, Katsuhiro Maekawa, Toshiyuki Obikawa, and Yasuo Yamane. Metal machining: Theory and applications. Butterworth-Heinemann, Oxford, 2000.

[30] P.N. Rao. *Manufacturing Technology—Metal Cutting and Machine Tools, 4e (Volume II)*. McGraw-Hill Education, 2018.

[31] www.examhill.com. http://www.examhill.com/shear-angle/. (Accessed on 11/28/2019).

[32] Y Author Altintas and AA Reviewer Ber. Manufacturing Automation: Metal Cutting Mechanics, Machine Tool Vibrations, and CNC Design. *Applied Mechanics Reviews*, 54(5), 09 2001.

[33] ISO 3685:1993. tool-life testing with single-point turning tools URL: https://www.iso.org/standard/9151.html.

[34] F Klocke. Manufacturing Processes I, Cutting, RWTH series. *Springer Verlag*, 504:7, 2011.

[35] Mitsubishi catalogue c008b - technical data. http://www.mitsubishicarbide.com/application/files/6915/1668/5748/catalog_c008b_technical_data.pdf. (Accessed on 6/12/2019).

[36] Rudy Helmons. *Excavation of Hard Deposits and Rocks, on the Cutting of Saturated Rock*. PhD thesis, 05 2017.

[37] Hans Kurt Toenshoff. *Cutting, Fundamentals*, pages 345–357. Springer Berlin Heidelberg, Berlin, Heidelberg, 2014.

[38] K.H. Grote and E.K. Antonsson. *Springer Handbook of Mechanical Engineering*. Number vol. 10 in 2009 Springer E-Books. Springer, 2009.

[39] Alessandro Fortunato, Amarildo Lulaj, Shreyes Melkote, Erica Liverani, Alessandro Ascari, and Domenico Umbrello. Milling of maraging steel components produced by selective laser melting. *The International Journal of Advanced Manufacturing Technology*, 94(5):1895–1902, Feb 2018.

[40] Samuel Milton, Antoine Morandeau, Florent Chalon, and Rene Leroy. Influence of Finish Machining on the Surface Integrity of Ti6Al4V Produced by Selective Laser Melting. *Procedia CIRP*, 45:127 – 130, 2016.

[41] Ashwin Polishetty, Manikanda Shunmugavel, Moshe Goldberg, Guy Littlefair, and Raj Kumar Singh. Cutting Force and Surface Finish Analysis of Machining Additive Manufactured Titanium Alloy Ti-6Al-4V. *Procedia Manufacturing*, 7:284 – 289, 2017.

[42] A. A. Couto. Machinability studies of conventional and AM 18Ni300 maraging steels. MSc. Thesis, FEUP, 2019.

[43] Data sheet: Maraging steel M300 for 200 W powder for additive manufacturing: additive manufacturing laser powder bed fusion. https://resources.renishaw.com/en/details/data-sheet-maraging-steel-m300-for-200-w-powder-for-additive-manufacturing--96325. (Accessed on 12/11/2019).

[44] Chaolin Tan, Kesong Zhou, Xin Tong, Yushan Huang, Jing Li, Wenyou Ma, Fuhai Li, and Tongchun Kuang. Microstructure and mechanical properties of 18ni-300 maraging steel fabricated by selective laser melting. In *2016 6th International Conference on Advanced Design and Manufacturing Engineering (ICADME 2016)*. Atlantis Press, 2017.

[45] Todd M. Mower and Michael J. Long. Mechanical behavior of additive manufactured, powder-bed laser-fused materials. *Materials Science and Engineering: A*, 651:198 – 213, 2016.

[46] Data sheet, type 9129a... http://web.sensor-ic.com:8000/ZLXIAZAI/KISTLER/000-710e-04.11.pdf. (Accessed on 01/22/2020).

[47] A. C. L. Amaral. Machinability studies of conventional and additively manufactured stainless steel 316L. MSc. Thesis, FEUP, 2019.

[48] Catálogo palbit imperial. https://www.palbit.pt/pt/downloads.803/ferramentas-de-corte.932/catalogos.936/catalogoimperial.a5639.html. (Accessed on 03/03/2020).

[49] D.I. Lalwani, N.K. Mehta, and P.K. Jain. Experimental investigations of cutting parameters influence on cutting forces and surface roughness in finish hard turning of MDN250 steel. *Journal of Materials Processing Technology*, 206(1):167 – 179, 2008.

[50] R.T. Coelho, A. Braghini Jr, C.M.O. Valente, and G.C. Medalha. Experimental evaluation of cutting force parameters applying mechanistic model in orthogonal milling. *Journal of the Brazilian Society of Mechanical Sciences and Engineering*, 25(3):247–253, 2003.

Appendix A

Codes and parameters for the turning experiments

Table A.1: Operation codes adopted for each combination of parameters in the turning tests.

d (mm)	n (rpm)	v_c (m/min)	Section	Tool	a_p (mm)	f (mm/rev)	Operation Code
20	1432	90	L1	T1	0.3	0.05	T1V2a3f3
19.4	1477	90	L1	T1	0.3	0.1	T1V2a3f2
18.8	1524	90	L1	T1	0.3	0.2	T1V2a3f1
18.2	1574	90	L1	T1	0.2	0.05	T1V2a2f3
17.8	1609	90	L1	T1	0.2	0.1	T1V2a2f2
17.4	1646	90	L1	T1	0.2	0.2	T1V2a2f1
17	1685	90	L1	T1	0.1	0.05	T1V2a1f3
16.8	1705	90	L1	T1	0.1	0.1	T1V2a1f2
16.6	1726	90	L1	T1	0.1	0.2	T1V2a1f1
16.4	1165	60	L1	T1	0.3	0.05	T1V1a3f3
15.8	1209	60	L1	T1	0.3	0.1	T1V1a3f2
15.2	1256	60	L1	T1	0.3	0.2	T1V1a3f1
14.6	1308	60	L1	T1	0.2	0.05	T1V1a2f3
14.2	1345	60	L1	T1	0.2	0.1	T1V1a2f2
13.8	1384	60	L1	T1	0.2	0.2	T1V1a2f1
13.4	1425	60	L1	T1	0.1	0.05	T1V1a1f3
13.2	1447	60	L1	T1	0.1	0.1	T1V1a1f2
13	1469	60	L1	T1	0.1	0.2	T1V1a1f1
20	2387	150	L2	T1	0.3	0.05	T1V4a3f3
19.4	2461	150	L2	T1	0.3	0.1	T1V4a3f2
18.8	2540	150	L2	T1	0.3	0.2	T1V4a3f1
18.2	2623	150	L2	T1	0.2	0.05	T1V4a2f3
17.8	2682	150	L2	T1	0.2	0.1	T1V4a2f2

Table A.1: Operation codes adopted for each combination of parameters in the turning tests.

d (mm)	**n (rpm)**	v_c **(m/min)**	**Section**	**Tool**	a_p **(mm)**	**f (mm/rev)**	**Operation Code**
17.4	2744	150	L2	T1	0.2	0.2	T1V4a2f1
17	2809	150	L2	T1	0.1	0.05	T1V4a1f3
16.8	2842	150	L2	T1	0.1	0.1	T1V4a1f2
16.6	2876	150	L2	T1	0.1	0.2	T1V4a1f1
16.4	2329	120	L2	T1	0.3	0.05	T1V3a3f3
15.8	2418	120	L2	T1	0.3	0.1	T1V3a3f2
15.2	2513	120	L2	T1	0.3	0.2	T1V3a3f1
14.6	2616	120	L2	T1	0.2	0.05	T1V3a2f3
14.2	2690	120	L2	T1	0.2	0.1	T1V3a2f2
13.8	2768	120	L2	T1	0.2	0.2	T1V3a2f1
13.4	2851	120	L2	T1	0.1	0.05	T1V3a1f3
13.2	2894	120	L2	T1	0.1	0.1	T1V3a1f2
13	2938	120	L2	T1	0.1	0.2	T1V3a1f1
20	1432	90	L3	T2	0.3	0.05	T2V2a3f3
19.4	1477	90	L3	T2	0.3	0.1	T2V2a3f2
18.8	1524	90	L3	T2	0.3	0.2	T2V2a3f1
18.2	1574	90	L3	T2	0.2	0.05	T2V2a2f3
17.8	1609	90	L3	T2	0.2	0.1	T2V2a2f2
17.4	1646	90	L3	T2	0.2	0.2	T2V2a2f1
17	1685	90	L3	T2	0.1	0.05	T2V2a1f3
16.8	1705	90	L3	T2	0.1	0.1	T2V2a1f2
16.6	1726	90	L3	T2	0.1	0.2	T2V2a1f1
16.4	1165	60	L3	T2	0.3	0.05	T2V1a3f3
15.8	1209	60	L3	T2	0.3	0.1	T2V1a3f2
15.2	1256	60	L3	T2	0.3	0.2	T2V1a3f1
14.6	1308	60	L3	T2	0.2	0.05	T2V1a2f3
14.2	1345	60	L3	T2	0.2	0.1	T2V1a2f2
13.8	1384	60	L3	T2	0.2	0.2	T2V1a2f1
13.4	1425	60	L3	T2	0.1	0.05	T2V1a1f3
13.2	1447	60	L3	T2	0.1	0.1	T2V1a1f2
13	1469	60	L3	T2	0.1	0.2	T2V1a1f1
20	2387	150	L4	T2	0.3	0.05	T2V4a3f3
19.4	2461	150	L4	T2	0.3	0.1	T2V4a3f2
18.8	2540	150	L4	T2	0.3	0.2	T2V4a3f1
18.2	2623	150	L4	T2	0.2	0.05	T2V4a2f3
17.8	2682	150	L4	T2	0.2	0.1	T2V4a2f2
17.4	2744	150	L4	T2	0.2	0.2	T2V4a2f1

Table A.1: Operation codes adopted for each combination of parameters in the turning tests.

d (mm)	**n (rpm)**	v_c **(m/min)**	**Section**	**Tool**	a_p **(mm)**	**f (mm/rev)**	**Operation Code**
17	2809	150	L4	T2	0.1	0.05	T2V4a1f3
16.8	2842	150	L4	T2	0.1	0.1	T2V4a1f2
16.6	2876	150	L4	T2	0.1	0.2	T2V4a1f1
16.4	2329	120	L4	T2	0.3	0.05	T2V3a3f3
15.8	2418	120	L4	T2	0.3	0.1	T2V3a3f2
15.2	2513	120	L4	T2	0.3	0.2	T2V3a3f1
14.6	2616	120	L4	T2	0.2	0.05	T2V3a2f3
14.2	2690	120	L4	T2	0.2	0.1	T2V3a2f2
13.8	2768	120	L4	T2	0.2	0.2	T2V3a2f1
13.4	2851	120	L4	T2	0.1	0.05	T2V3a1f3
13.2	2894	120	L4	T2	0.1	0.1	T2V3a1f2
13	2938	120	L4	T2	0.1	0.2	T2V3a1f1

* d = diameter of the workpiece

Appendix B

Average load values for the turning experiments

Table B.1: Average load values obtained in the turning experiments.

Code	Conventional				AM			
	F_p (N)	F_c (N)	F_f (N)	F_R (N)	F_p (N)	F_c (N)	F_f (N)	F_R (N)
T1V2a3f3	24.04	49.44	30.03	62.65	24.17	52.61	32.12	66.21
T1V2a3f2	28.30	79.12	36.75	91.72	28.32	81.52	37.35	94.04
T1V2a3f1	36.85	139.30	46.00	151.26	32.29	137.04	41.01	146.64
T1V2a2f3	14.96	39.61	19.12	46.46	15.57	38.88	20.10	46.45
T1V2a2f2	17.74	58.37	21.86	64.81	17.95	59.66	23.13	66.46
T1V2a2f1	19.90	98.55	25.92	103.83	18.54	95.59	23.68	100.21
T1V2a1f3	6.53	26.15	8.51	28.26	6.49	23.20	8.62	25.59
T1V2a1f2	7.58	35.48	8.56	37.27	6.69	34.09	9.39	35.99
T1V2a1f1	5.24	53.75	7.32	54.50	6.79	53.72	8.36	54.79
T1V1a3f3	26.70	59.03	34.23	73.27	26.39	56.20	33.47	70.53
T1V1a3f2	31.14	87.61	41.92	102.00	30.33	88.54	41.02	102.19
T1V1a3f1	45.67	157.99	60.50	175.24	34.35	143.55	44.47	154.15
T1V1a2f3	12.53	41.97	17.76	47.26	17.52	43.38	23.17	52.20
T1V1a2f2	17.29	63.54	23.79	70.02	20.34	62.93	25.63	70.93
T1V1a2f1	24.30	108.19	30.80	115.08	19.97	103.20	27.82	108.73
T1V1a1f3	6.14	54.95	15.06	57.30	7.13	26.81	9.52	29.32
T1V1a1f2	7.43	39.24	8.40	40.81	8.34	38.37	10.48	40.64
T1V1a1f1	7.86	62.17	9.67	63.40	7.70	58.84	9.71	60.13
T1V4a3f3	22.78	50.95	29.48	63.12	23.60	51.91	31.89	65.33
T1V4a3f2	25.95	77.86	33.62	88.69	29.29	80.63	35.77	92.95
T1V4a3f1	30.58	135.82	40.49	144.99	28.86	134.85	38.14	143.08
T1V4a2f3	16.30	42.53	20.42	49.92	15.97	39.08	20.39	46.89

Table B.1: Average load values obtained in the turning experiments.

Code	Conventional				AM			
	F_p (N)	F_c (N)	F_f (N)	F_R (N)	F_p (N)	F_c (N)	F_f (N)	F_R (N)
T1V4a2f2	15.97	61.37	22.92	67.42	19.04	61.19	23.76	68.35
T1V4a2f1	15.24	94.57	22.24	98.34	18.16	95.61	22.41	99.86
T1V4a1f3	6.72	26.64	8.91	28.88	5.54	24.24	8.86	26.40
T1V4a1f2	8.06	36.52	9.56	38.61	7.47	34.10	8.88	36.02
T1V4a1f1	6.34	56.59	8.42	57.56	6.36	53.80	7.83	54.74
T1V3a3f3	23.21	56.19	30.20	67.88	23.18	52.83	31.42	65.69
T1V3a3f2	27.42	82.71	34.29	93.65	28.86	84.15	37.91	96.71
T1V3a3f1	30.04	141.63	41.67	150.66	32.61	140.72	41.71	150.35
T1V3a2f3	14.18	44.38	20.22	50.79	14.90	40.34	20.09	47.47
T1V3a2f2	17.80	64.73	23.70	71.20	20.00	64.88	26.42	72.85
T1V3a2f1	18.00	100.74	24.52	105.24	19.69	99.12	23.70	103.80
T1V3a1f3	8.13	29.64	9.39	32.13	7.60	25.54	8.75	28.04
T1V3a1f2	7.77	39.01	9.83	40.97	7.03	36.60	9.61	38.49
T1V3a1f1	7.95	59.80	9.78	61.11	5.59	57.08	8.85	58.03
T2V2a3f3	33.80	59.34	42.98	80.69	33.82	67.84	42.99	87.14
T2V2a3f2	42.70	95.31	56.38	118.69	44.71	105.05	57.70	127.92
T2V2a3f1	48.61	158.54	64.19	177.82	47.57	167.26	62.69	184.85
T2V2a2f3	21.89	45.46	28.64	58.02	19.49	47.97	26.37	58.10
T2V2a2f2	26.02	66.06	32.92	78.26	25.00	73.36	33.29	84.35
T2V2a2f1	27.50	111.53	37.07	120.71	31.15	119.67	38.20	129.43
T2V2a1f3	10.75	29.79	14.09	34.67	9.83	30.58	12.26	34.38
T2V2a1f2	10.01	38.86	13.64	42.39	11.80	43.36	14.44	47.20
T2V2a1f1	12.09	63.00	14.29	65.72	11.32	69.44	15.51	72.05
T2V1a3f3	40.19	69.65	51.58	95.53	37.59	71.01	50.06	94.67
T2V1a3f2	59.54	115.41	75.46	150.19	47.71	109.71	62.43	134.95
T2V1a3f1	62.46	171.39	79.57	199.01	57.31	177.97	73.10	200.75
T2V1a2f3	19.47	44.77	23.90	54.36	23.70	55.22	31.38	67.79
T2V1a2f2	40.82	101.41	51.78	120.96	28.21	79.31	38.28	92.47
T2V1a2f1	38.23	124.81	48.59	139.28	35.42	130.82	45.90	143.09
T2V1a1f3	14.92	35.67	19.07	43.11	10.04	34.53	13.52	38.42
T2V1a1f2	16.42	49.38	20.70	56.01	12.72	48.72	16.52	53.00
T2V1a1f1	15.25	73.47	20.01	77.66	14.40	77.61	19.54	81.32
T2V4a3f3	28.87	65.02	37.32	80.33	32.32	62.79	40.67	81.49
T2V4a3f2	33.37	96.48	43.67	111.04	39.87	97.99	50.46	117.20
T2V4a3f1	43.42	151.91	56.14	167.67	46.91	164.45	60.84	181.51
T2V4a2f3	17.50	41.32	22.97	50.41	20.44	48.85	26.79	59.34

Table B.1: Average load values obtained in the turning experiments.

Code	**Conventional**				**AM**			
	F_p **(N)**	F_c **(N)**	F_f **(N)**	F_R **(N)**	F_p **(N)**	F_c **(N)**	F_f **(N)**	F_R **(N)**
T2V4a2f2	22.42	66.33	30.13	76.23	24.71	71.43	31.35	81.83
T2V4a2f1	23.96	108.87	32.90	116.23	26.77	116.76	36.10	125.12
T2V4a1f3	8.30	25.07	9.40	28.04	10.01	31.66	12.55	35.50
T2V4a1f2	7.00	37.30	11.14	39.55	12.16	43.97	13.93	47.69
T2V4a1f1	8.23	62.22	12.68	64.03	10.04	68.55	14.76	70.84
T2V3a3f3	29.53	60.12	38.90	77.45	31.30	66.93	41.08	84.54
T2V3a3f2	39.22	95.40	49.67	114.48	38.25	99.79	48.84	117.50
T2V3a3f1	48.74	168.65	66.13	187.59	46.69	167.75	60.37	184.30
T2V3a2f3	16.36	43.12	22.81	51.45	20.08	50.94	27.16	61.12
T2V3a2f2	23.78	68.29	29.72	78.18	25.30	75.89	32.24	86.24
T2V3a2f1	26.43	116.12	35.90	124.39	26.26	122.26	36.64	130.31
T2V3a1f3	8.38	28.43	10.54	31.46	10.41	34.26	12.49	37.93
T2V3a1f2	8.99	40.47	11.91	43.13	10.70	44.31	12.90	47.37
T2V3a1f1	8.95	64.62	12.79	66.48	10.40	71.51	14.54	73.71

Appendix C

Comparison between different turning tests

Table C.1: Comparison between André Couto's [42] turning experiment main cutting force (F_c) results and this thesis results for the conventional material.

				Conventional			
				Tool			
				T1	**T1**	**T2**	**T2**
v_c **(mm/min)**	a_p **(mm)**	f **(mm/rev)**	**Code**	**André [42]**	**Marcelo**	**André [42]**	**Marcelo**
60	0.1	0.05	V1a1f3	20.91	54.95	31.75	35.67
60	0.1	0.1	V1a1f2	32.90	39.24	43.16	49.38
60	0.3	0.05	V1a3f3	48.60	59.03	61.89	69.65
60	0.3	0.1	V1a3f2	75.16	87.61	94.27	115.41
90	0.1	0.05	V2a1f3	47.05	26.15	27.33	29.79
90	0.1	0.1	V2a1f2	32.45	35.48	41.20	38.86
90	0.1	0.2	V2a1f1	54.46	53.75	63.90	63.00
90	0.3	0.05	V2a3f3	53.43	49.44	56.66	59.34
90	0.3	0.1	V2a3f2	69.27	79.12	107.98	95.31
90	0.3	0.2	V2a3f1	125.41	139.30	157.97	158.54
120	0.1	0.2	V3a1f1	54.73	59.80	60.71	64.62
120	0.3	0.2	V3a3f1	130.60	141.63	151.19	168.65

Table C.2: Comparison between André Couto's [42] turning experiment main cutting force (F_c) results and this thesis results for the AM material.

				AM			
				Tool			
				T1	**T1**	**T2**	**T2**
v_c **(mm/min)**	a_p **(mm)**	f **(mm/rev)**	**Code**	**André [42]**	**Marcelo**	**André [42]**	**Marcelo**
60	0.1	0.05	V1a1f3	21.43	26.81	33.39	34.53
60	0.1	0.1	V1a1f2	35.22	38.37	41.47	48.72
60	0.3	0.05	V1a3f3	49.97	56.20	70.10	71.01
60	0.3	0.1	V1a3f2	78.76	88.54	100.91	109.71
90	0.1	0.05	V2a1f3	21.95	23.20	30.96	30.58
90	0.1	0.1	V2a1f2	28.60	34.09	41.85	43.36
90	0.1	0.2	V2a1f1	52.49	53.72	65.98	69.44
90	0.3	0.05	V2a3f3	50.63	52.61	63.73	67.84
90	0.3	0.1	V2a3f2	77.48	81.52	100.42	105.05
90	0.3	0.2	V2a3f1	139.94	137.04	165.03	167.26
120	0.1	0.2	V3a1f1	52.02	57.08	69.78	71.51
120	0.3	0.2	V3a3f1	133.83	140.72	158.65	167.75

Appendix D

Codes and parameters for the milling experiments

Table D.1: Operation codes adopted for each combination of parameters in the milling tests.

Section	H (mm)	v_c (m/min)	n (rpm)	a_p (mm)	f_z (mm)	v_f (mm/min)	Operation Code
L1	15	80	1107	0.2	0.05	55.36	V1a1f3
L1	14.8	80	1107	0.2	0.1	110.72	V1a1f2
L1	14.6	80	1107	0.2	0.2	221.43	V1a1f1
L1	14.4	80	1107	0.4	0.05	55.36	V1a2f3
L1	14	80	1107	0.4	0.1	110.72	V1a2f2
L1	13.6	80	1107	0.4	0.2	221.43	V1a2f1
L1	13.2	80	1107	0.6	0.05	55.36	V1a3f3
L1	12.6	80	1107	0.6	0.1	110.72	V1a3f2
L1	12	80	1107	0.6	0.2	221.43	V1a3f1
L2	15	160	2214	0.2	0.05	110.72	V2a1f3
L2	14.8	160	2214	0.2	0.1	221.43	V2a1f2
L2	14.6	160	2214	0.2	0.2	442.87	V2a1f1
L2	14.4	160	2214	0.4	0.05	110.72	V2a2f3
L2	14	160	2214	0.4	0.1	221.43	V2a2f2
L2	13.6	160	2214	0.4	0.2	442.87	V2a2f1
L2	13.2	160	2214	0.6	0.05	110.72	V2a3f3
L2	12.6	160	2214	0.6	0.1	221.43	V2a3f2
L2	12	160	2214	0.6	0.2	442.87	V2a3f1
L3	15	240	3321	0.2	0.05	166.07	V3a1f3
L3	14.8	240	3321	0.2	0.1	332.15	V3a1f2
L3	14.6	240	3321	0.2	0.2	664.30	V3a1f1
L3	14.4	240	3321	0.4	0.05	166.07	V3a2f3
L3	14	240	3321	0.4	0.1	332.15	V3a2f2

Table D.1: Operation codes adopted for each combination of parameters in the milling tests.

Section	**H (mm)**	v_c **(m/min)**	**n (rpm)**	a_p **(mm)**	f_z **(mm)**	v_f **(mm/min)**	**Operation Code**
L3	13.6	240	3321	0.4	0.2	664.30	V3a2f1
L3	13.2	240	3321	0.6	0.05	166.07	V3a3f3
L3	12.6	240	3321	0.6	0.1	332.15	V3a3f2
L3	12	240	3321	0.6	0.2	664.30	V3a3f1
L4	15	320	4429	0.2	0.05	221.43	V4a1f3
L4	14.8	320	4429	0.2	0.1	442.87	V4a1f2
L4	14.6	320	4429	0.2	0.2	885.73	V4a1f1
L4	14.4	320	4429	0.4	0.05	221.43	V4a2f3
L4	14	320	4429	0.4	0.1	442.87	V4a2f2
L4	13.6	320	4429	0.4	0.2	885.73	V4a2f1
L4	13.2	320	4429	0.6	0.05	221.43	V4a3f3
L4	12.6	320	4429	0.6	0.1	442.87	V4a3f2
L4	12	320	4429	0.6	0.2	885.73	V4a3f1

* H = height of the workpiece